# 3D Printed Smart Materials of Continuous Wire Polymer Composites for Sensing Applications

## Mennatullah Elsayed

A DISSERTATION SUBMITTED TO THE FACULTY OF GRADUATE STUDIES IN PARTIAL FULFILLMENT OF THE REQUIREMENTS FOR THE DEGREE OF DOCTOR OF PHILOSOPHY

GRADUATE PROGRAM IN MECHANICAL ENGINEERING

YORK UNIVERSITY

TORONTO, ONTARIO

November 2022

# Abstract

Smart material with sensing capability is an exciting new technology that will impact many applications, including structural health monitoring, biomedical implants, wearable sensors, and actuators. Internal damage in polymer composites is usually hard to predict, and they need to be continuously monitored for any sign of internal damage for safety issues and to increase the life cycle. In this study, continuous wire polymer composites (CWPCs) were 3D-printed using the fused filament fabrication (FFF) technique to produce functional smart materials with different sensing capabilities like strain and thermal sensing. Here, the integrated wire within the conductive polymer composite structure acts as a sensing element. For strain sensing characterization, different design parameters such as matrix type, wire type, and loading condition were investigated to study the effect of these parameters on the efficacy of the CWPC sensor. The different matrices used have different mechanical properties representing rigid (polylactic acid) and flexible (thermoplastic polyurethane) structures to widen the range of application of CWPCs as strain sensors. The change of the electrical resistance of the integrated wire within the CWPCs was measured under tensile loading and plotted against the applied strain. The results of this electromechanical testing demonstrate the ability of CWPCs to be used as strain sensor for either rigid or flexible structures. To check the reliability and reversibility of CWPCs structure as strain sensor, the electromechanical behaviour was investigated under fatigue/cyclic loading. The results of this work demonstrate the reverse piezoresistance behaviour of the CWPC sensor. From thermal sensing standpoint, different design parameters like wire type, matrix type, and sensor thickness were studied to investigate the application of CWPCs as temperature and heat flux sensors which can be readily designed and adapted to suit unique and bespoke thermal applications. The change of the electrical resistance of the integrated wires was correlated to the applied temperature to

measure the heat conducted through a surface. A prototype of a real-world application was designed for the heat flux measurements using CWPC sensor. Generally, this study demonstrates the applicability of FFF technique to print sensors with continuous integrated wire with tuneable properties for different sensing applications.

# Acknowledgement

I would like to express my deepest gratitude to my academic supervisors who helped me at every step along the way. It is without their continuous support and guidance; I would not have been able to accomplish this thesis. So hereby, I thank Prof. Garrett Melenka and Prof. Roger Kempers for always pushing me forward.

I would like to extend my sincere appreciation to my committee members; Prof. Sunny Leung and Prof. Gerd Grau for their valuable suggestions and positive criticism.

I am very thankful to the Melenka and TF-lab team members for their support and assistance during my work. Also, I am thankful to my colleagues at the department of Mechanical Engineering, York University.

Last but not least, no words would be enough to describe the support of my family and their belief in me and my capabilities that encourage me to complete this work.

# Table of Contents

# List of Figures

# List of Tables

# List of Symbols

| | |
|---|---|
| $\Delta R$ | Change in resistance |
| $R$ | Sample's initial resistance before testing |
| $\varepsilon$ | Applied strain |
| $\rho$ | Resistivity of the sensing element |
| $L$ | Length of the sensor |
| $A$ | Surface area of the sensor |
| $R_i$ | Sample resistance measured during testing |
| $\sigma_c$ | UTS of composite |
| $\sigma_w$ | UTS of wire |
| $\sigma_p$ | UTS of polymer |
| $E$ | Young's modulus of the copper |
| $E_c$ | Youngs' modulus of composite |
| $E_w$ | Youngs' modulus of wire |
| $E_p$ | Youngs' modulus of polymer |
| $V_w$ | Volume fraction of the wire within the sample |
| $V_p$ | Volume fraction of the polymer within the sample |
| $V_v$ | Volume fraction of the voids within the sample |
| $v_w$ | Volume of the wire within the sample |
| $v_c$ | Volume of composite sample |
| $v_p$ | Volume of the polymer within the sample |
| $L_{wire}$ | Initial length of the wire |
| $A_{wire}$ | Initial cross-section area of the wire |

| | |
|---|---|
| $D_{wire}$ | Initial diameter of the wire |
| $L_{wire/raster}$ | Initial length of the wire in a single raster |
| l | Total length of the 3D printed sample |
| w | Width of the 3D printed sample |
| t | Thickness of the 3D printed sample |
| $L_i$ | Instantaneous values of the wire length |
| $\Delta_i$ | Instantaneous applied extension |
| $A_i$ | Instantaneous values of the wire area |
| $\nu$ | Poisson's ratio |
| $\nu_c$ | Poisson's ratio of the composite |
| $\nu_w$ | Poisson's ratio of the wire |
| $\nu_p$ | Poisson's ratio of the polymer |
| $\lambda$ | Stretch ratio along the principal axes |
| $\sigma_{Hookean}$ | Applied stress in uniaxial direction (Neo-Hookean model) |
| $\sigma_{Mooney}$ | Applied stress in uniaxial direction (Mooney–Rivlin two parameters model) |
| $\sigma_{Yeoh}$ | Applied stress in uniaxial direction (Yeoh model) |
| $C_1, C_2, C_3$ | Hyperelastic material parameters |
| $\sigma_{exp}$ | Experimental tensile stress |
| $N_f$ | Fatigue life |
| $R_s$ | Strain ratio of fatigue testing |
| $\gamma$ | Material constant in Walker mean stress equation |
| $\varepsilon_a$ | Strain amplitude |
| $\varepsilon_{ea}$ | Elastic strain |

| | |
|---|---|
| $\varepsilon_{pa}$ | Plastic strain |
| $\sigma'_f, \varepsilon'_f, c, b$ | Strain-life constants |
| $\sigma_m$ | Applied mean stress |
| $\alpha$ | Temperature coefficient of resistance |
| $Q_{meas}$ | Heat flux measured across CWPC sample |
| $Q_{applied}$ | Known applied power on CWPC sample |
| $k_{sensor}$ | Thermal conductivity of the CWPC sensor |
| $A_{sesnor}$ | Area of CWPC sensor |
| $A$ | Outer surface area of the insulation |
| $d_{sensor}$ | Thickness of CWPC sensor |
| $T_t$ | Temperature of top layer of CWPC sensor |
| $T_b$ | Temperature of bottom layer of CWPC sensor |
| $\Delta T$ | Temperature difference between top and bottom layer |
| $R_t$ | Electrical resistance of top layer of CWPC sensor |
| $R_b$ | Electrical resistance of bottom layer of CWPC sensor |
| $T_{amb}$ | Ambient temperature |
| $T_i$ | Applied temperature |
| $k_{ins}$ | Thermal conductivity of insulation material |
| $R_{sensor}$ | Thermal resistance of CWPC sensor |
| $L_{sensor}$ | Longitudinal length covered by the CWPC sensor |
| $L_{ins}$ | Length of the uncovered part by the sensor |
| $Q_{ins}$ | Heat flux measured through the insulation material |
| $R_{ins}$ | Thermal resistance of the insulation material |

| | |
|---|---|
| $R_{conv}$ | Thermal resistance of convection |
| $T_{rod}$ | Temperature of the aluminium rod |
| h | Convective heat transfer coefficient |
| q | Heat flux measured by unit area |

## List of Abbreviations

| | |
|---|---|
| PMC | Polymer Matrix Composite |
| CFPC | Continuous Fiber Polymer Composite |
| AM | Additive Manufacturing |
| FFF | Fused Filament Fabrication |
| SLA | Stereolithography |
| LOM | Laminated Object Manufacturing |
| SHM | Structural Health Monitoring |
| 3D | Three Dimensional |
| CWPC | Continuous Wire Polymer Composite |
| CCFPC | Continuous Carbon Fiber Polymer Composite |
| ABS | Acrylonitrile Butadiene Styrene |
| PLA | Polylactic Acid |
| RTD | Resistive Temperature Detector |
| Cu | Copper |
| NiCr | Nichrome |
| UTS | Ultimate Tensile Strength |

GF          Gauge Factor

DMM         Digital Multimeter

ROM         Rule of Mixture

TPU         Thermoplastic Polyurethane

2D DIC      Two-Dimensional Digital Image Correlation

DAQ         Data acquisition

AOI         Area of Interest

ANOVA       Analysis of Variance

Ni          Nickel

# Chapter 1      Introduction

## 1.1.  Research Motivation

Polymer matrix composites (PMCs) have gained high value in engineering applications owing to their wide range of tailorable properties that are unattainable through the use of homogenous materials. The combination of low density and high stiffness of PMCs, the ability to impart new properties, such as thermal or electrical conductivity, that are otherwise uncommon for such class of materials, coupled with their ease of fabrication and low cost, have made PMCs one of the most widely used classes of composites in a wide variety of applications ranging from the sporting to the aerospace industries [1]. Polymer matrices are commonly mixed with various types of reinforcements classified mainly according to their shape and geometry. The main types of reinforcements used in PMC's are continuous and discontinuous fibers [1]. Due to their high specific strength and stiffness properties, and their better thermal and electrical conductivity compared to discontinuous filler materials, continuous fiber polymer composites (CFPC) have been used in several applications such as aerospace, automotive, and sporting equipment industries [1]. For example, carbon fiber composites are widely used in golf clubs to reduce the weight by 10% ~ 40% and increase the damping properties [2]. Additionally, 20% of the Airbus 380 airframe are made of polymer composites, and Boeing 787 has 50% of its components made of polymer composites [3].

Additive manufacturing (AM) is becoming increasingly utilized to overcome the drawbacks of conventional CFPC production [4,5]. The global personal "3D printing market" is valued at USD 2.02 billion in 2022 and is expected to reach a value of USD 3.79 billion by the end of 2027 [6]. AM techniques of CFPC include fused filament fabrication (FFF), stereolithography (SLA),

laminated object manufacturing (LOM), and material jetting process. Out of these different techniques, FFF is the most applied one to produce CFPC as it is a commercially accessible technology with low-cost hardware and a large open-source community for continuous development. CFPC components with enhanced mechanical properties can be readily fabricated by AM techniques, as reported by several researchers [7–11]. To date, most AM CFPC research has focused on improving and quantifying the mechanical properties of the AM components. However, there exists the opportunity to explore and investigate the piezoresistance and thermal sensing capabilities of these types of AM composite.

Smart materials with sensing capabilities can be used in various applications like structural health monitoring (SHM), biomedical implants, wearable sensors, automotive, and actuators. A strain sensor for SHM can be used to measure the in-situ deformation of the product. Among various types of materials used for strain sensors, conductive polymer composites have been developed due to their better flexibility, low cost, and low processing temperature [12]. However, different obstacles hinder the usage of embedded strain sensors within the conductive polymer product as they are usually not durable, difficult to repair, and expensive. Therefore, it is crucial to use self-sensing multi-functional composite structures at which a sensor is an integral part of the structure and can enhance its mechanical properties. This can be achieved through additive manufacturing (AM) of continuous wire polymer composites (CWPC), where the integrated wire within the composite structure act as a sensing element. This fabrication approach provides sensors with design flexibility and repeatability, which widen the range of applications. Furthermore, this AM material can be used as temperature and heat flux sensors. A heat flux sensor is a measuring device that measures the thermal energy transferred through a defined area per unit of time [12,13]. Such

2

customized CWPC heat flux sensor can be applied in various applications such as agricultural to measure soil heat flux and medical as wearable sensor for biometric monitoring.

## 1.2. Thesis Objective

The main objective of this research is to develop the CWPC structure using AM technique for strain and thermal sensing applications. This type of material can leverage the capabilities of FFF technique to produce a multi-functional structure with sensing capabilities with improved mechanical properties. The detailed objective of this study is classified into two main steps, as described below.

*Characterize and verify the reliability of CWPCs as a strain sensor:* Verify the manufactured smart material functions as a piezoresistance sensor for in-situ measurements of the deformation of the samples. Several parameters can be investigated in this project such as wire materials and matrix materials under different loading conditions such as static and dynamic loadings. Different loading conditions were examined to widen the range of applications for the structures subjected to either tensile or cyclic loading. This is important for SHM applications. Two matrices of rigid material (polylactic acid) and flexible material (thermoplastic polyurethane) were applied to leverage the sensing capability of CWPC for either rigid applications such as sporting equipment or flexible applications such as wearable sensor. The reliability of such sensors will further be investigated through conducting cyclic load testing.

*Characterize heat flux sensing using CWPCs:* Study another aspect of sensing application in the field of heat transfer by printing heat flux sensors and measuring the change in resistance within the CWPC using the test rig in [14]. The obtained experimental results will be used to validate the proposed mathematical model to predict the thermal properties of CWPCs.

3

## 1.3. Thesis Outline

To achieve the above-mentioned objectives, the thesis is organized into seven chapters. **Chapter 2** discusses the literature review and the previous studies related to the polymer composites, the additive manufacturing, the structural health monitoring, and temperature and heat flux sensors. In this chapter, the lack of the research of the functionalized 3D-printed CFPC as strain and thermal sensors was addressed to be explored in the following chapters.

Tensile samples of CWPC using two different wires were fabricated using the FFF technique. Electrical resistance of the wires was measured under tensile loading test to characterize the electromechanical properties of CWPC samples. The results showed the capability of the FFF CWPC to be used as strain sensor for structural health monitoring applications. This study is explained in **Chapter 3** and published in peer-reviewed journal of "*Smart Materials and Structures*" under the title "3D printed continuous wire polymer composites strain sensors for structural health monitoring" [15].

To widen the range of applications of FFF CWPC as strain sensor, two types of matrices of rigid and flexible polymers were used to 3D-print the CWPC tensile samples to compare and characterize the electromechanical properties of these materials. The outcome of this study approved the capability of these materials to be used as strain sensors for different applications; either rigid applications such as sports equipment or flexible ones such as wearable sensors. This study is presented in **Chapter 4** and published in peer-reviewed journal of "*Sensors and Actuators A: Physical*" under the title of "A comparative study on the electromechanical properties of 3D-Printed rigid and flexible continuous wire polymer composites for structural health monitoring" [16].

To leverage the capability of CWPC as strain sensor, the electromechanical properties of FFF CWPC structures were examined under dynamic/ cyclic loading. Two types of rigid and flexible samples were subjected to cyclic loading test, and the electrical resistance of the integrated wires was measured simultaneously. The results showed the reverse change of electrical resistance with loading and unloading cycle. This study is presented in **Chapter 5** and published in peer-reviewed journal of "*Fatigue & Fracture of Engineering Materials & Structures*" under the title of "Fatigue behavior and electromechanical properties of additively manufactured continuous wire polymer composites for structural health monitoring" [17].

From the thermal standpoint, the FFF technique was used to 3D-print CWPC samples to characterize their performance as temperature and heat flux sensors. In this study, the electrical resistance of the integrated wire was measured with the change of sample temperature. The results were promising and CWPC samples can be successfully used as temperature and heat flux sensors. This study is presented in **Chapter 6** and submitted in peer-reviewed journal of "*Case Studies in Thermal Engineering*" under the title of "Heat Flux Measurement using 3D-Printed Continuous Wire Polymer Composite Sensors" (under review).

Finally, **Chapter 7** summarizes the outcome of this research study. Also, it presents the potential applications of the developed materials as strain and thermal sensors. The future work of this research is also discussed in this chapter.

## 1.4. References

[1]    Peters ST. Handbook of composites. 2$^{nd}$ ed. Chapman & Hall (2001).

[2]    Tong Y. Application of New Materials in Sports Equipment. IOP Conf Ser Mater Sci Eng 2019;493. https://doi.org/10.1088/1757-899X/493/1/012112.

[3]     Aerospace     |     Composites     UK.     https://compositesuk.co.uk/composite-materials/applications/aerospace (accessed 9 September 2022).

[4]     Goh GD, Dikshit V, Nagalingam AP, Goh GL, Agarwala S, Sing SL, et al. Characterization of mechanical properties and fracture mode of additively manufactured carbon fiber and glass fiber reinforced thermoplastics. Mater Des 2018;137:79–89. https://doi.org/10.1016/j.matdes.2017.10.021.

[5]     Ibrahim Y, Melenka GW, Kempers R. Additive manufacturing of Continuous Wire Polymer Composites. Manuf Lett 2018;16:49–51. https://doi.org/10.1016/j.mfglet.2018.04.001.

[6]     Global Personal 3D Printers Market Report 2022-2027: Surging Demand for 3D Printing in Dental Industry Driving Growth - Business Wire. https://www.businesswire.com/news/home/20220831005450/en/Global-Personal-3D-Printers-Market-Report-2022-2027-Surging-Demand-for-3D-Printing-in-Dental-Industry-Driving-Growth---ResearchAndMarkets.com (accessed 19 November 2022).

[7]     Ibrahim Y, Melenka GW, Kempers R. Fabrication and tensile testing of 3D printed continuous wire polymer composites. Rapid Prototyp J 2018;24:1131–41. https://doi.org/10.1108/RPJ-11-2017-0222.

[8]     Yang C, Tian X, Liu T, Cao Y, Li D. 3D printing for continuous fiber reinforced thermoplastic composites: Mechanism and performance. Rapid Prototyp J 2017;23:209–15. https://doi.org/10.1108/RPJ-08-2015-0098.

[9]     Melenka GW, Cheung BKO, Schofield JS, Dawson MR, Carey JP. Evaluation and prediction of the tensile properties of continuous fiber-reinforced 3D printed structures. Compos Struct 2016;153:866–75. https://doi.org/10.1016/j.compstruct.2016.07.018.

[10] Hofstätter T, Pedersen DB, Tosello G, Hansen HN. State-of-the-art of fiber-reinforced polymers in additive manufacturing technologies. J Reinf Plast Compos 2017;36:1061–73. https://doi.org/10.1177/0731684417695648.

[11] Matsuzaki R, Ueda M, Namiki M, Jeong TK, Asahara H, Horiguchi K, et al. Three-dimensional printing of continuous-fiber composites by in-nozzle impregnation. Sci Rep 2016;6:1–7. https://doi.org/10.1038/srep23058.

[12] Zribi A, Barthès M, Bégot S, Lanzetta F, Rauch JY, Moutarlier V. Design, fabrication and characterization of thin film resistances for heat flux sensing application. Sensors Actuators, A Phys 2016;245:26–39. https://doi.org/10.1016/j.sna.2016.04.040.

[13] Jasperson BA, Schmale J, Qu W, Pfefferkorn FE, Turner KT. Thin film heat flux sensors fabricated on copper substrates for thermal measurements in microfluidic environments. J Micromechanics Microengineering 2014;24. https://doi.org/10.1088/0960-1317/24/12/125018.

[14] Elkholy A, Kempers R. An accurate steady-state approach for characterizing the thermal conductivity of Additively manufactured polymer composites. Case Stud Therm Eng 2022;31. https://doi.org/10.1016/j.csite.2022.101829.

[15] Saleh MA, Kempers R, Melenka GW. 3D printed continuous wire polymer composites strain sensors for structural health monitoring. Smart Mater Struct 2019;28:105041. https://doi.org/10.1088/1361-665x/aafdef.

[16] Saleh MA, Kempers R, Melenka GW. A comparative study on the electromechanical properties of 3D-Printed rigid and flexible continuous wire polymer composites for structural health monitoring. Sensors Actuators, A Phys 2021;328:112764.

https://doi.org/10.1016/j.sna.2021.112764.

[17]   Saleh MA, Kempers R, Melenka GW. Fatigue behavior and electromechanical properties of additively manufactured continuous wire polymer composites for structural health monitoring. FFEMS 2022;45:2630–2645. https://doi.org/10.1111/ffe.13778.

# Chapter 2 Literature Review

Smart materials of conductive polymer composites have gained great interest recently due to their improved mechanical properties, flexibility, low cost, and low processing temperature [1,2]. In this respect, conductive polymer composites are highly recommended in the field of structural health monitoring (SHM) where the material can be used to measure the in-situ deformation of the part. Continuous conductive polymer composites can provide better mechanical, electrical, and thermal properties when compared to discontinuous conductive polymer composites [3]. Most research has focused on laminated continuous carbon fiber polymer composite (CCFPC) as a conductive material to predict the induced strain; however, if the change of the resistance of CCFPC is small, the resistance change can be difficult to measure due to the high stiffness of CCRFP [4]. Alternative approaches employed fiber reinforced laminated composites with embedded wire for electrical measurements [5]. However, the use of embedded sensor within the composite structures may cause difficulties like mechanical property degradation or delamination which will eventually lead to serious structural damage [4]. The optimum solution to address these shortcomings is through using multi-functional composite structures in which the sensor is an integral part of the structure and can simultaneously serve to enhance its mechanical properties. This can be achieved by additive manufacturing (AM) of continuous wire polymer composites (CWPCs) where the integrated wires within the polymer composite structure act as the sensing element. This fabrication technique and this type of materials can also be used for other sensing applications such as thermal sensing applications including temperature and heat flux sensors. Heat flux sensors are used to measure the heat conducted through a surface [6]. AM of CWPC provides design flexibility of the printed heat flux sensor to optimize the performance with improved measurement capability and reduced cost.

## 2.1. Polymer Matrix Composites

A composite material is known as a material including two or more materials deliberately combined to form heterogeneous structures with desired oriented properties and are separated at macroscopic or microscopic scale [7]. The constituents of composite materials are called matrix and reinforcement and/or filler. Although, both reinforcement and matrix retain their electrical, thermal, chemical, and physical identities, yet they together have combination of properties which cannot be achieved by any of the single constituents. Fibres are the load-carrying members, whereas matrix surrounds the fibres to keep them together and acts as the load transfer medium [8]. Published reports showed that there is a rapid increase in the global use of composite materials. The growth in the U.S. composite materials shipment has been increased from USD 8.2 billion to USD 12 billion by 2020 compared to 2014 in different composite industries such as wind energy, transportation/ automotive, construction, aerospace, marine, electronics, consumer goods, and others [9].

Among different types of composite materials used (metallic, polymeric, and ceramic), polymer matrix composite (PMC) is the most commonly used, possessing some advantages compared to other types of composites. For example, PMCs does not require high pressures and temperatures during processing, resulting in significant energy savings during the production stage. Accordingly, there is a rapid development in this type of material and consequently it is nowadays commonly being considered for structural and non-structural applications [10,11].

Polymers used as matrix material can be mainly classified into thermoplastics and thermosets. Thermoplastics polymers have secondary bond between the molecular chains, while the thermosets polymers have primary bond between the molecular chains and they are linked together

by strong cross-links [12]. Thermosets were the first to be introduced as a matrix that can be reinforced by fibers. However, developments recently shifted to thermoplastics, as they are more easily moulded in several manufacturing techniques and have higher moisture resistance and toughness compared to thermosets, in addition they can be easily recycled [8].

Polymer matrices are commonly mixed with various types of reinforcements classified mainly according to their shape and geometry. The main types of reinforcements used in PMCs are continuous fibers and discontinuous fibers (chopped, particles, and flakes reinforcements) as shown in Figure 2-1 [13]. Normally, there is a preferred orientation for continuous fiber reinforced composites, whereas discontinuous fiber reinforced composites generally have random orientation [13].

Compared to discontinuous fibers reinforcements, continuous fiber composites have the highest strength and modulus. Additionally, from the electrical and thermal conductivity standpoint, continuous conductive fibers provide continuous conductive network, and therefore, they have superior electrical and thermal conductivity for smart applications of polymer composites, compared to discontinuous fibers [3].
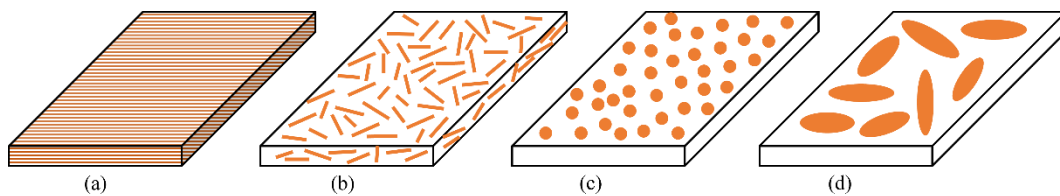
Figure 2-1. Types of composite material based on reinforcement shape; a) Fiber, b) Chopped, c) Particulate, d) Flakes composites [13].

11

## 2.2. Polymer Matrix Composites Applications

PMCs are widely used in transportation such as automotive, marine, and aerospace; sports equipment; construction sector; household appliances; and military. The most popular application for composites is automotive sector where they are being in several parts to achieve weight reduction and energy efficiency. Additionally, American Airline company could decrease the fuel consumption of 600 planes by 11.000 gallons per year if they decreased each aircraft weight only by one pound when using polymer composites [14]. Atkore FRE Composites company used thermoplastic polymer composites to produce robot arms for the international space station [15]. Moreover, fiber reinforced polymer composites (FRPC) are replacing the conventional concrete structures reinforced with steel due to the lower cost of these materials [16]. FRPC are also being used in bridge decks, drainage system, guardrail system, utility poles, pipeline infrastructure, turbine blades for wind energy, and waterfront infrastructure. Speaking of waterfront infrastructure, U.S. Navy spends about $40-50 million to replace wooden structures per year [17]. As for sporting goods and leisure, composites are being strongly introduced to the field where they are extensively used in bicycles, surfboards, snowboards, golf club shafts, racquets, baseball bats motorcyclist helmets, winter sports like hockey, and kayak paddles to name few [17–19].

To widen the range of applications of FRPC, conductive fillers/fibers can be used to reinforce polymer composites to develop smart materials of conductive FRPC. Conductive FRPC can be applied for different smart applications such as bio-inspired structures, self-healing materials, strain sensors, wearable sensors, and thermal sensors [20]. According to Global Market Insight, Inc. report in 2019, market share of conductive polymers is predicted to increase from USD 3.5 billion in 2018 to USD 6 billion in 2025 and North America is accounting for more than 40% of this market share [21].

## 2.3. Processing Techniques of Continuous Fiber Reinforced Thermoplastic Composites

For years, thermoplastic continuous fiber polymer composites (CFPC) manufacturing is commonly performed using several fabrication methods like tape winding/ tape laying, pultrusion, compression molding, thermoforming, and autoclave. The pre-impregnated/prepreg composite material was firstly prepared before being fabricated by any of the above-mentioned fabrication techniques. Yet, processing of CFPC still contends with many problems like high production costs [10]. In addition, these processes experience some limitations like the molds high cost, the inability of producing a special fibers alignment, and the difficulties to manufacture complex and customized construction parts [22]. In this respect, processing technique of AM has been introduced to the industry to overcome these drawbacks. Different techniques of AM have been developed over years like fused filament fabrication (FFF), stereolithography (SLA), polyjet, and laminated object manufacturing (LOM) [22]. As reported in Wholers 2019 [23], the overall market size of additive manufacturing is growing from 15.8 billion US$ in 2020 to 35.6 billion US$ in 2024.

Conventional processing of continuous fiber reinforced composites such as compression molding and pultrusion processes are well-known to produce light weight parts for load bearing structures used in automobile, aerospace, and sports. However, AM techniques such as FFF, LOM, and SLA have been rarely used to fabricate continuous fiber reinforced composites [24].

## 2.4. Additive Manufacturing of Polymer Composites

The process of AM is a fabrication technique of joining layer by layer to produce 3D parts based on a 3D CAD model [20]. Although most of the AM has some limitations in terms of the build

13

time and part size, the main advantages of AM of polymer composites include the ability of formulation of tailorable material, spatial arrangements of phases, functional reinforcement, and 3D customizable complex geometries with minimum labour cost, feedstock material, and waste disposal. Therefore, AM is considered as a pure digital technology and a sustainable business model with minimum usage of fixtures and tooling. These features of AM have led to a paradigm shift in manufacturing industry, especially for the era of Industry 4.0 [22,24].

The maturation of AM technology has been transferred from just a rapid prototyping of the structures to the fabrication of high value parts. It has been applied in different field such as aerospace, building and construction, biomedical, automotive, and food industry [20]. AM of polymer composites gives more chances to extend its applications to functional, electromagnetic shielding, load bearing, and sensing applications [20,25]. To date, intensive studies have been carried out on the functional design of AM polymer composites, including acoustic [26], mechanical [27], electromagnetic materials [28], electrically and thermally conductive structures [29–33], and water treatment [34].

Most of the studies conducted in the field of AM of polymer composites are focused on short fiber reinforcements [22]. Development of AM continuous fiber polymer composite has gained an interest in recent research works and novel AM processes have been studied to tackle the challenges associated with these fabrication techniques and to allow for the production of parts with improved mechanical properties [22].

### 2.4.1. Material Extrusion: Fused Filament Fabrication (FFF)

Material extrusion is one of the most cost effective, user-friendly, and popular AM technique. In this process, the thermoplastic filament is selectively fed into a heated nozzle and is deposited onto a bed in a layer-by-layer manner according to a computer pre-programmed path. During the

14

printing process, the filament is converted from a semi-liquid state to a solid-state after the extrusion as it cools down. FFF is one of material extrusion AM technology [20,24].

The most common thermoplastics used in this process are the amorphous and semi-crystalline ones such as acrylonitrile butadiene styrene (ABS), polylactic acid (PLA), polystyrene (PS), polycarbonate (PC), poly aryl ether ketone (PAEK), nylon, and polyphenylene (PPS). These materials were selected due to their low coefficient of thermal expansion and low melting and glass transition temperatures, which can decrease the internal stresses occurred during cooling. They also have good flowability, mechanical and environmental stability, and no chemical reactions happen during the printing process [20,22].

To introduce functionality to the FFF structure, FFF has been used to produce fiber reinforced composites ranging from nano-scale reinforcement to continuous fiber form. FFF is convenient to print short fiber reinforced polymer composites as no modifications are needed to the extrusion head of the 3D-printer (Figure 2-2a) [35]. However, FFF of short fiber polymer composites suffers from porosity, voids, and weak interfacial bonding, therefore, minimal enhancement of mechanical properties is achieved [35]. It is recommended to incorporate the fiber along the direction of the filament in a continuous form to develop continuous fiber reinforced polymer composites with enhanced mechanical properties. There are several methods to integrate continuous fibers into polymer composites with simple modifications of the print head: Method 1) Continuous fiber incorporation in the print head. Therefore, both fiber and matrix are fed simultaneously and combined as they pass through extruder (Figure 2-2b). Method 2) Continuous fiber incorporation on the component. Therefore, two independent extruders are used with independent nozzles to feed both materials separately (Figure 2-2c). Method 3) Continuous fibers are pre-impregnated into the polymer to from the prepreg filament before being introduced to the nozzle (Figure 2-2d) [22,24].
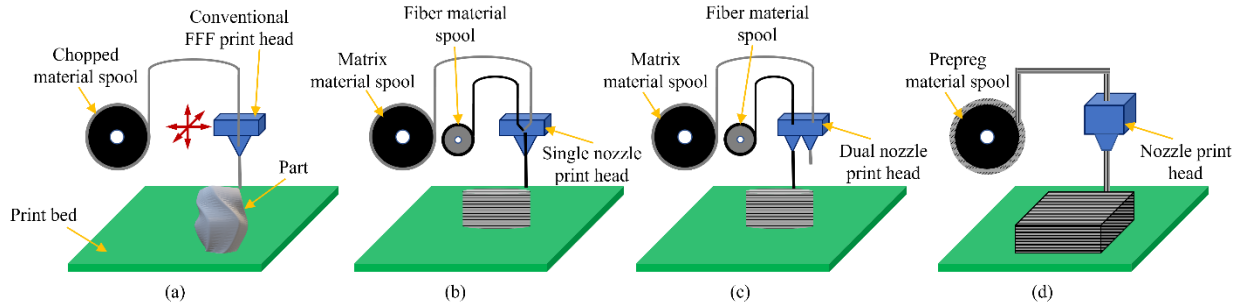
Figure 2-2. Schematic of FFF AM technique [35].

## 2.4.2. Vat Polymerization

In vat polymerization, a photosensitive thermoset liquid resin is selectively cured in a vat using light-activated polymerization process in a layer-by-layer manner based on a computer pre-programmed pattern [20,24]. This category includes SLA, polymerization, continuous liquid interface production, multiphoton polymerization, and digital light processing techniques [20]. To print continuous fiber reinforced polymer composites, SLA is the commonly used process of vat polymerization [22]. AM mirror system is used in SLA process to control the scanning path of the ultraviolet light to cure the photopolymer resin (Figure 2-3) [24]. The most commonly resins used in SLA are epoxy, polyester, and photosensitive polyacrylate. Two methods are followed to introduce the continuous fiber: Method 1) Fiber dispersion on resin surface. Method 2) Premixing the fiber with matrix resin [22]. Some extra mechanism is needed to align the continuous fibers, as the fibers are oriented randomly within the resin. Manual laying mechanism has been developed to fabricate continuous fiber reinforced composites in SLA technique. Placement of continuous fiber has a crucial effect on the mechanical properties, as a poor placement can cause air entrapment which results in uneven surface and poor interlayer bonding. Improvement of mechanical properties has been obtained when incorporating continuous fibers into resin matrix. However, the mechanical properties do not meet the expected requirements because of the weak bonding between the matrix and fiber. This is because the incomplete curing of the material due

16

to the scatted ultraviolet light radiation. Therefore, applying post-processing thermal treatment is necessary to achieve higher mechanical properties. Parts with low porosity and high resolution can be obtained using SLA technique, however, limited materials can be processed [22].
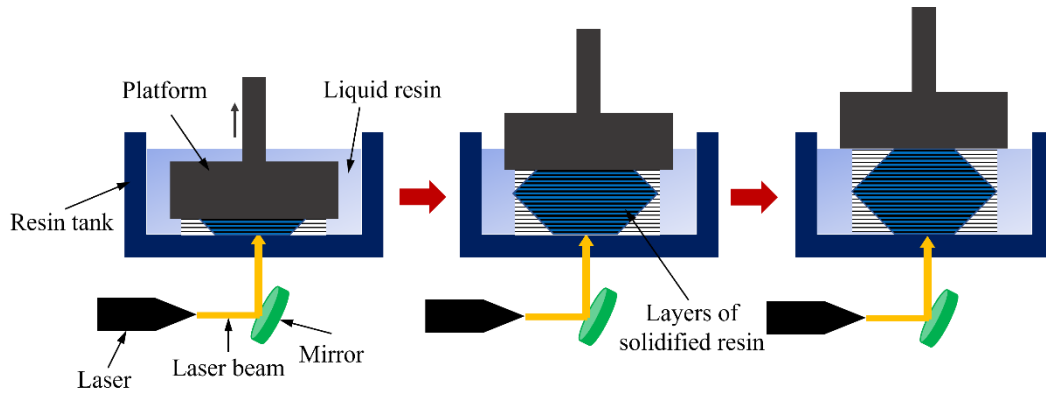


Figure 2-3. Schematic of SLA AM technique [36].

### 2.4.3. Material Jetting Process

In material jetting AM process, the liquid photopolymer resins or thermoplastics in droplet form is selectively deposited through parallel printheads series on a build platform (Figure 2-4). This process is newly introduced to fabricate continuous fiber reinforced composites using dynamic capillary-driven AM technique. Resin with catalyst in liquid state is dropped and deposited onto the continuous fibers before being gradually cured using external thermal energy/ UV light. Compared with continuous fiber reinforced thermoplastic composites fabricated by other AM techniques, this composite fabricated by dynamic capillary-driven AM technique shows a relatively fewer voids and defects and higher packing factor of the fiber. Therefore, superior mechanical behaviour was observed when compared to other thermoplastic composites. The mechanical performances of this composite can vary from soft elastomers to stiff thermoset [20,24].
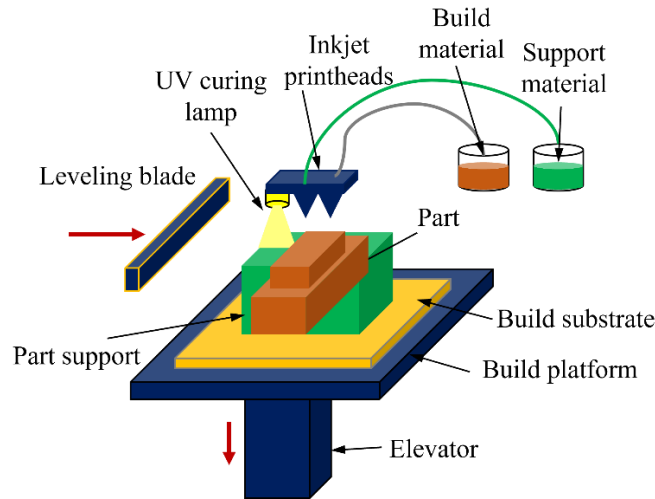
Figure 2-4. Schematic of material jetting technique [37].

### 2.4.4. Laminated object manufacturing

In sheet lamination or LOM process, the feedstock of prepreg composite sheet is shaped based on a computer pre-programmed design using a laser cutting subtractive technique and then the prepreg sheets are stacked and bonded together in a layer-by-layer manner by infra radiation for the prepreg sheets to consolidate efficiently (Figure 2-5). Thermo-curable thermoset and thermoplastic prepreg sheets are commonly employed in LOM. The main advantage of this process is its ability to develop high strength components compared to conventional methods. However, the complexity of the 3D parts is limited by the lamination process as the fabrication of complicated internal features is impossible due to the constrains in removing the unwanted material. Also, to support overhanging features, extra sheets are needed, and this results in material wastage [20,22,24].
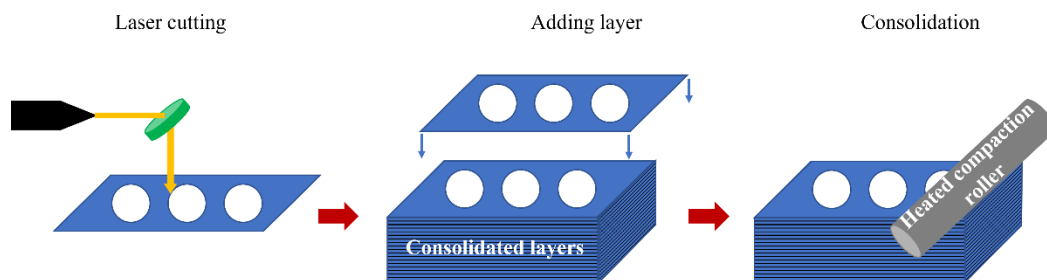


Figure 2-5. Schematic of LOM AM technique [24].

18

### 2.4.5. Automated Fiber Placement (AFP) & AM

Hybrid manufacturing process of AM and AFP technique can be used to resolve the issue associated with the customized complex geometry of continuous fiber reinforced polymer composites [24]. It provides manufacturing flexibility and larger build size compared to the conventional AM methods, strong machine control system, and functional fiber-placement work-cell for effective design of composite structure. The AFP with AM combines a multi-axis robotic arm with the 3D printing head to fabricate the composite structure [38].  A collaborative robotic workcell is used to build a structure where the robot lays the prepreg tows up to enhance the design and workflow of the composite production. The robotic workcell of AFP enlarges the workspace, simplifies the trajectory planning, and improves the efficiency of the production when compared with other approaches of AM to fabricate polymer composites [24]. Although, large structures can be fabricated by mounting the placement head on a gantry system, this technique requires high capital investment [38].

To date, out of different AM techniques, FFF has been commonly used for CFPC fabrication. FFF is more promising because of several reasons. First, it is less demanding technologically as it could be used with slight modifications on the print head for filament extrusion. Second, the feedstock materials used in FFF technique have longer shelf life. Third, it is a commercially accessible technology due to its flexibility with low-cost hardware and its large open-source community for the continuous development [9,11,28].

### 2.5.  AM of Functional Polymer Composites

AM of polymer composites has been emerged to overcome some challenges associated with AM of pure polymers such as limited mechanical properties and to leverage the functionalities of AM parts which are not attainable by pure polymers. Valino et al. [39] compared the mechanical

19

properties of continuous aramid, glass, and carbon fiber reinforced nylon composites with the pure 3D-printed nylon specimen and reported an improvement of 6.3 times for tensile strength and five times for the flexural strength. For most cases, the most interested property for structural system is the load bearing capability which is reflected by the mechanical strength or stiffness. However, other properties such as thermal and electrical conductivity, sensing and actuating abilities, and self-healing are of great importance for several applications [20].

The advantage of accessing individual layers during the AM fabrication enables it to fabricate complex functioning structures and to embed electronics into 3D-printed components. For example, wireless pressure and temperature sensing circuity can be embedded within shoe insole with communication chips for data transmission. To date, the most commonly conductive phases include metallic particles and carbon-based materials (carbon nanotubes (1D) and graphene (2D)) which are added to polymer materials to fabricate functional parts by different AM techniques. For discontinuous fiber/particle reinforced polymer composites, the conductive path is obtained by interconnected 3D-network of conductive additives. The percolation threshold requires minimum volume fraction of filler to achieve the conductive network. The percolation threshold depends on the material type, the size distribution, and the agglomeration and dispersion and when the filler amount exceeds this threshold, the conductivity increases significantly. However, the high amount of filler affects the viscosity of composite, and therefore, it should be considered for AM processes. Generally, the filler content should be compromised to achieve good conductivity and success part fabrication at the same time [20,24,25]. Christ et al. [40] used FFF technique to develop flexible strain sensor made of polyurethane/multiwalled carbon nanotube (TPU/MWCNT). To investigate its performance, electrical and mechanical tests were conducted, and the results showed its superior piezoresistive performance. Leigh et al. [41] developed a conductive polymer composite

compromised of polycaprolactone matrix and carbon black reinforcement to 3D-print electronic sensors using FFF technique. The 3D-printed part was investigated to be used for sensing of capacitance changes and mechanical flexing. A glove was printed to study the flex sensor's ability to detect the changes of electrical resistance upon fingers movement. The sensor electrical resistance was changed according to the movement of the fingers.

The metallic inks are extensively used to develop electrical circuitry within the polymer composites [42–44]; however, they are insufficiently cured due to the thermal resistance limitations of polymers which may degrade at high temperatures. To tackle this issue, sintering process is applied using a light source to heat the metal inherently by photonic absorption. Espalin et al. [44] followed a multiple process approach by integrating FFF with laser welding and machining to fabricate electrically conductive part. Firstly, a polyetherimide was 3D-printed using FFF before being machined to create channels within the substrate. Finally, the copper and silver inks were dispensed and cured by heating.

To address the shortcomings associated with the discontinuous conductive polymer composites, a 3D-printing of conductive continuous polymer composites has been proposed by several researchers [28–32,42,45]. This technique is promising as it combines the advantage of both 3D-printing and a continuous conductive network [31]. This indicates the ability of this 3D-printed material to be used as a strain sensor for different applications such as robotics, prosthetics, and wearable electronics, where multi-directionality, customizability, and complex design are required. It can also be applied for different thermal applications such as heat sinks, heat exchangers and thermal sensors. The following section discusses different studies associated with different sensing applications.

### 2.5.1. Strain Sensing Applications

3D-printed CFPC materials are mainly orthotropic or transversely isotropic due to the nature of the FFF manufacturing process, contrary to conventional isotropic metals, the mechanical properties and failure damage is difficult to predict [5]. To allow for CFPC to be used for functional components, the composite needs to be continuously monitored for any sign of internal damage or failure for safety issues and to increase the life cycle. The system for continuous monitor of the composite structure damage is known as Structural Health Monitoring (SHM) [5,46].

Prior to the usage of SHM techniques, only non-destructive techniques like X-ray, eddy current, or ultrasonic inspection were used to offer periodical inspection of the local damage. A major drawback of these methods is disassembly of the structures may be required for inspection. In this respect, non-destructive inspection methods cannot provide information about the structure in the real-time conditions. In a different way, ongoing monitoring of the integrity of the structure can be provided by an integrated SHM system [47].

SHM systems are used to collect different types of physical quantities like forces, displacements, acoustic emissions, and vibrations, by using the appropriate sensors according to the designed function or purpose [48]. Among various measurable signals, the most common used one is the mechanical strain due to its ease of implementation and its full representation of the health status by delivering the locations of the damage within the structures [4]. Mechanical strain measured using the piezoresistive method at which the mechanical deformation of the structure is correlated to its resistance (ex. strain gauges) is the most commonly applied method among various SHM systems like acoustic emission, fiber bragg grating, optical fiber method, and sonic infrared imaging [1,4,48,49]. Moreover, some of these SHM systems, unlike piezoresistive one, do not allow the sensing of stress/strain in case of damage absence [20,21]. The SHM system was firstly

implemented by Schulte and Baron relying on the piezoresistivity of carbon fiber reinforced polymer laminated composites to sense the internal damage [22]. This was followed by several studies using the method of the piezoresistivity to identify damage within composites [2,5,50–53].

In industrial applications, most of the commercial SHM sensors used are made of metallic films which have low flexibility which can limit the range of applications. Moreover, semiconductor materials were introduced as SHM sensors due to their high piezoresistive sensitivity but they also at the same time have poor mechanical properties [54]. Therefore, smart materials based on polymer composites have been developed to overcome these limitations, in addition, the physico-chemical properties of such polymer composites can be tailored easily for specific application due to their simple integration into composite structures [28,56]. Several researchers [54,55,57–60] studied conductive polymers for their high flexibility and at the same time their notable electrical conductivity, but the conductive polymers are mainly synthesized in a film or a powder form only to be then embedded into the required application and this method limits their usage for several structural applications. On the other hand, conductive filler could be used within the polymer to introduce conductivity. It is recommended to use a conductive filler in a form of continuous fibers instead of discontinuous ones to obtain better electrical properties [61].

When the conductive fibers are mechanically loaded, they become strained and eventually fail. This in turn would affect its electrical conductivity/resistance and thus indicate the "integrity" of the composite [50]. It was found that at small tensile strains, the resistance tended to increase linearly, while at large strains the increase was nonlinear due to fibers damage [2,51]. This change in electrical resistance depends on several parameters such as the orientation of the fiber over which the electrical measurements are recorded, the direction at which the load is applied, and the material of the conductive fibers used. Moreover, the resistance measurements can be used for

further investigation of failure and damage mechanism in polymer composites. For example, the sudden increase in the electrical resistance means that the failure occurred due to the fiber breakage along the fiber direction, while the gradual increase in the electrical resistance till the failure of the structure implies matrix damages [48].

To determine the electrical sensitivity of the piezoresistive sensor, a fundamental parameter, expressed quantitatively as the gauge factor (GF) is calculated. Gauge factor is experimentally calculated, and it is defined as the ratio of fractional change in electrical resistance to the fractional change in length (strain) (Equation 2.1) [5]:

$$GF = (\Delta R/R)/\varepsilon \qquad\qquad (2.1)$$

where $\Delta R$ is the change in the resistance due to the applied strain, $R$ is the initial resistance of the strain sensor, and $\varepsilon$ is the applied strain [5]. Therefore, when the part is subjected to a mechanical strain, its resistance will change consequently according to the electrical resistance equation (Equation 2.2) [49]. Afterwards, the slope of the relation between the fractional change in resistance and the applied mechanical strain is used to get the GF (Equation 2.1) [49,60]. The higher the $\Delta R/R$ value with the strain, the higher the GF indicating the higher sensitivity of the sensor [5].

$$R = \rho\, L/A \qquad\qquad (2.2)$$

where $R$ is the electrical resistance of the sensing element, $\rho$ is the resistivity of the sensing element, and $L$ and $A$ is its length and surface area, respectively.

The GF is mainly depending on both the resistivity and the plasticity of the material of the sensor and the interaction of sensing material-matrix. For most of metals, the change of resistivity ($\rho$) under applied strain is minimal and, hence, the change of electrical resistance of most of metals

comes only from the change of geometry (L: length, A: area) under applied strain. In this respect, the GF is defined as presented in Equation 2.3 [62].

$$GF = 1 + 2v \tag{2.3}$$

where $v$ is the Poisson's ratio.

Researchers have focused on carbon fiber reinforced polymer laminated composite as a conductive material for electrical measurements to predict the induced strain, though, the change of the resistance of carbon fiber is small and it could be difficult to measure due to the high stiffness of carbon fiber reinforced polymer composite [49]. On the other hand, several researchers studied the piezoresistivity of the carbon nano-tube (CNT) in polymer composites due to its enhanced electrical properties at which the conductivity mainly depends on the percolation and tunnelling mechanisms [14,27,36,37,63,64]. It was found that when the loaded polymer/CNT reaches the percolation threshold, its electrical property increases remarkably [65]. Therefore, the volume fraction of CNT within the composite should be in a certain value for the percolation mechanism to occur [49,65]. On the other hand, if the CNT content exceeds a certain limit, the mechanical properties of the composite will start to degrade [27,37]. In this respect, using continuous metal conductive wires within polymer composite could be of great interest due to their good conductivity and their higher flexibility compared to carbon fiber reinforced polymer composites. Therefore, some studies were done on glass fibers reinforced laminated epoxy composite with embedded nickel alloy wire for electrical measurements [16,66]. In this study, the measured resistance of embedded nickel alloy showed two phases of deformation for the composite. In phase I, representing the elastic deformation of the material, the electrical resistance changed linearly under flexural and uniaxial tension loading. While in phase II, representing the plastic deformation

of the material, stepped increase was observed in the piezoresistivity of the nickel alloy wire indicating the accumulation of the microcracks in the composite [16,66]. Using embedded sensors within the composite structures may cause some difficulties like property degradation or delamination which will eventually lead to serious damage to the structures [4]. Moreover, most of the embedded sensors are usually not durable, difficult to repair, and expensive [46,49]. Subsequently, the optimum solution for the above-mentioned drawbacks is through using multi-functional composite structures at which a sensor is an integral part of the structure and can enhance its mechanical properties as well.

2.5.1.1.  Strain Sensing Under Fatigue Loading

Recently, the piezoresistive behaviour of AM polymer composite under cyclic loading has gained a great interest to leverage the sensing capability of this structure under dynamic loading. Fatigue damage of polymer composites is unpredictable as it may occur due to different damage mechanisms and their interactions [67–69]. Dynamic strain monitoring needs a measurand with the ability to change reversibly with reversible straining [70]. The electrical resistance change method is one of the techniques that can be reversibly changed with loading and unloading during the cyclic test. Therefore, it can be used with conductive polymer composites to detect the strain without additional sensors [71]. Augustin et al. [72] monitored the integrity of adhesive bond of the scarf joints by measuring the electrical resistance of the 3D-printed path on the joint bondline under tensile fatigue loading. The increase of the electrical resistance indicated the crack initiation and propagation during the mechanical test.

Nevertheless, from the aforementioned studies, it can be seen that all AM research work has focused on the discontinuous fiber reinforced polymer composites to characterize the sensing capability of this type of 3D-printed structure, while, the 3D-printed CFPC has been only

26

characterized for its mechanical properties [61,73]. The sensing capability of the 3D-printed CWPC has not been studied yet. On the other hand, direct printing capability of CWPC provides design flexibility for the sensors with tuneable properties according to the area of application [4].

### 2.5.2. Thermal Sensing Applications

Lightweight, manufacturability, compactness, and low cost are the recent requirements for heat transfer equipment. Polymers have some advantages over metallic materials, such as their ease of manufacturing, recyclability, and low cost [74–77]. However, they suffer from low thermal conductivity [74]. On the other hand, electrically conductive fillers such as carbon-based materials or metals in a polymer matrix can develop conductive polymer composites with higher thermal properties [32,77].

Some examples of temperature sensors include a thermocouple, thermopile, and resistive temperature detector (RTD). In RTDs, the electrical resistance of the sensing element varies with temperature according to the temperature coefficient of resistance, $\alpha$. RTD sensors typically have short response times, good sensitivity, simple fabrication methods, and small volumes [78]. For instance, RTDs provide accurate absolute temperature measurements instead of differential measurements like thermopiles. In addition, RTDs use only one metallic material during the manufacturing process instead of several materials like the thermocouples [6]. Lee et al. [79] fabricated a temperature sensor of gated reduced graphene oxide (rGo)/polyurethane composite using a lithographic technique. However, it is a complex process, and the sensor is costly.

Other thermal applications of 3D-printed polymer composites include heat exchangers and heat sinks [31,32,80]. For example, Hymas et al. [66] developed metal reinforced polymer composites heat exchangers fabricated by AM technique, and they showed lightweight characteristics with an

increase in the thermal exchange efficiency. Waheed et al. [81] used FFF technique with modified filament compromised of ABS and synthetic microdiamonds to develop heat sinks.

Nikzad et al. [82] studied the thermal conductivity of FFF ABS reinforced with either copper or iron nanoparticles. The thermal conductivity measurements showed a threshold value of 30 vol% and 20 vol% for iron and copper nanoparticles, respectively, to form conductive chains. Ibrahim et al. [31] fabricated 3D-printed continuous fiber polymer composites to investigate the effect of build orientation and fiber volume fraction on the thermal conductivity of carbon fiber composites. They found that adding 34% volume fraction of continuous carbon fiber to the nylon matrix improved the thermal conductivity of the FFF part by around 10 folds. With this technique, the FFF process can be used to fabricate functional parts of conductive continuous polymer composite. 3D-printed panel of copper wire PLA composite was used for an anti- or de-icing system where the copper wire served as a heating element [45].

Nevertheless, the usage of FFF technique to produce CWPC has not been investigated yet to work as a heat flux sensor. Here, the 3D-printing of a functional part can be used to provide the heat flux measurements for the whole structure. This type of structure can be applied in low temperature thermal sensing applications.

## 2.6. Summary

CFPC has superior mechanical, electrical, and thermal properties when compared with discontinuous fiber reinforced polymer composites. As such, in this thesis, conductive polymer composites were developed using CWPC. In comparison with conventional manufacturing techniques of continuous fiber reinforced polymer composites, AM techniques have allowed liberty to fabricate electrically/thermally conductive devices such as sensors, field-effect transistors, actuators, and organic light-emitting diodes inside a 3D-printed structure. Among

different AM techniques, the FFF fabrication technique was selected to fabricate the conductive materials because of its simplicity, customizability, and ability to print complex shapes and utilize various polymeric materials. The strain sensing capability of the 3D-printed CFPC had been investigated in the previous studies based on an embedded sensor within the structure which may cause several challenges as discussed previously. Therefore, in this study, the strain sensing characterization of the FFF CWPC was investigated, where the sensor is an integral part of the structure. From the thermal standpoint, the heat flux characterization has not been investigated previously for the 3D-printed CFPC. Since most of the studies of FFF fabricated composites had focused on the mechanical properties of the structure, different functionalities such as strain and thermal sensing were investigated in this study for CWPCs. The strain sensing ability of 3D-printed CWPC enables them to be used for different applications such as SHM and wearable sensors. Additionally, this material can be used as temperature and heat flux sensors.

The applicability of CWPC to be used as strain sensor using two different wire materials was verified and is discussed in **Chapter 3** of this thesis. In **Chapter 4**, two different matrices of flexible and rigid polymers were used to fabricate CWPC sensor to widen the range of strain sensors applications for both flexible and rigid sensors. **Chapter 5** describes the capability of CWPC materials to be used as strain sensors under dynamic/ cyclic loading. Temperature and heat flux sensors of CWPC were fabricated and characterized as described in **Chapter 6** to be used in different thermal applications.

## 2.7. References

[1] Balaji R, Sasikumar M. Graphene based strain and damage prediction system for polymer composites. Compos Part A Appl Sci Manuf 2017;103:48–59. https://doi.org/10.1016/j.compositesa.2017.09.006.

[2]     Park JB, Okabe T, Takeda N, Curtin WA. Electromechanical modeling of unidirectional CFRP composites under tensile loading condition. Compos - Part A Appl Sci Manuf 2002;33:267–75. https://doi.org/10.1016/S1359-835X(01)00097-5.

[3]     Saleh MA, Kempers R, Melenka GW. A comparative study on the electromechanical properties of 3D-Printed rigid and flexible continuous wire polymer composites for structural health monitoring. Sensors Actuators, A Phys 2021;328:112764. https://doi.org/10.1016/j.sna.2021.112764.

[4]     Lee G, Kim M, Yoon H, Yang J, Ihn J, Ahn S. Direct printing of strain sensors via nanoparticle printer for the applications to composite structural health monitoring. Procedia CIRP 2017;66:238–42. https://doi.org/10.1016/j.procir.2017.03.279.

[5]     Balaji R, Sasikumar M. Development of strain and damage monitoring system for polymer composites with embedded nickel alloys. Meas J Int Meas Confed 2017;111:307–15. https://doi.org/10.1016/j.measurement.2017.07.036.

[6]     Zribi A, Barthès M, Bégot S, Lanzetta F, Rauch JY, Moutarlier V. Design, fabrication and characterization of thin film resistances for heat flux sensing application. Sensors Actuators, A Phys 2016;245:26–39. https://doi.org/10.1016/j.sna.2016.04.040.

[7]     Peters ST. Handbook of composites. 2nd ed. Chapman & Hall 2001.

[8]     Kumar S, Kumar Garkhail S. Composites based on natural fibres and thermoplastic matrices. Queen Mary University of London 2002. http://qmro.qmul.ac.uk/xmlui/handle/123456789/1700

[9]     Vacuum Systems for Composite Manufacturing. https://vacaero.com/information-resources/vac-aero-training/180484-vacuum-systems-for-composite-manufacturing.html

(accessed 8 September 2022).

[10] Pujari S. Comparison of Jute and Banana Fiber Composites: A Review. Int J Curr Eng Technol 2013;2:121–6. https://doi.org/10.14741/ijcet/spl.2.2014.22.

[11] Sathishkumar TP, Naveen J, Satheeshkumar S. Hybrid fiber reinforced polymer composites - A review. J Reinf Plast Compos 2014;33:454–71. https://doi.org/10.1177/0731684413516393.

[12] Thermosetting Plastics Definition - Difference Between Thermoplastic & Thermosetting Plastic. https://byjus.com/chemistry/difference-between-thermoplastic-and-thermosetting-plastic/ (accessed 10 September 2022).

[13] Kaw AK. Mechanics of composite materials. 2nd ed. Taylor & Francis 2006.

[14] Materials Innovation - Aerospace Manufacturing and Design. https://www.aerospacemanufacturinganddesign.com/article/amd0312-metal-aircraft-food-tray-arms/ (accessed 8 September 2022).

[15] Industrial Fiberglass Reinforced Products | FRE Composites. https://frecompositesinc.com/ (accessed 25 July 2022).

[16] Pendhari SS, Kant T, Desai YM. Application of polymer composites in civil construction: A general review. Compos Struct 2008;84:114–24. https://doi.org/10.1016/j.compstruct.2007.06.007.

[17] Creese RC, GangaRao HVS. Polymer composites III 2004: transportation infrastructure, defense and novel applications of composites. DEStech 2004:199.

[18] Brown RP. Polymers in sport and leisure Technology Limited 2001;12.

[19] Koniuszewska AG, Kaczmar JW. Application of Polymer Based Composite Materials in Transportation. Prog. Rubber Plast. Recycl. 2016;32. https://doi.org/10.1177/147776061603200101.

[20] Yaragatti N, Patnaik A. A review on additive manufacturing of polymers composites. Mater. Today Proc. 2020;44:4150–4157. https://doi.org/10.1016/j.matpr.2020.10.490.

[21] Conductive Polymers Market Statistics | Global Forecast - 2027. https://www.gminsights.com/industry-analysis/conductive-polymers-market (accessed 25 July 2022).

[22] Zindani D, Kumar K. An insight into additive manufacturing of fiber reinforced polymer composite. Int J Light Mater Manuf 2019;2:267–78. https://doi.org/10.1016/J.IJLMM.2019.08.004.

[23] Scheuer C, Boot E, Carse N, Clardy A, Gallagher J, Heck S, et al. Wohlers Report 2019: 3D Printing and Additive Manufacturing State of the Industry, Annual Worldwide Progress Report: Chapter title: Middle East: Iran. Phys Educ Sport Child Youth with Spec Needs Res – Best Pract – Situat 2019:343–54.

[24] Yuan S, Li S, Zhu J, Tang Y. Additive manufacturing of polymeric composites from material processing to structural design. Compos Part B Eng 2021;219. https://doi.org/10.1016/j.compositesb.2021.108903.

[25] Bekas DG, Hou Y, Liu Y, Panesar A. 3D printing to enable multifunctionality in polymer-based composites: A review. Compos Part B Eng 2019;179:107540. https://doi.org/10.1016/J.COMPOSITESB.2019.107540.

[26] Konarski SG, Naify CJ, Rohde CA. Buckling-induced reconfigurability in underwater

acoustic scatterers. Appl Phys Lett 2020;116:051903. https://doi.org/10.1063/1.5141097.

[27]    Yuan S, Kai Chua C, Zhou K, Yuan S, Chua CK, Zhou K. 3D-Printed Mechanical Metamaterials with High Energy Absorption. Adv Mater Technol 2019;4:1800419. https://doi.org/10.1002/ADMT.201800419.

[28]    Sankaran S, Deshmukh K, Ahamed MB, Khadheer Pasha SK. Recent advances in electromagnetic interference shielding properties of metal and carbon filler reinforced flexible polymer composites: A review. Compos Part A Appl Sci Manuf 2018;114:49–71. https://doi.org/10.1016/J.COMPOSITESA.2018.08.006.

[29]    Robinson AJ, Colenbrander J, Deaville T, Durfee J, Kempers R. A wicked heat pipe fabricated using metal additive manufacturing. Int J Thermofluids 2021;12:100117. https://doi.org/10.1016/j.ijft.2021.100117.

[30]    Saleh, Menna A, Kempers R, Melenka GW. Fatigue behavior and electromechanical properties of additively manufactured continuous wire polymer composites for structural health monitoring 2022:2630–45. https://doi.org/10.1111/ffe.13778.

[31]    Ibrahim Y, Elkholy A, Schofield JS, Melenka GW, Kempers R. Effective thermal conductivity of 3D-printed continuous fiber polymer composites. Adv Manuf Polym Compos Sci 2020;6:17–28. https://doi.org/10.1080/20550340.2019.1710023.

[32]    Ibrahim Y, Kempers R. Effective thermal conductivity of 3D - printed continuous wire polymer composites. Prog Addit Manuf 2022;V. https://doi.org/10.1007/s40964-021-00256-5.

[33]    Saleh MA, Kempers R, Melenka GW. 3D printed continuous wire polymer composites

strain sensors for structural health monitoring. Smart Mater Struct 2019;28:105041. https://doi.org/10.1088/1361-665x/aafdef.

[34] Li R, Yuan S, Zhang W, Zheng H, Zhu W, Li B, et al. 3D Printing of Mixed Matrix Films Based on Metal-Organic Frameworks and Thermoplastic Polyamide 12 by Selective Laser Sintering for Water Applications. ACS Appl Mater Interfaces 2019;11:40564–74. https://doi.org/10.1021/ACSAMI.9B11840/SUPPL_FILE/AM9B11840_SI_008.MP4.

[35] Naranjo-Lozada J, Ahuett-Garza H, Orta-Castañón P, Verbeeten WMH, Sáiz-González D. Tensile properties and failure behavior of chopped and continuous carbon fiber composites produced by additive manufacturing. Addit Manuf 2019;26:227–41. https://doi.org/10.1016/j.addma.2018.12.020.

[36] Sano Y, Matsuzaki R, Ueda M, Todoroki A, Hirano Y. 3D printing of discontinuous and continuous fibre composites using stereolithography. Addit Manuf 2018;24:521–7. https://doi.org/10.1016/J.ADDMA.2018.10.033.

[37] Velu R, Sathishkumar R, Saiyathibrahim A. Perspective Chapter: Multi-Material in 3D Printing for Engineering Applications. Adv Addit Manuf 2022. https://doi.org/10.5772/INTECHOPEN.102564.

[38] Raspall F, Velu R, Vaheed NM. Fabrication of complex 3D composites by fusing automated fiber placement (AFP) and additive manufacturing (AM) technologies. Adv Manuf: Polym Compos Sci 2019 Jan 2;5(1):6-16. https://doi.org/10.1080/20550340.2018.1557397.

[39] Valino AD, Dizon JRC, Espera AH, Chen Q, Messman J, Advincula RC. Advances in 3D printing of thermoplastic polymer composites and nanocomposites. Prog Polym Sci

2019;98:101162. https://doi.org/10.1016/J.PROGPOLYMSCI.2019.101162.

[40] Christ JF, Aliheidari N, Ameli A, Pötschke P. 3D printed highly elastic strain sensors of multiwalled carbon nanotube/thermoplastic polyurethane nanocomposites. Mater Des 2017;131:394–401. https://doi.org/10.1016/J.MATDES.2017.06.011.

[41] Leigh SJ, Bradley RJ, Purssell CP, Billson DR, Hutchins DA. A Simple, Low-Cost Conductive Composite Material for 3D Printing of Electronic Sensors. PLoS One 2012;7:e49365. https://doi.org/10.1371/JOURNAL.PONE.0049365.

[42] El-Hajj Y, Ghalamboran M, Grau G. Inkjet and Extrusion Printed Silver Biomedical Tattoo Electrodes. FLEPS 2022:1–4. https://doi.org/10.1109/fleps53764.2022.9781535.

[43] Idris MK, Naderi P, Melenka GW, Grau G. Damage location sensing in carbon fiber composites using extrusion printed electronics. Funct Compos Struct 2021;3. https://doi.org/10.1088/2631-6331/ac3731.

[44] Espalin D, Muse DW, Macdonald E, Wicker RB, Muse DW, Macdonald E, et al. 3D Printing multifunctionality: structures with electronics. Int J Adv Manuf Technol 2014;72:963–78. https://doi.org/10.1007/S00170-014-5717-7.

[45] Ibrahim Y, Kempers R, Amirfazli A. Cold Regions Science and Technology 3D printed electro-thermal anti- or de-icing system for composite panels. Cold Reg Sci Technol 2019;166:102844.

[46] Balaji R, Sasikumar M. A nanometallic nickel-coated, glass-fibre-based structural health monitoring system for polymer composites. Smart Mater Struct 2017;26. https://doi.org/10.1088/1361-665X/aa74f4.

[47]   Lu S, Tian C, Wang X, Zhang L, Du K, Ma K, et al. Strain sensing behaviors of GnPs/epoxy sensor and health monitoring for composite materials under monotonic tensile and cyclic deformation. Compos Sci Technol 2018;158:94–100. https://doi.org/10.1016/j.compscitech.2018.02.017.

[48]   Wen J, Xia Z, Choy F. Damage detection of carbon fiber reinforced polymer composites via electrical resistance measurement. Compos Part B Eng 2011;42:77–86. https://doi.org/10.1016/j.compositesb.2010.08.005.

[49]   Johnson TM, Fullwood DT, Hansen G. Strain monitoring of carbon fiber composite via embedded nickel nano-particles. Compos Part B Eng 2012;43:1155–63. https://doi.org/10.1016/j.compositesb.2011.09.014.

[50]   Park JB, Okabe T, Takeda N. New concept for modeling the electromechanical behavior of unidirectional carbon-fiber-reinforced plastic under tensile loading. Smart Mater Struct 2003;12:105–14. https://doi.org/10.1088/0964-1726/12/1/312.

[51]   Ogi K, Takao Y. Characterization of piezoresistance behavior in a CFRP unidirectional laminate. Compos Sci Technol 2005;65:231–9. https://doi.org/10.1016/j.compscitech.2004.07.005.

[52]   Xia Z, Okabe T, Park JB, Curtin WA, Takeda N. Quantitative damage detection in CFRP composites: Coupled mechanical and electrical models. Compos Sci Technol 2003;63:1411–22. https://doi.org/10.1016/S0266-3538(03)00083-6.

[53]   Xia ZH, Curtin WA. Modeling of mechanical damage detection in CFRPs via electrical resistance. Compos Sci Technol 2007;67:1518–29. https://doi.org/10.1016/j.compscitech.2006.07.017.

[54] Cai G, Wang J, Qian K, Chen J, Li S, Lee PS. Extremely Stretchable Strain Sensors Based on Conductive Self-Healing Dynamic Cross-Links Hydrogels for Human-Motion Detection. Adv. Sci. 2017;4:1600190. https://doi.org/10.1002/advs.201600190

[55] Teixeira J, Horta-Romarís L, Abad MJ, Costa P, Lanceros-Méndez S. Piezoresistive response of extruded polyaniline/(styrene-butadiene-styrene) polymer blends for force and deformation sensors. Mater Des 2018;141:1–8. https://doi.org/10.1016/j.matdes.2017.12.011.

[56] Waheed S, Cabot JM, Smejkal P, Farajikhah S, Sayyar S, Innis PC, Beirne S, Barnsley G, Lewis TW, Breadmore MC, Paull B. Three-Dimensional Printing of Abrasive, Hard, and Thermally Conductive Synthetic Microdiamond-Polymer Composite Using Low-Cost Fused Deposition Modeling Printer. ACS Appl Mater Interfaces 2019;11:4353–63. https://doi.org/10.1021/acsami.8b18232.

[57] Yoon H. Current Trends in Sensors Based on Conducting Polymer Nanomaterials. Nanomaterials 2013;3:524–49. https://doi.org/10.3390/nano3030524.

[58] Latessa G, Brunetti F, Reale A, Saggio G, Di Carlo A. Piezoresistive behaviour of flexible PEDOT:PSS based sensors. Sensors Actuators, B Chem 2009;139:304–9. https://doi.org/10.1016/j.snb.2009.03.063.

[59] Takamatsu S, Takahata T, Muraki M, Iwase E, Matsumoto K, Shimoyama I. Transparent conductive-polymer strain sensors for touch input sheets of flexible displays. J Micromechanics Microengineering 2010;20. https://doi.org/10.1088/0960-1317/20/7/075017.

[60] Zein A El, Hupp C, Cochrane C. Development of a Flexible Strain Sensor Based on

PEDOT : PSS for Thin Film Structures. Sensors 2017:1–14. https://doi.org/10.3390/s17061337.

[61] Ibrahim Y, Melenka GW, Kempers R. Fabrication and tensile testing of 3D printed continuous wire polymer composites. Rapid Prototyp J 2018;24:1131–41. https://doi.org/10.1108/RPJ-11-2017-0222.

[62] Angelidis N, Wei CY, Irving PE. The electrical resistance response of continuous carbon fibre composite laminates to mechanical strain. Compos Part A Appl Sci 2004 Oct 1;35(10):1135-47. https://doi.org/10.1016/j.compositesa.2004.03.020.

[63] Industrial Fiberglass Reinforced Products | FRE Composites. https://frecompositesinc.com/ (accessed 8 September 2022).

[64] Esfandiari P, Silva JF, Novo PJ, Nunes JP, Marques AT. Production and processing of pre-impregnated thermoplastic tapes by pultrusion and compression moulding. J. Compos. Mater. 2022;56:1667–76. https://doi.org/10.1177/00219983221083841.

[65] Hu N, Karube Y, Yan C, Masuda Z, Fukunaga H. Tunnelling effect in a polymer / carbon nanotube nanocomposite strain sensor. Acta Mater. 2008;56:2929–36. https://doi.org/10.1016/j.actamat.2008.02.030.

[66] Hymas DM, Arle MA, Singer F, Shooshtari AH, Ohadi MM. Enhanced air-side heat transfer in an additively manufactured polymer composite heat exchanger. Proc 16th Intersoc Conf Therm Thermomechanical Phenom Electron Syst ITherm 2017:634–8. https://doi.org/10.1109/ITHERM.2017.7992546.

[67] Safai L, Cuellar JS, Smit G, Zadpoor AA. A review of the fatigue behavior of 3D printed polymers. Addit Manuf 2019;28:87–97. https://doi.org/10.1016/j.addma.2019.03.023.

[68] Saleh MA, Al Haron MH, Saleh AA, Farag M. Fatigue behavior and life prediction of biodegradable composites of starch reinforced with date palm fibers. Int J Fatigue 2017;103:216–22. https://doi.org/10.1016/j.ijfatigue.2017.06.005.

[69] Giancane S, Panella FW, Nobile R, Dattoma V. Fatigue damage evolution of fiber reinforced composites with digital image correlation analysis. Procedia Eng 2010;2:1307–15. https://doi.org/10.1016/j.proeng.2010.03.142.

[70] Wang X, Chung DDL. Self-monitoring of fatigue damage and dynamic strain in carbon fiber polymer-matrix composite. Compos Part B Eng 1998;29:63–73. https://doi.org/10.1016/S1359-8368(97)00014-0.

[71] Iizuka K, Todoroki A, Takahashi T, Ueda M. Reverse piezo-resistivity of 3D printed continuous carbon fiber/PA6 composites in a low stress range. Adv Compos Mater 2021;30:380–95. https://doi.org/10.1080/09243046.2020.1848314.

[72] Augustin T, Karsten J, Kötter B, Fiedler B. Health monitoring of scarfed CFRP joints under cyclic loading via electrical resistance measurements using carbon nanotube modified adhesive films. Compos Part A Appl Sci Manuf 2018;105:150–5. https://doi.org/10.1016/J.COMPOSITESA.2017.11.015.

[73] Melenka GW, Cheung BKO, Schofield JS, Dawson MR, Carey JP. Evaluation and prediction of the tensile properties of continuous fiber-reinforced 3D printed structures. Compos Struct 2016;153:866–75. https://doi.org/10.1016/j.compstruct.2016.07.018.

[74] Vadivelu MA, Kumar CR, Joshi GM. Polymer composites for thermal management: a review. Compos Interfaces 2016;23:847–72. https://doi.org/10.1080/09276440.2016.1176853.

[75]    Kalsoom U, Peristyy A, Nesterenko PN, Paull B. A 3D printable diamond polymer composite: A novel material for fabrication of low cost thermally conducting devices. RSC Adv 2016;6:38140–7. https://doi.org/10.1039/c6ra05261d.

[76]    Chen J, Zhu Y, Huang J, Zhang J, Pan D, Zhou J, et al. Advances in Responsively Conductive Polymer Composites and Sensing Applications. Polym Rev 2021;61:157–93. https://doi.org/10.1080/15583724.2020.1734818.

[77]    Chen J, Zhu Y, Guo Z, Nasibulin AG. Recent progress on thermo-electrical properties of conductive polymer composites and their application in temperature sensors. Eng Sci 2020;12:13–22. https://doi.org/10.30919/es8d1129.

[78]    Dankoco MD, Tesfay GY, Benevent E, Bendahan M. Temperature sensor realized by inkjet printing process on flexible substrate. Mater Sci Eng B Solid-State Mater Adv Technol 2016;205:1–5. https://doi.org/10.1016/j.mseb.2015.11.003.

[79]    Lee H, Choi TK, Lee YB, Cho HR, Ghaffari R, Wang L, Choi HJ, Chung TD, Lu N, Hyeon T, Choi SH, Kim D. A graphene-based electrochemical device with thermoresponsive microneedles for diabetes monitoring and therapy. Nat. Nanotechnol 2016;11:566–572. https://doi.org/10.1038/nnano.2016.38.

[80]    Elsayed Y, Elkholy A, Melenka G, Kempers R. Continuous Fiber Polymer Composites for Thermal Applications 2018:1–6. https://doi.org/10.25071/10315/35371.

[81]    Waheed S, Cabot JM, Smejkal P, Farajikhah S, Sayyar S, Innis PC, et al. Three-Dimensional Printing of Abrasive, Hard, and Thermally Conductive Synthetic Microdiamond-Polymer Composite Using Low-Cost Fused Deposition Modeling Printer. ACS Appl Mater Interfaces 2019;11:4353–63. https://doi.org/10.1021/acsami.8b18232.

[82]    Nikzad M, Masood SH, Sbarski I. Thermo-mechanical properties of a highly filled polymeric composites for Fused Deposition Modeling. Mater Des 2011;32:3448–56. https://doi.org/10.1016/J.MATDES.2011.01.056.

# Chapter 3      3D Printed Continuous Wire Polymer Composites Strain Sensors for Structural Health Monitoring

A version of this chapter has been published as:

Menna A. Saleh, Roger Kempers, Garrett W. Melenka. 3D Printed Continuous Wire Polymer Composites Strain Sensors for Structural Health Monitoring. Smart Materials and Structures

(2019)

This chapter presents the electromechanical properties of three dimensional (3D) printed unidirectional continuous wire polymer composite (CWPC) to study the correlation of the elastic mechanical deformation and the electrical resistance under uniaxial loading conditions. Two kinds of wires were used for this study: copper (Cu) and nichrome (NiCr). 3D printing was utilized due to its flexibility in design and structure for different applications. From mechanical testing, the NiCr CWPCs demonstrated an increase of 13.5% and 54% in ultimate tensile strength (UTS) and Young's modulus, respectively, compared to pure 3D printed polylactic acid (PLA) while the Cu CWPC did not exhibit significant improvement in the mechanical properties. A direct linear relationship was observed between the applied tensile strain and the measured electrical resistance for both Cu and NiCr CWPCs indicating the ability of these 3D printed structures to be used as a sensor to measure stress/strain in the real time. In addition, the sensitivity of both composites in terms of gauge factor (GF), representing the relative change in the electrical resistance with the tensile strain of the material, were found to be 1.17 ±0.06 and 1.13 ±0.07 for Cu and NiCr CWPCs, respectively. This sensitivity was compared with a simple analytical model and showed a good agreement with the experimental results. Finally, the reliability of these CWPCs was evaluated by conducting a cyclic loading test within their elastic ranges.  The results of this work will enable

the manufacture of integrated sensors within 3D printed components with improved mechanical properties and increased functionality.

## 3.1. Introduction

Continuous fiber polymer composites (CFPCs) provide improved specific stiffness, specific strength, thermal and electrical conductivity over short fiber reinforced polymer composites [1,2]. CFPCs have been used in numerous applications such as aerospace, automotive, and sporting equipment industries [1,2] however CFPCs still contend with many problems such as long processing cycle times which leads to high production costs [3]. Common CFPC manufacturing methods include manual hand-layup, vacuum forming, pultrusion, filament winding, compression molding, and bladder assisted molding [4]. Drawbacks of these manufacturing methods include high molds cost, the inability of producing a specific fiber orientation, and the difficulties to manufacture complex construction parts [4].

Additive manufacturing (AM) is becoming increasingly utilized to overcome drawbacks of conventional CFPC production [1,2]. Presently, only fused filament fabrication (FFF) and stereolithography technologies have been used for CFPC fabrication [1]. FFF manufacturing is ideally suited for CFPC manufacturing since continuous fibers can be extruded along with a thermoplastic material through a heated nozzle. Continuous fiber FFF is becoming a commercially accessible technology due to its flexibility with low-cost hardware and its large open-source community for the continuous development [2,5].

Producing continuous fiber reinforced composites with enhanced mechanical properties can be readily achieved by AM techniques as reported by several researchers [2,4,6–8]. Melenka et al. [6] demonstrated that the ultimate strength and stiffness were increased with increasing the volume

43

fraction of continuous reinforcement fiber for Kevlar reinforcement nylon composite. Matsuzaki et al. [8] showed that the strength and Young's modulus of carbon fiber reinforced PLA composite was improved by 435% and 599%, respectively, compared to PLA. Ibrahim et al. [2,9] developed a method of 3D printing continuous wire polymer composites (CWPCs) and reported that Young's modulus of the polylactic acid (PLA) was enhanced by 30 % when reinforcing the polymer with a continuous metal wire.

Structural Health Monitoring (SHM) is a system to continuously monitor composite structure damage [10,11]. Common SHM sensing technologies include piezoresistive, acoustic emission, fiber bragg grating (FBG), and sonic infrared imaging [12–16]. The most common method for achieving SHM in conventional CFPC is a piezoresistive method [10]. Mechanical deformation of the structure is correlated to its resistance and thus indicate the "integrity" of the structure. Many of these SHM systems do not allow the sensing of stress/strain in case of damage absence [13]. Among various types of materials used for piezoelectric SHM systems, smart materials based on polymer composites have been developed due to their better mechanical properties in terms of flexibility and their low cost as well due to their low processing temperature which in turn widen the range of applications [16,17]. The piezoresistive SHM method is well suited to the measurement of 3D printed CFPC structures.

To determine the electrical sensitivity of the piezoresistive sensor, the gauge factor (GF) is a fundamental parameter. GF is an experimentally calculated correlation factor and it is defined as the ratio of fractional change in electrical resistance, to the fractional change in strain according to Equation 3.1 [11,18]:

$$GF = \frac{\Delta R/R}{\varepsilon} \qquad (3.1)$$

where $\Delta R$ is the change in the resistance due to the applied strain, $R$ is the initial resistance of the strain sensor, and $\varepsilon$ is the applied strain [11]. When the sensor is subjected to a mechanical strain, its resistance will change due to the elongation and reduction of cross-sectional area of the conductive element and is governed by the electrical resistance equation (Equation 3.2) [19].

$$R = \rho \frac{L}{A} \tag{3.2}$$

The slope of the relation between the fractional change in resistance and the applied mechanical strain is used to calculate the GF (Equation 3.1) [19,20]. In this respect, the GF is mainly dependent on the resistivity and the plasticity of the material of the sensor and the interaction of sensing material-matrix. The higher the $\Delta R/R$ value with the strain, the higher the GF indicating the higher sensitivity of the sensor [11].

Lee et al. measured the gauge factor of the silver nanoparticle printed sensor on the top of different thermoplastic substrates [12]. In this study, the substrate acts as an electric insulation between the conductive nanoparticle and the prepreg CFPC [12]. Here the sensor was separately printed on the surface of the structure which may lead to several difficulties like property degradation or delamination, not durable, and expensive [10,12,15].

Currently, SHM sensing of 3D-printed CWPCs has not been examined. Integrated manufacturing of SHM sensors has not been undertaken. To date, most AM CFPC or CWPC research has focused on improving and quantifying the mechanical properties (strength and stiffness) of the 3D printed components. However, particularly for the electrically conductive metal wires present in CWPCs, the exists the opportunity to explore and investigate the piezoresistive sensing capabilities of these types of 3D printed composite. Direct printing capability provides design flexibility for the sensors with tunable properties while also providing improved mechanical properties [12].

In the present study, the electromechanical behavior of a CWPC components is characterized to understand how they would function in SHM applications. Here, the integrated metal wire acts as a SHM strain sensor as the reinforced polymer 3D printed structure is subjected to mechanical loading. This methodology will produce a multifunctional 3D printed CFPC structure. Two reinforcing/sensing wire materials (copper, Cu and nichrome, NiCr) were examined, and their performance was evaluated based on the value of their gauge factor. Analytical models for both mechanical and electrical properties were proposed to compare the theoretical obtained values with the experimental data. Finally, the samples were subjected to cyclic tensile loading to understand the electromechanical reliability of these AM CWPCs as sensors.

## 3.2. Experimental Methods

To characterize the electromechanical and piezoresistive properties of the AM CWPC, samples were fabricated and experimentally tested using a tensile testing apparatus in conjunction with electrical resistance instrumentation. The methods and procedures used are described here.

### 3.2.1. Sample Fabrication

The CWPC test samples were fabricated using an open source modified 3D printer (Prusa i3 mk2, Prusa Research, Prague, Czech Republic). The open-source printer was modified to allow for the introduction of continuous wires within a polymer structure. The continuous wire reinforced polymer structures were manufactured using the method reported by Ibrahim et al. [2,9]. The samples were prepared according to ASTM D3039 -17, which describes the standard test method for tensile properties of polymer matrix composite materials. The samples had nominal dimensions of 200 mm long by 25 mm wide and 2 mm thick (Figure 3-1) and were printed using the printing

parameters shown in Table 3-1. A customized MATLAB script was created to generate the G-code which is used to 3D print the unidirectional continuous wire reinforced PLA composite.
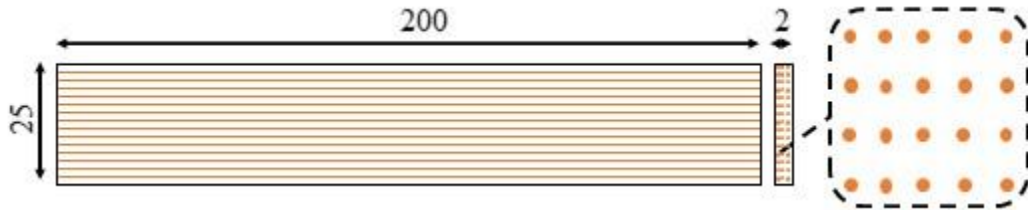


Figure 3-1. Schematic representation of 3D printed CWPC sample showing approximate wire distribution.

Table 3-1. 3D printing parameter for continuous wire reinforced PLA composite.

| Printing parameters | | |
|---|---|---|
| Extruder temperature | 170 | °C |
| Bed Temperature | 55 | °C |
| Extruder multiplier | 1.3 | |
| Nozzle diameter | 0.6 | mm |
| Wire diameter | 0.075 | mm |
| Raster width | 0.65 | mm |
| Layer height | 0.4 | mm |
| Printing angle | 0 | ° |
| Number of rasters | 38 | |
| Number of layers | 5 | |
| Fill density | 100 | % |

The ends of the conductive wires extended out from the printed sample as shown in Figure 3-2a to allow for electrical connections. These two wire ends were soldered to a 0.065 mm thick copper tape as shown in Figure 3-2b to which served as terminals to connect the resistance instrumentation detailed below.
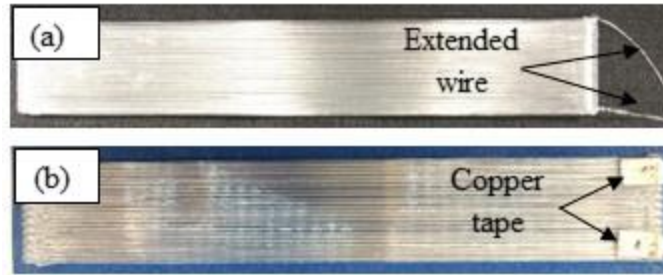
Figure 3-2. Example 3D printed NiCr wire reinforced PLA composite with; a) two extended wire

ends, b) two electrical terminals.

For the Cu CWPC sample, the two wires were extended from one corner at the bottom layer and one corner at the top layer of the printed sample for the electrical resistance to be measured through a single circuit running through all five layers. However, the NiCr CWPC samples used un-coated wires which were susceptible to potential short circuiting between the wires in adjacent layers, particularly in the gripping region at the ends of the sample. To avoid this, the lead wires were extended from only the middle layer circuit and the electrical resistance was measured only in this layer.

PLA rectangular end tabs of 60 mm × 25 mm × 2 mm were printed with a taper angle at the end of 6.7° and bonded to the ends of the sample as shown in Figure 3-3. End tabs were used to prevent sample slipping between the grips and to ensure that fracture to occur within the gauge length of the sample instead of gripping area.
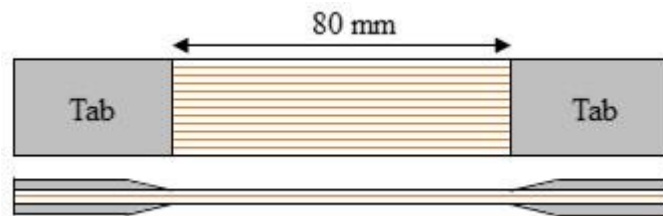


Figure 3-3. NiCr wire reinforced PLA with end tabs.

### 3.2.2. Materials

Transparent PLA filament (1.75 mm Transparent PLA, ColorFabb, The Netherlands) was used as the polymer feedstock. Two metallic wires were used in this work. Copper wire coated with polyimide (75 µm Cu wire, Remington Industries, USA), and a nickel-chromium wire (75 µm NiCr wire, Consoloidated Electronics Wire & Cable, Illinois, USA).

### 3.2.3. Electromechanical Testing

The electromechanically characteristics of each CWPC sample were obtained by measuring the electrical resistance of the embedded wire during tensile testing as shown in Figure 3-4. Samples were loaded with a crosshead speed of 0.5 mm/min using a universal testing machine (MTS Criterion Model 43, Eden Prairie, MN USA) equipped with 10 kN load cell. The sample extension was recorded using laser extensometer (LX500 laser extensometer, MTS, Eden Prairie, MN).

The electrical resistance of the printed sample was recorded in-situ by a digital multimeter (DMM) (Agilent 34401A, Agilent Technologies, Incorporated, Colorado, USA) using the four-probe method as shown in Figure 3-4 to eliminate the resistance of the lead wires. In this configuration, two copper wires were soldered to each of the sample electrodes. The uncertainty of the resistance measurement depends on the range of the measured electrical resistance for each type of material. The electrical resistance for the used Cu and NiCr wires were in the range of 1 kΩ and 10 kΩ, respectively. Therefore, the uncertainty in the electrical resistance measurements was $\pm25$ µΩ and $\pm189.5$ µΩ for Cu wire and NiCr wire reinforced PLA composite, respectively.

Data was collected continuously to a computer using a customized MATLAB script. It is important to note that the strain and the electrical resistance data were recorded with a same data collection

frequency of 2 Hz to guarantee data synchronization. Five samples were tested for each CWPC configuration.
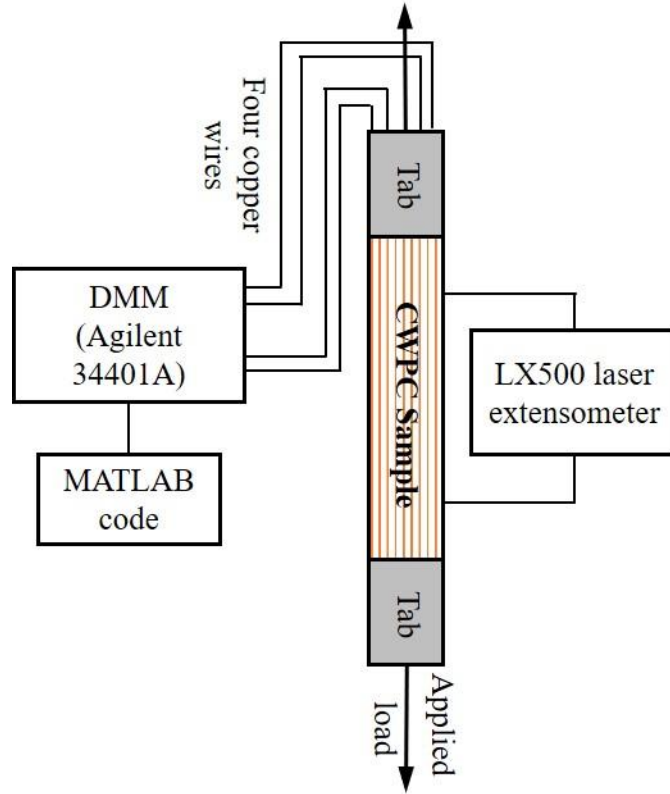


Figure 3-4. Schematic representation of the electromechanical testing setup.

To determine the sensitivity of the wire sensors, the GF was calculated as shown in Equation 3.1. The GF correlates the fractional change of the electrical resistance, calculated as shown in Equation 3.3 [8], and the applied strain obtained from the laser extensometer readings.

$$Fractional\ change\ of\ electrical\ resistance\ (\Delta R/R) = \frac{R_i - R}{R} \qquad (3.3)$$

where $R_i$ is the measured resistance of the sample during loading and $R$ is the initial resistance of sample before loading.

The ultimate tensile strength, *UTS*, and Young's modulus properties were analyzed statistically by an independent samples T-test to examine the significance of these properties for the CWPC samples compared to standard 3D printed PLA material samples. For all cases, statistical significance was considered accepted at a confidence level of 95% ($p < 0.05$).

### 3.2.4. Microscopic Imaging

The samples were cross-sectioned and examined under an optical microscope to quantify volume faction of wire in the printed components. Samples were mounted in a clear resin (Amazing clear cast, Alumilite Corp, USA) in a 28 mm inner diameter mold and cured for 24 hours. The printed sample was sectioned using high-speed cutting machine (Mecatome T260, PRESI, Hungary). The sample surface was prepared using a grinding and polishing machine (StarGrind™ 200-2V, Microstar 2000, Canada) through four steps of grinding using 180, 280, 400, and 600 grit silicon carbide papers followed by one step of polishing with suspension of 1 μm alumina particle at a rotational speed of 300 rpm. Volume fraction of all constituents of polymer composite were measured optically using optical stereomicroscope (LEICA MZ10 F, LEICA, Germany) with 50x magnification. Finally, the captured images were processed using an open-source software (ImageJ, National Institutes of Health, Bethesda, Maryland, USA) to obtain measurements of the volume fraction. The failure area after breakage of the sample was investigated using the same microscope at a magnification of 10x.

## 3.3. Analytical Modelling

To predict the mechanical and electrical properties of CWPC samples, analytical models were developed for comparison with the obtained experimental data.

### 3.3.1. Mechanical Model

To predict the mechanical properties of continuous wire reinforced polymer composite, rule of mixture (ROM) analytical model was applied [2,6]. To evaluate both the UTS and Young's modulus as shown in Equation 3.4, volume fraction and properties of each constituent should be identified first. Table 3-2 shows the assumed values of the UTS and Young's modulus for both Cu wire and NiCr wire [21]. For the 3D printed structure, the voids are frequently occurred in the structure. In this respect, some researchers [6,22] modified the properties of the matrix to take the existence of the voids into account as shown in Equation 3.5.

$$\sigma_c = V_w \sigma_w + V_p \sigma_p \qquad\qquad (3.4\text{-a})$$

$$E_c = V_w E_w + V_p E_p \qquad\qquad (3.4\text{-b})$$

where $\sigma_c$, $\sigma_w$, and $\sigma_p$ are the UTS of composite, wire, and polymer, respectively. $E_c$, $E_w$, and $E_p$ are Youngs' modulus of composite, wire, and polymer, respectively. $V_w$ and $V_p$ are the volume fractions for both wire and polymer, respectively.

Table 3-2. Mechanical properties of Cu and NiCr wires.

| Material | Material Properties | |
|---|---|---|
| | Young's modulus | UTS |
| Cu wire | 110 GPa | 210 MPa |
| NiCr wire | 200 GPa | 689 MPa |

$$\sigma_p = (1 - V_v)\sigma_{pe} \qquad\qquad (3.5\text{-a})$$

$$E_p = (1 - V_v)E_{pe} \qquad\qquad (3.5\text{-b})$$

where $\sigma_{pe}$ and $E_{pe}$ are the experimental values of UTS and Young's modulus of PLA, respectively. And $V_v$ is the volume fraction of the voids obtained from the microscopic investigation.

To identify the volume fractions used in the ROM model, the theoretical volume fraction of both wire and polymer was calculated from the measurements of the final geometry of the sample as shown in Equation 3.6.

$$v_w = L_{wire} * A_{wire} = (L_{wire/raster} * no.\,of\,rasters * no.\,of\,layers) * (\pi/4)D_{wire}^2 \qquad \text{(3.6-a)}$$

$$v_c = l * w * t \qquad \text{(3.6-b)}$$

$$v_p = v_c - v_w \qquad \text{(3.6-c)}$$

$$V_w = \frac{v_w}{v_c} \qquad \text{(3.6-d)}$$

$$V_p = \frac{v_p}{v_c} \qquad \text{(3.6-e)}$$

where $v_w$, $v_c$, and $v_p$ are the volume of wire, composite, and polymer, respectively. $L_{wire}$, $A_{wire}$, and $D_{wire}$ are the initial length, the cross-section area, and the diameter of the wire, respectively. $L_{wire/raster}$ is the initial length of the wire in a single raster. $l$, $w$, and $t$ are the total length, width, and thickness of the 3D printed sample, respectively.

### 3.3.2.  Gauge Factor Model

To predict the values of the GF for both Cu wire and NiCr CWPCs, an analytical model based on the electrical resistance equation (Equation 3.2) was applied. In this equation, the resistivity of the wire was assumed to be constant over the applied strain and the instantaneous length of the wire was assumed to be the length in the region between the grips as shown in Figure 3-3 as the sample under the grips does not experience tensile strain only.

In this model, the electrical resistance was calculated based on the instantaneous values of the extension of the sample as shown in Equation 3.7. Afterwards, Equation 3.1 was applied to

calculate the GF. It should be noted that the value of the resistivity of both Cu and NiCr wire was calculated using the initial dimensions of the wire, $L_{wire}$ and $A_{wire}$, and the initial reading of the resistance, $R$, of the unstrained 3D printed sample using Equation 3.2.

$$L_{wire} = L_{wire/raster} * no.of\ rasters * no.of\ layers \tag{3.7-a}$$

$$V_w = L_{wire} * A_{wire} \tag{3.7-b}$$

$$L_i = L_{wire} + (\Delta_i * no.of\ rasters * no.of\ layers) \tag{3.7-c}$$

$$A_i = \frac{V_w}{L_i} \tag{3.7-d}$$

$$R_i = \frac{\rho L_i}{A_i} \tag{3.7-e}$$

where $L_i$, $A_i$, and $R_i$ are instantaneous values of the wire length, area, and electrical resistance, respectively, corresponding to the applied extension, $\Delta_i$.

Statistical significance between experimental and analytical GF results, a paired sample T-test was conducted. Statistical significance was considered accepted at a confidence level of 95% ($p <$ *0.05*).

## 3.4. Results and Discussion

### 3.4.1. Optical Microscopy

The microstructure study showed a uniform distribution of the wire within the composite as seen in Figure 3-5. This figure shows the cross-section of the 3D printed continuous wire reinforced PLA composite. It can be shown that voids mostly exist around the wires. Voids occur due to the extruded polymer geometry. This observation was also reported by Ibrahim et al. and Ahn et al. [2,9,23] . The processed optical microscope images using ImageJ software were used to calculate

the volume fraction of both wire and voids within the fabricated composite as indicated in Table 3-3. Figure 3-6a addresses the processed images using threshold tools to first calculate the volume fraction of both wires and voids, $V_w\% + V_v\%$, together and then the volume fraction of the wires alone, $V_w\%$, was calculated as shown in Figure 3-6b. From the two previous measurements, the volume fraction of the voids, $V_v\%$, was obtained.
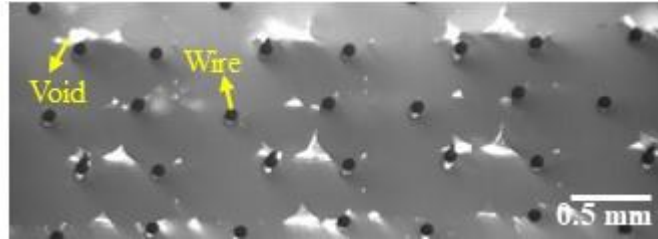


Figure 3-5. Cross-section microscopy of wire reinforced PLA composite.
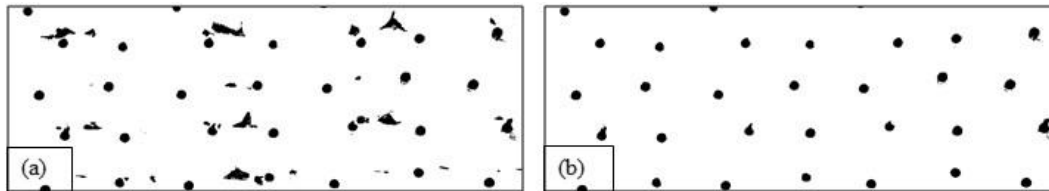


Figure 3-6. Processed images to calculate volume fraction of; a) wire + void, b) wire only.

Table 3-3. Volume fraction of composite constituent.

|  | Cu wire reinforced PLA composite | NiCr wire reinforced PLA composite |
|---|---|---|
| **PLA ($V_p\%$)** | 95.48 | 96.16 |
| **Wire ($V_w\%$)** | 2.37 | 1.83 |
| **Void ($V_v\%$)** | 2.15 | 2.01 |

Table 3-3 shows that the $V_w\%$ for the Cu wire reinforced PLA composite is higher than that for NiCr wire reinforced PLA composite. This may be attributed to the higher diameter of the Cu wire compared to NiCr which was measured using flat anvil digital micrometer (Mitutoyo, Canada).

The diameters of the Cu wire and NiCr wire were found to be 82 μm and 75 μm, respectively, and the higher diameter of the Cu wire is due to the coated layer of polyimide which has a melting temperature of about 350 °C. This melting temperature of polyimide is much higher than the printing temperature of PLA used in this study (170 °C) indicating that the coated layer was included with Cu wires for the volume fractions measurements after printing process.

### 3.4.2. Mechanical Properties

The stress-strain curves for the Cu wire and NiCr CWPCs are shown in Figure 3-7. Here the value of the stress increased gradually with applied tensile strain before decreasing rapidly indicating a brittle fracture of these composites. Figure 3-8 presents the UTS and Young's modulus of the wire reinforced PLA composites compared to printed PLA. It can be noted that the average UTS and Young's modulus were found to be 44.89 ±1.82 and 53.8 ±4.35 MPa and 3.3515 ±0.3726 and 4.714 ±0.1327 GPa for Cu wire and NiCr wire PLA composites, respectively. The higher values of the mechanical properties for the NiCr PLA composite may be attributed to the higher mechanical properties of NiCr material compared to Cu as indicated in Table 3-2. The UTS and Young's modulus were improved by 13.5% and 54%, respectively, compared to PLA by using NiCr wire. These results are similar to those measured by Ibrahim et al. [2].
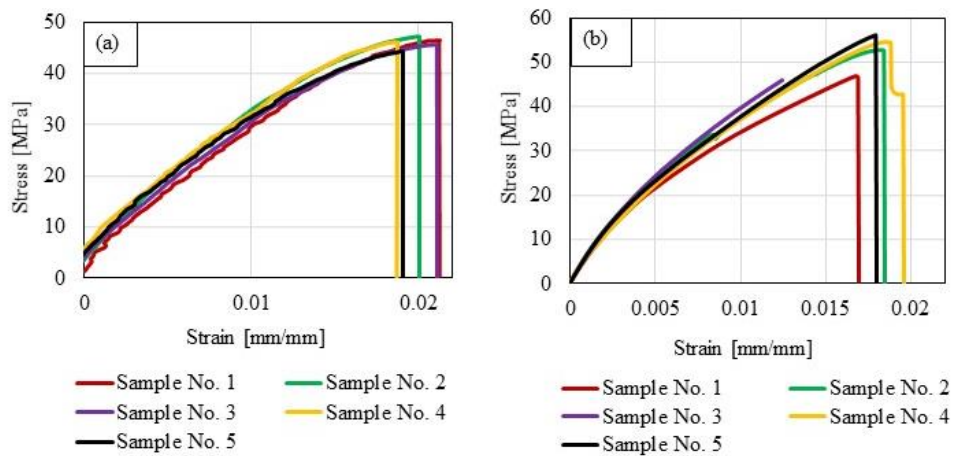


Figure 3-7. Stress-Strain curve of; a) Cu wire, b) NiCr wire reinforced PLA composite.

56
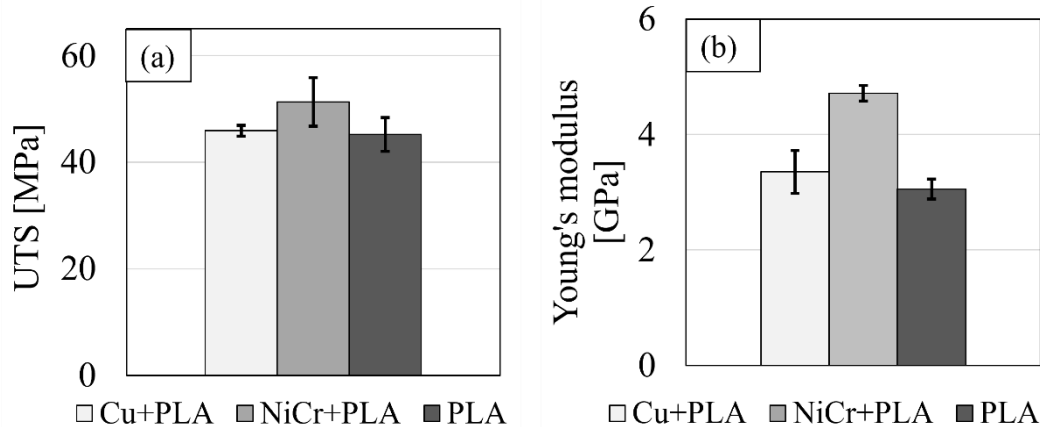
Figure 3-8. Mechanical properties of Cu and NiCr wire reinforced PLA composite; a) UTS, b) Young's modulus.

Table 3-4 presents the results of the statistical study in terms of p-value for the mechanical properties to examine the significance between the UTS and Young's modulus of PLA compared to composites results. It can be shown that Cu wire reinforced PLA composite gave no significance with the pure PLA results for both UTS and Young's modulus. While NiCr wire reinforced PLA composite showed a significant difference between its mechanical properties and PLA properties.

Table 3-4. Statistical study of mechanical properties for PLA and wire composites.

|  | p-value | |
|---|---|---|
|  | UTS | Young's modulus |
| Between PLA and Cu+PLA | 0.666 | 0.158 |
| Between PLA and NiCr+PLA | 0.043 | $6.2*10^{-7}$ |

### 3.4.3. Mechanical Model Results

The volume fraction of each constituent was calculated using Equation 3.6 for the ROM model. The theoretical volume fractions of both PLA and wires were found to be 98.66% and 1.34%, respectively. A comparison between the experimental and theoretical values of UTS and Young's modulus in shown in Figure 3-9. Overall, the predicted values are higher than the experimentally measured values and this may be attributed to the basic assumptions that ROM based on such as

the perfect adhesion between matrix and fibers and the nonexistence of voids within the structure which are not the cases for the 3D printed composites. Moreover, Melenka et al. [6] found that for the low fiber volume fraction (4%), there is less agreement between experimental and predicted properties for Kevlar reinforced nylon 3D printed composite.
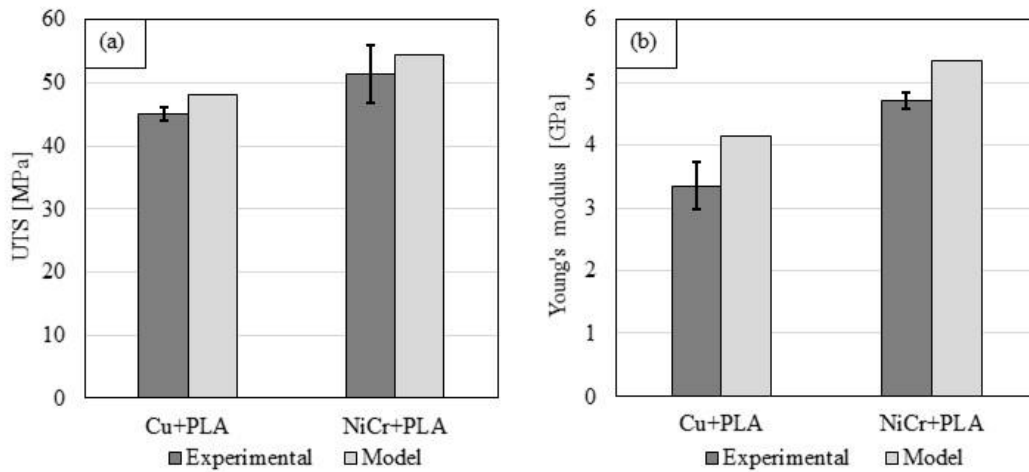


Figure 3-9. Experimental and analytical model results of mechanical properties of Cu wire and NiCr wire reinforced PLA composite; a) UTS, b) Young's modulus.

### 3.4.4. Electromechanical Properties

The relative change in electrical resistance induced during tensile strain is shown in Figure 3-10. Here the elongation and area reduction within the wires governed by Equation 3.2 results in an increase in the electrical resistance until fracture for both CWPC samples.

Similar results were reported by several researchers [10,11,24], who presented a direct relationship between applied strain and electrical resistance for different types of materials used as sensors within polymer composites. These included nanometallic nickel coated glass fiber within glass fiber reinforced epoxy composite, nichrome wire within glass fiber reinforced epoxy composite, and printed pattern of carbon ink on polyethylene-terephthalate (PET) substrate.
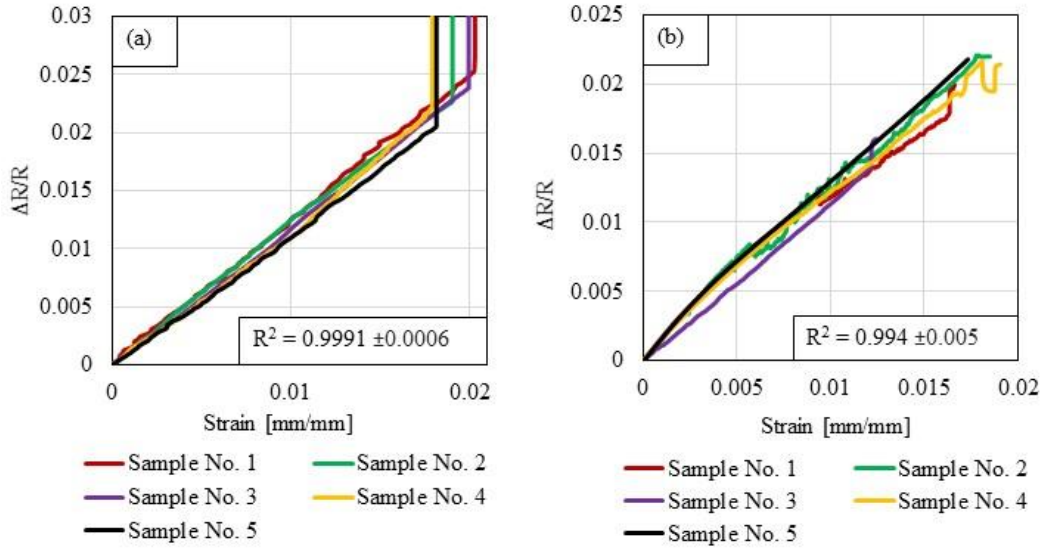
Figure 3-10. Plot of ($\Delta R/R\text{-}\varepsilon$) curve; a) Cu wire, b) NiCr wire reinforced PLA composite.

This direct relationship between the fractional change in resistance and strain indicates the ability of both Cu and NiCr wires to act as a sensing element within the CWPC to measure stress/strain in the real time and hence predict the deformation and damage induced in the composite structure. The values of $R^2$ for the relation between the strain and the fractional change in electrical resistance, as shown in Figure 3-10, demonstrates the very linear relation between strain and resistance change for both sets of CWPCs.

Figure 3-10a shows that there is a sudden increase in the value of the electrical resistance by several orders of magnitude after failure, indicating a loss of connectivity of the Cu wire due to its physical fracture as illustrated in Figure 3-11a. Similar results were also reported for nickel coated glass fiber embedded in glass fiber reinforced epoxy [10] and for Nichrome (NiCr) and nickel alloy wires used as sensors in polymer composite [11]. However, for the NiCr CWPC, the value of the resistance continues to increase gradually until failure occurred (Figure 3-10b) indicating only matrix breakage as shown in Figure 3-11b.

The breakage of Cu wire indicates that there is improved adhesion between Cu wire and PLA compared to NiCr wire with PLA and this may be attributed to polyimide coating layer on Cu wire which may serve to enhance the bonding at elevated temperature during the printing process. Therefore, the results obtained of resistance measurements can be used also for further investigation of failure and damage mechanism in polymer composites in terms of matrix or fibers failure.
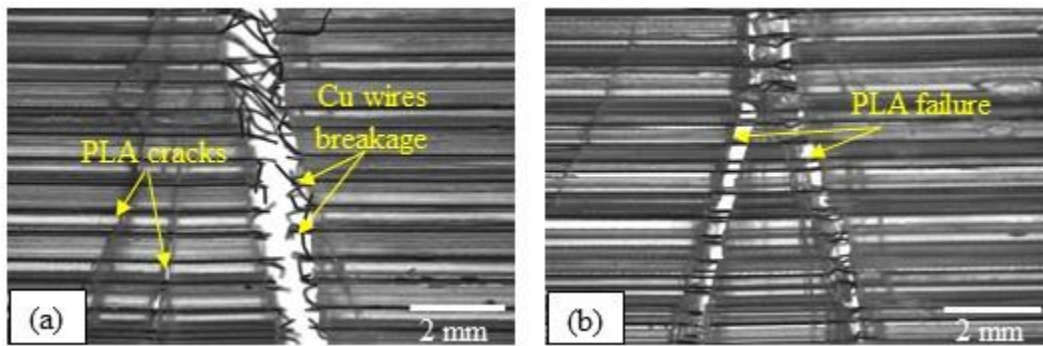


Figure 3-11. Failure section microscopy of; a) Cu wire, b) NiCr wire reinforced PLA composite.

The NiCr CWPC samples presented other challenges in terms of obtaining reliable electromechanical results. Some samples demonstrated fluctuations in electrical resistance during strain and this may be attributed to internal shorting of the NiCr wire circuit within the CWPC itself. Similar resistance measurement issues were not observed with the coated Cu CWPC samples. Although, the measurements were recorded only for one layer as mentioned in Sec. 3.2.1, a short circuit could also occur between the uninsulated wire and the conductive metal frame of the testing machine and cause a sudden drop in the measured resistance. In this respect, it is recommended to use insulated wire for such electrical sensing applications to avoid conductivity issues.

### 3.4.5.  Gauge Factor

To examine the sensitivity of the CWPC sensors, the slope of ($\Delta R/R$-$\varepsilon$) curve was calculated to obtain the GF of the CWPC samples [25].  Figure 3-12 shows the value of the measured GFs (as obtained by Equation 3.1) for the Cu and NiCr CWPC samples. The values of GFs were found to be 1.17 ±0.06 and 1.13 ±0.07 for Cu wire and NiCr wire reinforced PLA composites, respectively.

These experimental results of GF for both Cu and NiCr wire CWPCs were compared with the analytical values calculated as discussed in Sec. 3.3.2. As shown in Equation 3.7 (e), the electrical resistance was calculated based on the experimental applied tensile extension. Therefore, there is a little variation between the calculated GF for each sample as indicated by the error bars on the columns of the model in Figure 3-12. From the initial reading of the resistance of the samples and from the geometry of the wire, the average value of the resistivity for both Cu wire and NiCr wire was calculated and found to be $1.74 \times 10^{-8}$ ±$8.8 \times 10^{-11}$ $\Omega$m and $1.04 \times 10^{-6}$ ±$4.3 \times 10^{-9}$ $\Omega$m, respectively. Figure 3-12 shows a good agreement between experimental and analytical results for Cu and NiCr wire reinforced PLA composite. This finding was verified by the statistical study through conducting a t-test (paired sample T-test) which showed no significance between the experimental and the analytical values with obtained ($p = 0.33$) and ($p = 0.064$) for Cu wire and NiCr wire reinforced PLA composite, respectively. This statistical insignificance between predicted and experimental values confirms the credibility of this analytical model to be used to predict the GF values for unidirectional wire reinforced polymer composites. In other words, this analytical model can be used to predict the sensitivity and therefore to design functionalized 3D printed unidirectional CWPC strain sensors for different real-world applications.
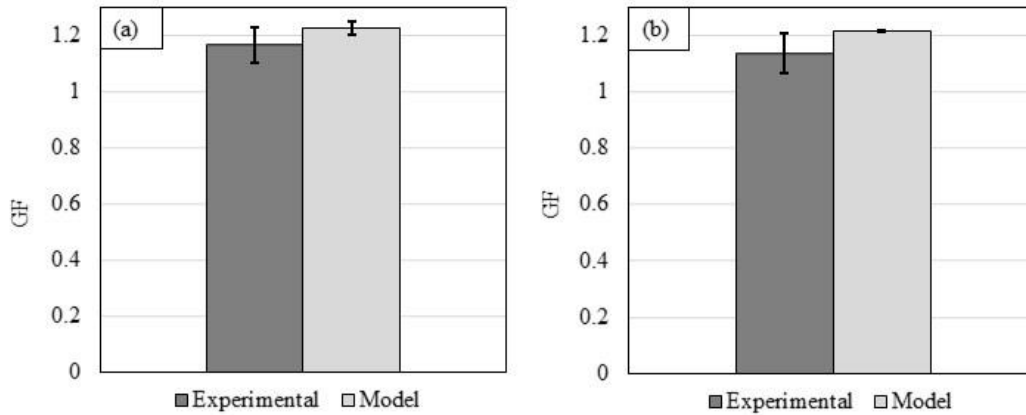
Figure 3-12. Gauge factor of; a) Cu wire, b) NiCr wire reinforced PLA composite.

To sum up, in terms of electromechanical properties, both Cu and NiCr showed very close sensitivity (gauge factor) as shown in Figure 3-12. In terms of mechanical properties, the NiCr samples showed a significance increase in UTS and Young's modulus compared to the pure PLA while Cu samples did not show significance in improving mechanical properties. However, NiCr wire still contends with short circuits problem as it is not commercially available with coated layer unlike Cu wire.

### 3.4.6. Cyclic Loading

To test the reliability of the wire sensor in the polymer composite, a cyclic loading tensile test was conducted using the same universal testing frame with minimum and maximum load of 100 N and 1000 N, respectively, and at a constant crosshead speed of 0.5 mm/min for loading and unloading. This applied load range was chosen to be in the elastic deformation region of the sample. The test was conducted for ten cycles as mentioned by several researchers [11,17,26]. The fractional change in the electrical resistance was measured simultaneously using the same procedure as described previously for ten loading-unloading cycles.

Figure 3-13 shows the electrical and mechanical response of the Cu CWPC sample to the repeated

cyclic loading for ten cycles. As illustrated in Figure 3-13, upon applying the axial load up to 1000

N, the electrical resistance of the Cu wire increased linearly before being reduced again to nearly

its original value upon load removal. This phenomenon was also observed by Balaji and Sasikumar

[11] and Teixeira et al. [17]. Moreover, it can be shown that the change of maximum, $\Delta R/R$, was

minimal indicating that the Cu wire has a repeatable and reversible response during the cyclic

loading. Lu et al. [25] reported similar behavior for graphene platelets/epoxy flexible sensor. On

the other hand, there is more variation in the strain values over the ten cycles due to the hysteresis

phenomenon as shown in Figure 3-14.
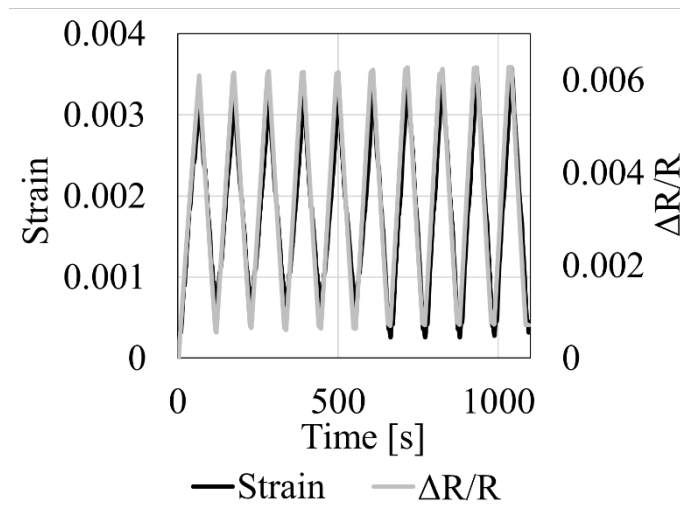


Figure 3-13. Mechanical and electrical response of Cu wire reinforced PLA composite under

tensile cyclic loading.

Figure 3-14 shows the hysteresis loop phenomenon of Cu CWPC sample during loading and

unloading. From Figure 3-14a, the hysteresis loop area confined by the loading and unloading

curve for each cycle was calculated using customized code on MATLAB software (Figure 3-15).

The average value was $1.962 \times 10^{-3} \pm 0.533 \times 10^{-3}$ MPa for the stress-strain curve (Figure 3-15a)

representing the dissipated energy, usually as a heat, and the value of the reversed deformation due

to friction and the structural changes within the polymer molecular chains [27,28]. It should be noted that, for composite material, the energy is mostly dissipated by the less stiff component, and this was confirmed by the calculation of the hysteresis loop area for pure 3D printed PLA sample when subjected to tensile-tensile cyclic loading test under the same loading conditions. It was found that the average value of the areas for each cycle is $2.276 \times 10^{-3} \pm 0.476 \times 10^{-3}$ MPa. This result is highly comparable to the result for Cu CWPC, indicating that the energy is mainly dissipated primarily by the PLA component of the composite. As shown in Figure 3-15a, the hysteresis loop area for Cu CWPC increased with the number of cycles indicating more energy loss with the number of cycles. This trend is similar to what was presented in literature by Shukla et al. [29] who found that the hysteresis loop area increased from 1.5 to 4 N.mm after 3500 cycles for carbon nanotube reinforced Polypropylene composite (CNT-PP). The small hysteresis loop shift represents the value of the deformation accumulated over the ten cycles [27]. Similarly, for the sensing property, there is hysteresis error as shown in Figure 3-15b with the average hysteresis loop area of $2.29 \times 10^{-6} \pm 9.88 \times 10^{-7}$. Figure 3-15b also depicted that the hysteresis loop area for Cu wire reinforced PLA composite increased with the number of cycles due to more energy losses as mentioned before.

The sudden increase in the hysteresis loop area at seventh cycle (Figure 3-15a and b) indicates more strain happened to the material. This sudden increase in the area correlates to the changes in the structure of the Cu wire as pure PLA showed a gradual increase in the hysteresis loop area with number of cycles as shown in Figure 3-15c. This behavior of sudden increase in strain was observed by several researchers studying the fatigue behavior of metals [30,31]. It was correlated to the strain ratcheting phenomenon occurred to the material under stress controlled uniaxial cyclic loading test with non-zero mean stress. This phenomenon results from strain accumulation under

low to intermediate cyclic fatigue regime and it is associated with dislocations movement within the metal [30–32].
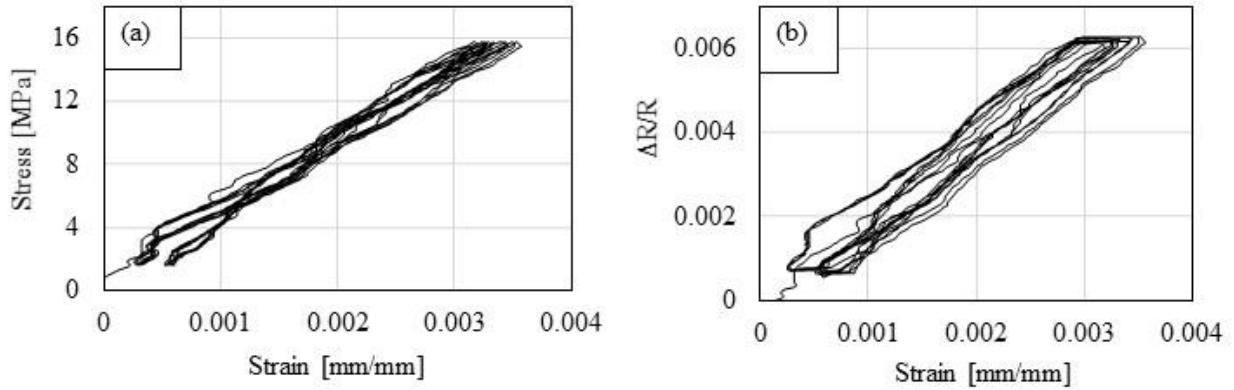


Figure 3-14. Hysteresis loop of; a) stress-strain curve, b) ($\Delta R/R$-$\varepsilon$) curve of Cu wire reinforced PLA composite.
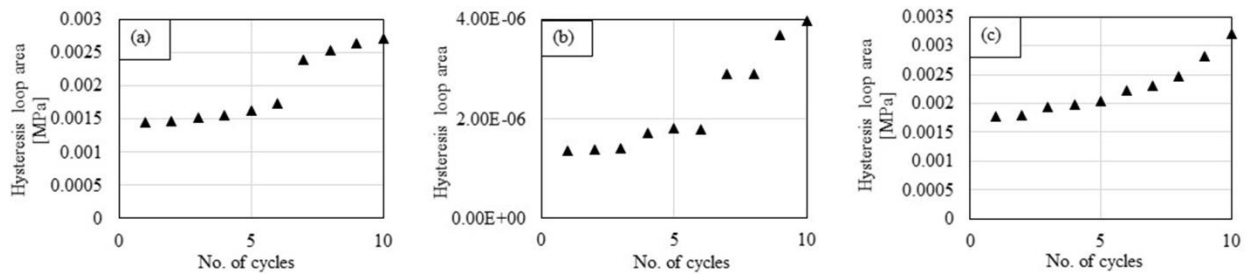


Figure 3-15. Hysteresis loop area after 10 cycles for; a) stress-strain curve of Cu wire reinforced PLA composite, b) ($\Delta R/R$-$\varepsilon$) curve of Cu wire reinforced PLA composite, c) stress-strain curve of PLA.

## 3.5. Summary and Conclusions

The electromechanical behavior of 3D printed unidirectional Cu and NiCr CWPC components were electromechanically characterized to understand how they would function for SHM applications.

The 3D printed CWPCs demonstrated improved mechanical properties compared to pure 3D printed PLA, especially for the NiCr wire reinforced PLA composite which showed an increase of 13.5% and 54% in UTS and Young's modulus, respectively. The predicted mechanical properties applying ROM was higher than the experimentally measured values due the assumptions of the ROM theory—namely the perfect adhesion between matrix and fibers and the nonexistence of voids within the structure.

There was a direct linear relationship observed between the applied tensile strain and the measured electrical resistance for both Cu wire and NiCr CWPCs indicating the ability of these wires to be used as a sensor to measure stress/strain in the real time and hence predict the deformation and damage induced in the composite structure. The GF of the printed samples can also be reliably predicted based on the geometry and resistive properties of the reinforcing wire and matrix material. The GFs of Cu wire and NiCr CWPCs were strongly agreed with the predicted values.

The uncoated NiCr CWPC demonstrated some inconsistencies in the measured resistance, and it is believed this is due to a short circuit occurred between the uncoated wire and the metallic frame of the testing machine. Therefore, it is recommended to use coated wires for such electrical sensing applications.

The reliability of the wire as a sensor within PLA composite was verified by conducting a cyclic loading test for Cu CWPC sample. The results showed the occurrence of hysteresis phenomenon indicating the dissipation of energy primarily by the PLA component of the composite.

We have demonstrated 3D printed continuous wire polymer composites (CWPCs) can serve as 3D printed strain sensors and could be used to develop multi-functional CWPCs with effective sensing capabilities under real time loading conditions for structural health monitoring applications. This

fabrication approach also provides the design flexibility required to produce functionalized 3D printed components for applications such as biomedical implants or aircraft components for in-situ monitoring the behavior of the part.

## 3.6.   References

[1]   Goh GD, Dikshit V, Nagalingam AP, Goh GL, Agarwala S, Sing SL, et al. Characterization of mechanical properties and fracture mode of additively manufactured carbon fiber and glass fiber reinforced thermoplastics. Mater Des. 2018;137:79–89. https://doi.org/10.1016/j.matdes.2017.10.021

[2]   Ibrahim Y, Melenka GW, Kempers R. Fabrication and tensile testing of 3D printed continuous wire polymer composites, Rapid Prototyp. J. 2018; 24:1131–1141. https://doi.org/10.1108/RPJ-11-2017-0222.

[3]   Mattner T, Körbel W, Wrensch M, Drummer D. Compensation of edge effects in picture frame testing of continuous fiber reinforced thermoplastics. Compos Part B Eng. 2018;142(December 2017):95–101.

[4]   Yang C, Tian X, Liu T, Cao Y, Li D. 3D printing for continuous fiber reinforced thermoplastic composites: Mechanism and performance. Rapid Prototyp J. 2017;23(1):209–15.

[5]   Dawoud M, Taha I, Ebeid SJ. Mechanical behaviour of ABS: An experimental study using FDM and injection moulding techniques. J Manuf Process [Internet]. 2016;21:39–45. Available from: http://dx.doi.org/10.1016/j.jmapro.2015.11.002

[6]   Melenka GW, Cheung BKO, Schofield JS, Dawson MR, Carey JP. Evaluation and

prediction of the tensile properties of continuous fiber-reinforced 3D printed structures. Compos Struct [Internet]. 2016;153:866–75. Available from: http://dx.doi.org/10.1016/j.compstruct.2016.07.018

[7]     Hofstätter T, Pedersen DB, Tosello G, Hansen HN. State-of-the-art of fiber-reinforced polymers in additive manufacturing technologies. J Reinf Plast Compos. 2017;36(15):1061–73.

[8]     Matsuzaki R, Ueda M, Namiki M, Jeong TK, Asahara H, Horiguchi K, et al. Three-dimensional printing of continuous-fiber composites by in-nozzle impregnation. Sci Rep. 2016;6:1–7.

[9]     Ibrahim Y, Melenka GW, Kempers R. Additive manufacturing of Continuous Wire Polymer Composites. Manuf Lett [Internet]. 2018;16:49–51. Available from: https://doi.org/10.1016/j.mfglet.2018.04.001

[10]    Balaji R, Sasikumar M. A nanometallic nickel-coated, glass-fibre-based structural health monitoring system for polymer composites. Smart Mater Struct. 2017;26(9).

[11]    Balaji R, Sasikumar M. Development of strain and damage monitoring system for polymer composites with embedded nickel alloys. Meas J Int Meas Confed [Internet]. 2017;111(August):307–15. Available from: http://dx.doi.org/10.1016/j.measurement.2017.07.036

[12]    Lee G, Kim M, Yoon H, Yang J, Ihn J, Ahn S. Direct printing of strain sensors via nanoparticle printer for the applications to composite structural health monitoring. Procedia CIRP [Internet]. 2017;66:238–42. Available from: http://dx.doi.org/10.1016/j.procir.2017.03.279

[13]     Wen J, Xia Z, Choy F. Composites : Part B Damage detection of carbon fiber reinforced polymer composites via electrical resistance measurement. 2011;42:77–86.

[14]     Balaji R, Sasikumar M. Graphene based strain and damage prediction system for polymer composites. Compos Part A Appl Sci Manuf [Internet]. 2017;103:48–59. Available from: https://doi.org/10.1016/j.compositesa.2017.09.006

[15]     Johnson TM, Fullwood DT, Hansen G. Strain monitoring of carbon fiber composite via embedded nickel nano-particles. Compos Part B Eng. 2012;43(3):1155–63.

[16]     Park JB, Okabe T, Takeda N. New concept for modeling the electromechanical behavior of unidirectional carbon-fiber-reinforced plastic under tensile loading. Smart Mater Struct. 2003;12(1):105–14.

[17]     Teixeira J, Horta-Romarís L, Abad MJ, Costa P, Lanceros-Méndez S. Piezoresistive response of extruded polyaniline/(styrene-butadiene-styrene) polymer blends for force and deformation sensors. Mater Des [Internet]. 2018;141:1–8. Available from: https://doi.org/10.1016/j.matdes.2017.12.011

[18]     Lu Y, Biswas MC, Guo Z, Jeon W, Wujcik EK. Recent Developments in Bio-monitoring via Advanced Polymer Nanocomposite-based Wearable Strain Sensors. Accepted Manuscript. Biosens Bioelectron [Internet]. 2018; Available from: https://doi.org/10.1016/j.bios.2018.08.037

[19]     Ogi K, Takao Y. Characterization of piezoresistance behavior in a CFRP unidirectional laminate. Compos Sci Technol. 2005;65(2):231–9.

[20]     Alexander JH, Schneider J, Myers Z. Feasibility of multi-walled carbon nanotube / epoxy

thermoset-based strain sensors for sensing in structural applications. 2017;

[21]    Online Materials Information Resource - MatWeb [Internet]. [cited 2018 Jul 23]. Available from: http://www.matweb.com/

[22]    Rodriguezjames JF, Renaud PTE, Rodriguez JF, Thomas JP, Renaud JE. Characterization of the mesostructure of styrene materials. 2002;

[23]    Ahn D, Kweon JH, Kwon S, Song J, Lee S. Representation of surface roughness in fused deposition modeling. J Mater Process Technol. 2009;209(15–16):5593–600.

[24]    Zhang Y, Aeronautics N, Anderson N, Bland S, Engineer L, Aeronautics N, et al. All-printed Strain Sensors : Building Blocks of the Aircraft Structural Health Monitoring System. Sensors Actuators A Phys [Internet]. 2016; Available from: http://dx.doi.org/10.1016/j.sna.2016.10.007

[25]    Lu S, Tian C, Wang X, Zhang L, Du K, Ma K, et al. Strain sensing behaviors of GnPs/epoxy sensor and health monitoring for composite materials under monotonic tensile and cyclic deformation. Compos Sci Technol [Internet]. 2018;158:94–100. Available from: https://doi.org/10.1016/j.compscitech.2018.02.017

[26]    Hu C, Li Z, Wang Y, Gao J, Dai K, Zheng G. Comparative assessment of the strain-sensing behaviors of polylactic acid nanocomposites : reduced graphene oxide or carbon nanotubes †. 2017;2318–28.

[27]    Senatov FS, Niaza K V, Stepashkin AA, Kaloshkin SD. Low-cycle fatigue behavior of 3d-printed PLA-based porous scaffolds. 2016;97:193–200.

[28]    Shyr T, Shie J, Jhuang Y, Materials C. The Effect of Tensile Hysteresis and Contact

Resistance on the Performance of Strain-Resistant Elastic - Conductive Webbing. 2011;1693–705.

[29]   Shukla RS, Mertens J, Senthilvelan S. Hysteresis Heating of Polypropylene Based Composites. 2014;(Aimtdr):1–6.

[30]   Maier HJ, Gabor P, Karaman I. Cyclic stress – strain response and low-cycle fatigue damage in ultrafine grained copper. 2005;411:457–61.

[31]   Lim C, Kim KS, Seong JB. Ratcheting and fatigue behavior of a copper alloy under uniaxial cyclic loading with mean stress. Int J Fatigue [Internet]. 2009;31(3):501–7. Available from: http://dx.doi.org/10.1016/j.ijfatigue.2008.04.008

[32]   Kumar S, Sivaprasad S, Dhar S, Tarafder S. Ratcheting and low cycle fatigue behavior of SA333 steel and their life prediction. J Nucl Mater [Internet]. 2010;401(1–3):17–24. Available from: http://dx.doi.org/10.1016/j.jnucmat.2010.03.014

# Chapter 4    A Comparative Study on the Electromechanical Properties of 3D-Printed Rigid and Flexible Continuous Wire Polymer Composites for Structural Health Monitoring

In this chapter, the electromechanical properties of two different three-dimensional (3D) printed continuous wire polymer composites (CWPC) were characterized and compared. The two composite materials were copper wire polylactic acid (PLA) composite (rigid material) and copper wire thermoplastic polyurethane (TPU) composite (flexible material). The electromechanical measurements were based on piezoresistive properties of the sensor at which the mechanical strain and the electrical resistance were correlated under a uniaxial loading condition. Both types of materials exhibited a direct linear relationship between the two quantities, indicating the ability of CWPC to be used for strain sensing applications. The gauge factor (GF) sensitivity was compared for the two types of materials. It was found that there is no statistical significance difference between the GF of PLA CWPC (1.36 ±0.14) and TPU CWPC (1.29 ±0.07)); therefore, the sensing property depends mainly on the wire integrated into the 3D-printed structure rather than the matrix. Thus, different matrices can be used to fit different applications. An analytical model for GF showed agreement with the experimental results for both materials. TPU CWPC showed significant improvement in both Young's modulus, $E$, and ultimate tensile strength, $UTS$, (210.5% and 31.86%, respectively), compared with pure TPU, while the change in Poisson's ratio, $v$, was

insignificant. Young's modulus of PLA CWPC was significantly increased by 80.3% compared with PLA, while *UTS* and *v* did not significantly change. The experimental mechanical properties showed good agreement with data from the analytical models. The outcome of this study focused on the manufacturing of 3D-printed functionalized structure for strain sensing applications with improved mechanical properties. The wide range of attained strain allowed their use in different applications based on the range of strain needed, such as rigid sports equipment and flexible wearable sensors.

## 4.1.  Introduction

Polymer matrix composites (PMC) have received growing attention in the past few decades due to their strength and light weight. They have been extensively used in industrial fields such as automotive, astronautics, and aeronautics [1]. For these sectors, composites must retain their required mechanical properties while subjected to harsh environmental conditions such as radiation, corrosion, and thermal aging. Therefore, there should be an efficient and reliable method to check part performance during service. Polymer composites with sensing capabilities are extremely favourable for real-time and in-situ structural health monitoring (SHM) [1,2]. SHM is important for safety issues because it continuously monitors the composite under mechanical loading for any deformation, including internal change, damage or failure, thus increasing the life cycle of the product [3–5].

Different processing techniques have been used to produce conductive polymer composites by incorporating various conductive fillers such as copper, aluminum, graphite, carbon nanotubes, carbon fibers, and graphene. The processing techniques studied in the literature are magnetic stirring, template methods, and melt processing [6,7]. Although these methods are cost-effective,

they can not rapidly produce complex geometries with customizable sensing capabilities. Additionally, these methods are not suitable for large-scale production. Additive manufacturing (AM) is an emerging technology which can fabricate complex three-dimensional geometries. Among various AM techniques, extrusion-based AM is a promising process because of its simplicity and cost-effectiveness. Fused filament fabrication (FFF) is a solid-state extrusion-based AM process that uses polymer filament to fabricate three-dimensional structures [8].

To date, most extrusion-based AM research has focused on relatively rigid polymers such as polylactic acid (PLA) and acrylonitrile butadiene styrene (ABS). However, flexible polymers offer a more comprehensive range of strains and low elastic modulus, which could broaden the scope of sensing applications such as pressure sensors, displays, flexible circuits, wearable sensors, and piezoresistors. The development of flexible sensory composites allows for their use in next-generation Internet of Things (IOT) technology for human–machine interfacing [2,8]. Despite advantages, printing parts using a flexible filament of rubber-like materials still presents challenges such as filament buckling. Thus, there is a need to develop a reliable, economically, and simple method to fabricate flexible sensory composites [8].

The use of flexible polymer in sensing applications has been investigated by several researchers [2,8–10]. For instance, Bertolini et al. [9] studied the conductivity of carbon black-polypyrrole (CB-PPy) particle reinforced poly(vinylidene fluoride)/thermoplastic polyurethane (PVDF/TPU) 3D-printed flexible composite. They compared the effects of FFF and compression molding processes on the conductivity of the composite. Qureshi et al. [11] used a flexible strain sensor in the form of wire made of conductive silver nanoparticles deposited on the surface of nylon yarn. This single wire was further embedded in a glass-fiber-reinforced resin composite for resistance measurements under flexural loading. However, to date, there have been no studies of strain

74

sensors with wires integrated within the part to enhance the mechanical properties while performing as a sensor. Therefore, a 3D-printed continuous wire reinforced flexible polymer composite presents interesting opportunities with regard to broadening the scope of sensing applications.

For sensing applications, there are different mechanisms for electromechanical strain sensing, such as capacitance, piezoresistance, and inductance. Strain sensors based on capacitance and inductance have limited responsiveness to vibrations and are difficult to mount to structures for commercial application. They also require complex integrated circuits. In contrast, commercially available metallic piezoresistive-based strain sensors are highly functional [10]. In the piezoresistive method, resistance change, $\Delta R/R$, is measured to calculate the resultant strain, $\varepsilon$, from gauge factor (GF) equation, as shown in Equation 4.1 [5].

$$GF = \frac{\Delta R/R}{\varepsilon} \tag{4.1}$$

In Equation 4.1, $\Delta R$ is the difference between the initial resistance of the sample before loading, $R$, and the instantaneously measured resistance of the sample during loading.

Recently, several researchers have explored the use of 3D-printed polymer composites for SHM. For instance, Xiao et al. [12] and Herbert et al. [13] used digital light-based 3D printing and aerosol jet printing techniques to study the electromechanical properties of flexible polymer composites for strain sensing applications. These studies used silver nanowire composites and multi-walled carbon nanotube composites for sensing capabilities. Iizuka et al. [14] studied the electromechanical properties of carbon fiber reinforced thermoplastic composites to support SHM for rigid materials. Saleh et al. [15] studied the applicability of additively manufactured continuous wire PLA composites using two types of wires for SHM. The GF was 1.17 ±0.06 and 1.13 ±0.07

75

for copper and nichrome wire PLA composites, respectively. Continuous wires within FFF composites were not only used for resistance measurement sensing, but also increased the mechanical properties of the composite. However, functional composites of continuous wire with flexible polymer have not been investigated for SHM.

Due to the complex nature and heterogeneous failure modes of fiber-reinforced composites, full characterization of composite failure is required through non-contact strain measurement. Resistance response to stretching can be recorded in one or two directions, depending on the structure of the sensor used [16]. This can be done by measuring resistance corresponding to both axial and transverse strains to understand the mechanical behaviour of the composite. The method used to measure the strain in both directions is called two-dimensional digital image correlation (DIC) [17]. DIC is commonly used to detect surface deformation of composites. It is a powerful tool that offers flexibility in surface measurements for solid mechanics. 2D DIC compares collected digital images of specimen surfaces before and after deformation to obtain full-field displacements and strains [18,19].

In this study, the FFF fabrication technique was selected to fabricate strain sensors because of its simplicity, customizability, and ability to print complex shapes and utilize various polymeric materials (i.e., rigid or flexible). Low-cost continuous wire polymer composite (CWPC) material was used to integrate the wire into the functionalized 3D structure, which enhanced the material's mechanical properties in addition to providing sensing capabilities. This fabrication technique and the CWPC material allows for detection of damage anywhere within the whole part. A detailed comparison between the electromechanical behavior of a rigid PLA-based material and hyperelastic TPU-based material was investigated to understand their performance for SHM applications. Two matrices (PLA and TPU) were used, and the functionality of the CWPC was

examined, based on the GF values. To obtain the full-field strain of the sample under tensile loading, the 2D DIC technique was applied. Rule of mixture (ROM) and hyperelastic analytical models were introduced to compare the experimental mechanical properties with the theoretically calculated values. An analytical model for electromechanical properties was proposed to verify the GF results for both PLA and TPU CWPCs. The flexible sensor with continuous reinforcement presented in this study has not been explored previously; this sensor widens the range of applications in the field of SHM, especially by using the low-cost and straightforward fabrication technique of FFF.

## 4.2. Experimental Methods

### 4.2.1. Materials

Two polymer matrices were used in this study. PLA filament (1.75 mm Transparent PLA, ColorFabb, The Netherlands) and flexible TPU filament (1.75 mm Transparent TPU, Ninjatek, USA). The electrically conductive element was a polyimide-coated copper wire (75 µm Cu wire, Remington Industries, USA) which served as the integrated health monitoring sensor.

### 4.2.2. Sample Fabrication

An open-source 3D printer (Prusa i3 mk2, Prusa Research, Prague, Czech Republic) was modified, and the CWPC samples were fabricated using the method detailed by Ibrahim et al. [20]. CWPC samples were manufactured following ASTM D3039 - 17 with dimensions of 200 mm × 25 mm × 2 mm. A G-code was generated using a custom MATLAB code (MATLAB R2019b, Natick, Massachusetts: The MathWorks Inc.). The G-code was used to define the movements of the axes to print the samples in an axial parallel pattern which was not available in commercial slicing software. Table 4-1 presents the printing parameters used to prepare the samples. The extruder

temperature and bed temperature were selected based on the recommendation of the material manufacturers. The nozzle diameter was selected to accommodate composite printing with wire. Other geometrical parameters were chosen according to the aforementioned ASTM standard. For example, the raster parameters were selected to form the two-dimensional surface area of the sample (single layer) as determined by the nozzle movement in both x and y axes. Then, the nozzle was moved upward in the z-direction by the layer thickness to form the second layer. This process continued until the specified thickness of the sample was achieved. Figure 4-1 shows a 3D-printed sample and its principal axes. Four configurations were printed: pure PLA, Cu wire reinforced PLA (PLA+Cu), pure TPU, and Cu wire reinforced TPU (TPU+Cu).

Table 4-1. Printing parameters of CWPC samples.

| | Material Type | | Unit |
|---|---|---|---|
| | PLA, PLA+Cu | TPU, TPU+Cu | |
| Extruder temperature | 200 | 220 | °C |
| Bed temperature | 50 | 55 | °C |
| Nozzle diameter | 1 | | mm |
| Wire diameter | 0.075 | | mm |
| Raster width | 0.65 | | mm |
| Layer height | 0.5 | | mm |
| Printing angle | 0 | | ° |
| Number of rasters | 38 | | |
| Number of layers | 4 | | |
| Fill density | 100 | | % |
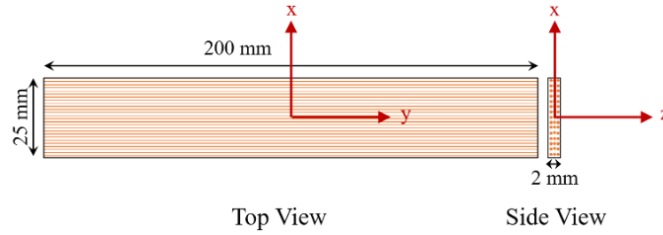
Figure 4-1. 3D-printed sample with principal axes.

Samples were prepared for electrical measurements following the method presented by Saleh et al. [15]. PLA end tabs were printed and used to avoid slippage between the sample and the test frame grips to ensure that the sample fails within the gauge length. End tabs had a rectangular shape with dimensions of 60 mm x 25 mm x 2 mm and a taper angle of 6.7°. The sample with bonded end tabs was prepared as in [15]. Four samples of each CWPC configuration were prepared.

### 4.2.3. Electromechanical Testing

The samples were electromechanically characterized by measuring the electrical resistance of the embedded copper wire under tensile loading. The electrical resistance was recorded using an in-situ digital multimeter (DMM) (Agilent 34401A, Agilent Technologies Inc., Colorado, USA). To eliminate lead wire resistance, the four-probe method was applied. A customized MATLAB script was used to acquire the data at a frequency of 1 Hz. The sample was loaded with a constant crosshead speed of 2 mm/min using a dynamic test frame (Instron ElectroPlus Model E3000, Norwood, USA) equipped with a 3 kN load cell. The load and displacement were acquired using a data acquisition unit (DAQ) (DAQ M Series, NI USB-6210, National Instrument, Texas, USA). The data acquired with the DAQ was synchronized with the DMM using a MATLAB script at the same frequency rate of 1 Hz. Figure 4-2 shows the experimental setup of this study.
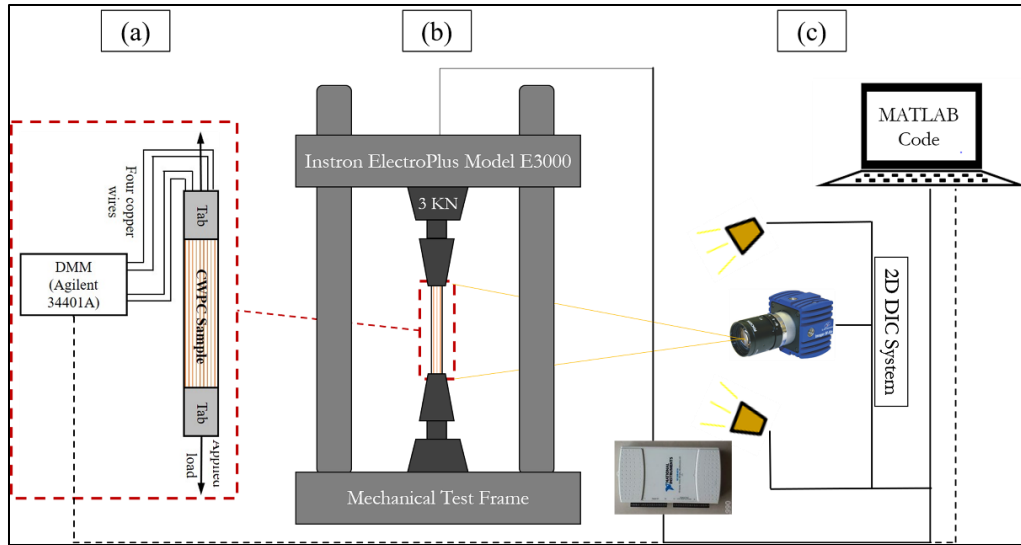
Figure 4-2. Experimental setup of electromechanical testing: (a) test sample with integrated sensor, (b) electrodynamic test frame for quasi-static and dynamic evaluation of the sensor, (c) 2D DIC system for full-field strain measurement.

The sample extension was measured using a 2D DIC system, which was also synchronized with the DAQ and DMM using the same MATLAB script. A 5M Basler camera (acA2440-35um, Basler AG, Ahrensburg, Germany) placed 0.5 m away from the sample was used to acquire the images at a rate of 1 Hz with an area of interest (AOI) on the sample of (60 mm x 70 mm).

Figure 4-3 presents a schematic image of the CWPC sample with two end tabs which prevent slippage and allow for accurate results during the mechanical testing. The image setup included a 50 mm focal length lens (KOWA LM50JCM 2/3" 50MM F2.8, RMA electronics, USA) and two light-emitting diode panels (Neewer 2 Packs LED light, Neewer, Shenzhen, China) illuminated the sample.
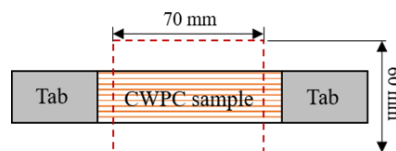


Figure 4-3. AOI on the CWPC sample.

The DIC software package (DaVis version 10.0.3 StrainMaster, LaVision GmbH, Gottingen, Germany) was used to conduct the strain measurements for the acquired images. First, samples were painted black using (2X Ultra Cover, Rust-Oleum Corp, Concord, ON, Canada) and speckled white with a mixture of white paint (5211 Opaque White, Createx Airbrush Colors, Createx Colors, East Granby, CT, USA) and reducer (4012 High-Performance Reducer, Createx Colors, East Granby, CT, USA) to achieve a high contrast speckle pattern for the process of image correlation. An airbrush (H-SET, Paasche Airbrush Company, Chicago, IL, USA) was used to apply the speckling pattern. An example of a speckled sample is shown in Figure 4-4 along with a profile of grayscale count across the width of the sample. Figure 4-4b shows the variation between the peaks and valleys across the width, representing the alternation between black and white colors and indicating good contrast for the image. Second, the images were divided into 49 x 49 pixel subsets size with a 16 pixel step size such that each subset had an average of 5 speckles for image post-processing. Each subset was correlated with another subset in the consecutive image, following the least-squares displacement measurements algorithm to obtain the displacement vector which was used afterwards to calculate the strain. The calculated average value of strain within each field of view (25 mm x 50 mm) was finally plotted against the corresponding tensile stress to obtain the stress–strain curve of each sample. This curve was used to obtain the ultimate tensile strength, *UTS*, and Young's modulus, *E*, of each sample. From 2D DIC images, both axial and transverse strains were calculated to obtain Poisson's ratio (Equation 4.2).

$$v = -\frac{lateral\ strain}{axial\ strain} \qquad (4.2)$$
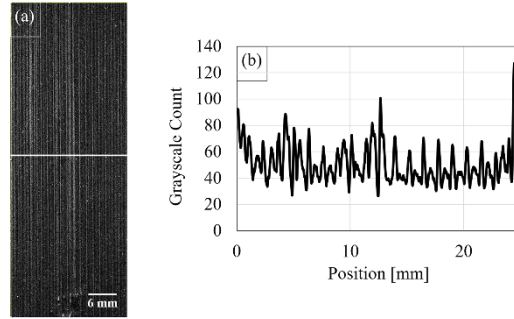
Figure 4-4. a) Example of 3D-printed speckled sample; b) a grayscale contrast profile of the speckled pattern extracted at the middle of the sample (indicated by the horizontal white line in part a).

Figure 4-5 shows the sample at different stages of preparation. As shown in Figure 4-5a, two wires are extended from the end of the 3D-printed sample, representing the two ends of the circuit embedded within the sample. Figure 4-5b and c show the electrical terminals applied using the four-probe method to negate the lead wire resistance. Figure 4-5d presents the final tabbed sample which was painted black and speckled white.
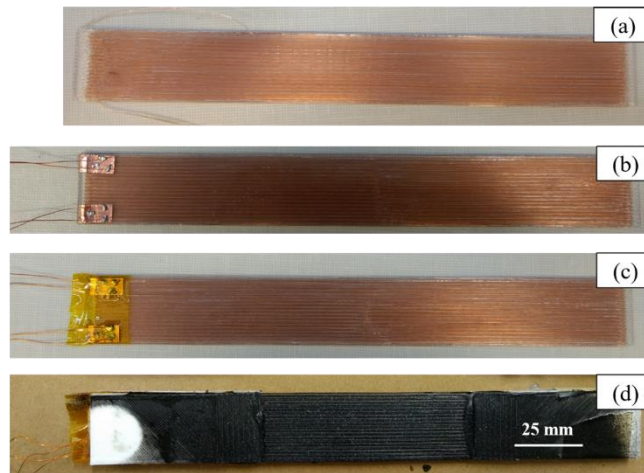


Figure 4-5. Sample preparation stages: a) 3D-printed sample, b) sample with two electrical terminals applied using the four-probe method, c) electrical terminal insulation using Kapton tape, d) painted and speckled sample with end tabs.

The sensitivity of the wire sensors was determined based on the GF calculation, as shown in Equation 4.1. The GF value was based on the fractional change of electrical resistance (Equation 4.3) [21] and the $\varepsilon_{yy}$ strain calculated from the 2D DIC system.

$$Fractional\ change\ of\ electrical\ resistance\ (\Delta R/R) = \frac{R_i - R}{R} \qquad (4.3)$$

where $R_i$ is the measured resistance of the sample during loading and $R$ is the initial resistance of the sample before loading.

### 4.2.4. Microscopic Imaging

The samples were cut to examine the cross section and quantify the wire volume fraction within the printed part using an optical microscope. A transparent resin (Amazing Clear Cast, Alumilite Corp, USA) was used to mount the samples in a mold of 28 mm inner diameter, then cured for 24 hours. A high-speed cut-off saw (Mecatome T260, PRESI, Hungary) was used to section the samples. Then, sample surface preparation was carried out using a polishing machine (StarGrind™ 200-2V, Microstar 2000, Canada) at a rotational speed of 300 rpm. Silicon carbide papers with 180, 280, 400, and 600 grit were used, followed by polishing using a suspension of 1 μm alumina particles. An optical stereomicroscope (LEICA MZ10 F, LEICA, Germany) was used at 50x magnification to quantify the volume fraction of printed polymer composite constituents. Finally, open-source image processing software (ImageJ, National Institutes of Health, Bethesda, Maryland, USA) was used to process captured images and calculate the volume fraction.

## 4.3. Analytical Modelling

To verify the experimental data of mechanical properties and because the two types of materials had different stiffnesses, different analytical models were selected to fit each type. The rule of

mixture (ROM) model assumes rigid (linear elastic material) material with continuous reinforcement; therefore, it was chosen to study the properties of PLA CWPC. Because of its flexibility (non-linear elastic material), analytical models for hyperelastic materials were chosen to study TPU CWPC.

### 4.3.1. Rule of Mixture (ROM) Model

For the continuous wire reinforced PLA composite, the rule of mixture (ROM) was used to predict its mechanical properties [20,22]. Equation 4.4 was used to predict the UTS (4.4-a), Young's modulus (4.4-b), and Poisson's ratio (4.4-c). To calculate the effective properties of the wire reinforced PLA composite, the individual properties and volume fraction of each constituent needed to be identified. Table 4-2 lists the assumed Cu wire properties of UTS, Young's modulus, and Poisson's ratio [20]. PLA UTS, Young's modulus, and Poisson's ratio were experimentally determined (as mentioned in Sec. 4.2.3) for the printed polymer and these experimental values will be listed later in Sec. 4.4.2.

$$\sigma_c = V_w \sigma_w + V_p \sigma_p \qquad \text{(4.4-a)}$$

$$E_c = V_w E_w + V_p E_p \qquad \text{(4.4-b)}$$

$$\nu_c = V_w \nu_w + V_p \nu_p \qquad \text{(4.4-c)}$$

where $\sigma_c$, $\sigma_w$, $\sigma_p$, $E_c$, $E_w$, $E_p$, $\nu_c$, $\nu_w$, and $\nu_p$ are the UTS, Young's modulus, and Poisson's ratio of the composite, wire, and polymer, respectively. $V_w$ and $V_p$ are the volume fractions for both wire and polymer, respectively. $V_w$ and $V_p$ were mathematically calculated following the method mentioned in [15].

Table 4-2. Mechanical properties of Cu wire [20].

| Material | Material Properties | | |
|----------|---------------------|-----|-----------------|
|          | Young's modulus | UTS | Poisson's ratio |
| Cu wire | 110 GPa | 210 MPa | 0.355 |

It is common for 3D-printed parts to include voids because the material is horizontally staked in rasters with an elliptical cross section to form the layer which is then staked vertically above other layers to form the part. Thus, the ROM matrix property was modified to account for them, as supported by several researchers [15,22,23].

### 4.3.2. Hyperelastic Analytical Model

According to the literature [24], three classifications of hyperplastic models can be formulated depending on the development of the model function. The first model is driven based on a mathematical development of energy strain function, the second model is based on conducting experimental data (empirical model), and the third model is based on physical motivation such as polymer chains network physics and statistical methods. Each of these formulations was used in this study to anticipate the hyperelastic mechanical behaviour of TPU CWPC. The Mooney–Rivlin two parameters model represents the model developed using the strain–energy function, the Yeoh model is based on experimental findings, and the Neo-Hookean model utilizes network physics and statistical methods. In these models, the sample is transversely isotropic because its cross-section plane is the plane of isotropy where the properties are the same in all directions because the wire has a circular cross section. The sample was also assumed to be incompressible under uniaxial tensile load such that Equations 4.5 and 4.6 are valid [25].

$$\lambda_1 \lambda_2 \lambda_3 = 1 \tag{4.5}$$

$$\lambda_1 = \lambda, \qquad \lambda_2 = \lambda_3 = \frac{1}{\sqrt{\lambda}} \tag{4.6}$$

where $\lambda$ is the stretch ratio along the principal axes ($\lambda = 1 + strain$).

The formulas to predict the three hyperelastic analytical models are presented in Equations 4.7–4.9 [25]:

Neo-Hookean model: $\sigma_{Hookean} = 2(\lambda^2 - \frac{1}{\lambda})C_1$  (4.7)

Mooney–Rivlin two parameters model: $\sigma_{Mooney} = 2(\lambda^2 - \frac{1}{\lambda})(C_1 + C_2\frac{1}{\lambda})$  (4.8)

Yeoh model: $\sigma_{Yeoh} = 2\left(\lambda^2 - \frac{1}{\lambda}\right)(C_1 + 2C_2\left(\lambda^2 + \frac{2}{\lambda} - 3\right) + 3C_3\left(\lambda^2 + \frac{2}{\lambda} - 3\right)^2)$  (4.9)

where $\sigma_{Hookean}$, $\sigma_{Mooney}$, and $\sigma_{Yeoh}$ are applied stresses in a uniaxial direction, and $C_1$, $C_2$, and $C_3$ are material parameters.

To obtain material parameters of these analytical models, curve fitting of experimental data of the stress–stretch curve was applied through least-square and Levenberg–Marquardt type algorithm methods using Comsol software (Comsol Multiphysics 5.5, Stockholm, Sweden). In this software, the optimization tool of the aforementioned algorithm was used to build the model. For this model, material and stretch parameters were defined and the equation was defined in terms of stress.

Then, the obtained material parameters were used to plot the stress–strain curve for each analytical model. Finally, the obtained stress–strain curve was used to produce the theoretical UTS and Young's modulus for each sample and then these values were compared with the experimental ones.

Equation 4.10 was applied to evaluate the efficiency of the analytical model and to calculate the relative error between the optimal numerical fitting and the experimental data [26];

$$Error = \frac{\sigma(\lambda_i, parameters) - \sigma_{exp_i}}{\max\{0.5|\sigma_{exp_i}\}} \qquad i = 1, ..., m \qquad \text{(4.10)}$$

where $\sigma(\lambda, parameters)$ is the analytical model stress function, $\sigma_{exp}$ is the experimental tensile stress, and m is the number of readings. There is a slight modification in the denominator, as reported by [26], where 0.5 is included to avoid division by a small value of $\sigma_{exp}$ when $\lambda$ approaches 1. Finally, the average error was calculated to assess the difference between the theoretical and experimental results [26].

### 4.3.3. Gauge Factor Model

Theoretical values of gauge factor of PLA and TPU CWPCs were predicted using an analytical model as described by Saleh et al. [15]. In this model, the change in resistance is calculated corresponding to each mechanical strain using Equation 4.11. In this equation, when the structure is subjected to mechanical strain, the corresponding resistance, R, varies due to the geometrical changes of the conductive constituent in the composite in terms of cross-sectional area reduction and elongation.

$$R_i = \frac{\rho L_i}{A_i} \qquad \text{(4.11)}$$

where $L_i$, $A_i$, and $R_i$ are instantaneous values of the wire length, area, and electrical resistance, respectively, corresponding to the applied strain. $\rho$ is the resistivity of the copper wire.

The experimental strain data was plotted against the calculated change in resistance ($\frac{R_i - R}{R}$) and the slope of this curve was used to obtain the theoretical GF value as indicated in Equation 4.1.

Analytical and experimental GF values were compared for statistical significance using a paired sample T-test with an accepted confidence level of 95% (*p < 0.05*).

## 4.4. Results and Discussion

### 4.4.1. Optical Microscopy

Figure 4-6 presents the cross section of PLA and TPU CWPC 3D-printed samples. It can be noted that the wire is uniformly distributed within the samples for both PLA and TPU CWPCs. Voids were found in the samples, and these voids were found mainly around the wire. ImageJ software was used to process the optical microscope images (Figure 4-6a and b) and determine the volume fraction of each constituent of the fabricated composite. The threshold tool was applied to identify voids within the sample and to compute the void volume fraction, $V_v$%, (Figure 4-6c and d); then, similarly, the volume fraction of the wire, $V_w$%, was calculated (Figure 4-6e and f). Table 4-3 summarizes the volume fraction values of each constituent. It can be noticed that the $V_v$% for TPU CWPC is less than that of PLA CWPC, and this may be attributed to the greater flexibility of TPU matrix compared to PLA.
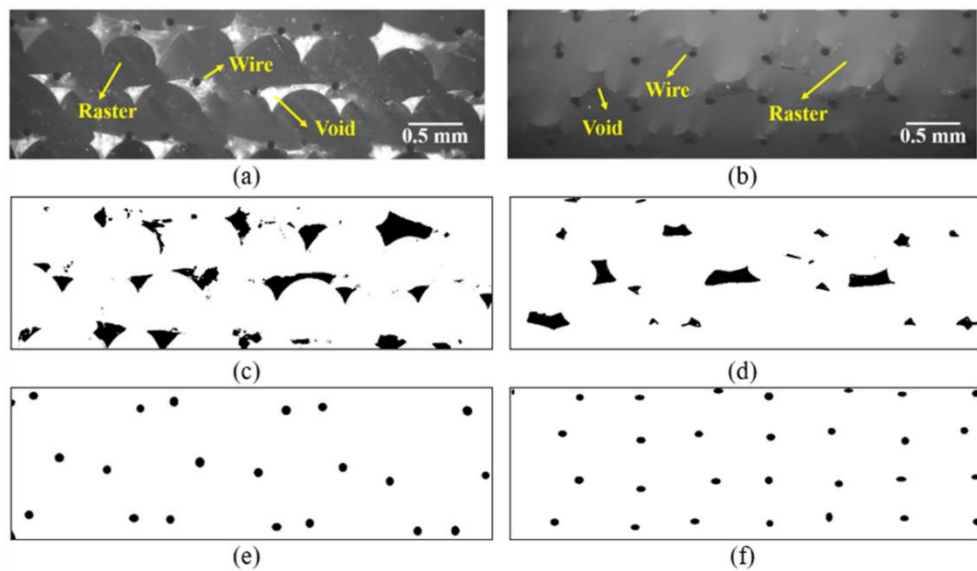


Figure 4-6. Microscopy cross section of a) PLA+Cu, b) TPU+Cu. Processed images to calculate $V_v$% of c) PLA+Cu, d) TPU+Cu. Processed images to calculate $V_w$% of e) PLA+Cu, f) TPU+Cu.

Table 4-3. Volume fraction of PLA and TPU CWPC constituent.

| | Cu wire reinforced PLA composite | Cu wire reinforced TPU composite |
|---|---|---|
| Matrix ($V_p$%) | 91.9 (±0.76) | 94.05 (±0.83) |
| Wire ($V_w$%) | 1.8 (±0.006) | 1.7 (±0.007) |
| Void ($V_v$%) | 6.3 (±0.017) | 4.25 (±0.014) |

### 4.4.2. Mechanical Properties

Full-field strain distributions were measured using a 2D DIC system. Strain in both the axial and transverse directions are presented in Figure 4-7 and Figure 4-8 for both PLA CWPC and TPU CWPC. Higher flexibility of TPU compared to PLA can be clearly observed in these figures (Figure 4-7 and Figure 4-8). Figure 4-7 shows the axial full-field strain distribution at different stress levels. It can be noted that the TPU CWPC shows higher positive axial deformation from the start of the test until just before the failure of the sample compared with PLA CWPC under tensile loading. For the transverse direction, as shown in Figure 4-8, it can also be seen that the TPU CWPC can sustain more deformation compared with PLA CWPC throughout the tensile test, following the same trend of the deformation in the axial direction.

As mentioned in Sec. 4.2.3, 2D DIC results were used to calculate the average strain for each image, and then the strain was plotted against the corresponding tensile stress to obtain the stress–strain curve of each type of material. Figure 4-9 shows the stress–strain curves for PLA and TPU CWPCs. This figure verifies the DIC results because it shows that TPU CWPC samples sustain failure strain six times larger than that of PLA CWPC samples. At the same time, PLA CWPC has higher strength (52.2 MPa) compared with TPU CWPC (5.583 MPa).
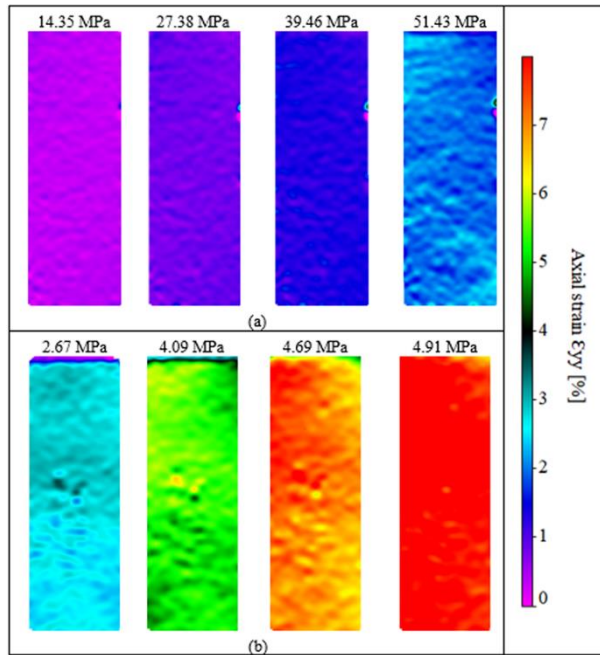
Figure 4-7. The progression of axial strain obtained using 2D DIC strain measurement just

before failure of a) PLA CWPC, b) TPU CWPC.
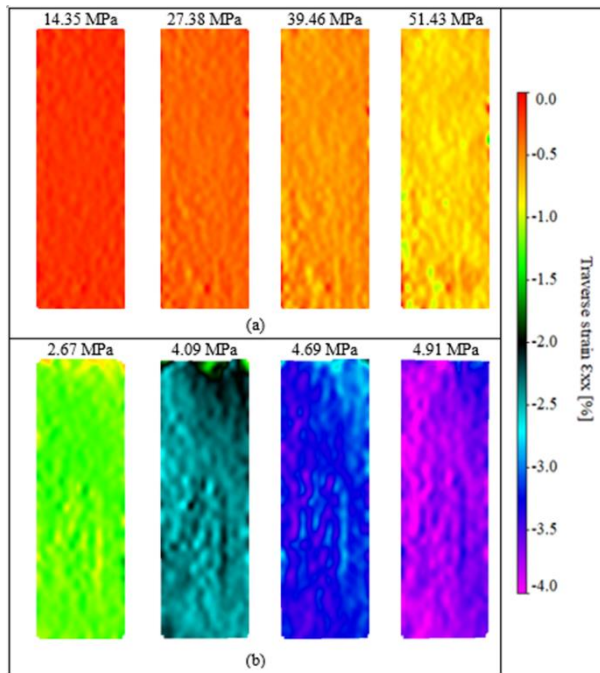


Figure 4-8. The transverse strain progression obtained using 2D DIC strain measurement just

before failure of a) PLA CWPC, b) TPU CWPC.
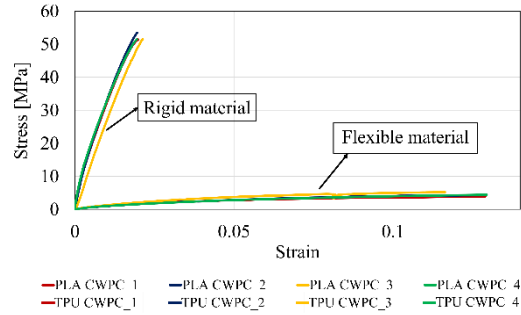
Figure 4-9. Example of stress–strain curve for PLA and TPU CWPCs

2D DIC results were compared for both PLA and TPU CWPCs at the same stress level to demonstrate the difference of the full-field strain between each material type under tensile loading. Figure 4-10 shows the full-field strain distribution at a stress level of 2 MPa. It can be seen that both axial and transverse strains are higher in TPU CWPC than PLA CWPC. PLA CWPC experienced almost no strain at this small stress level for both the axial and transverse directions, while TPU CWPC strained by about 2% and -1% for the axial and transverse directions, respectively.
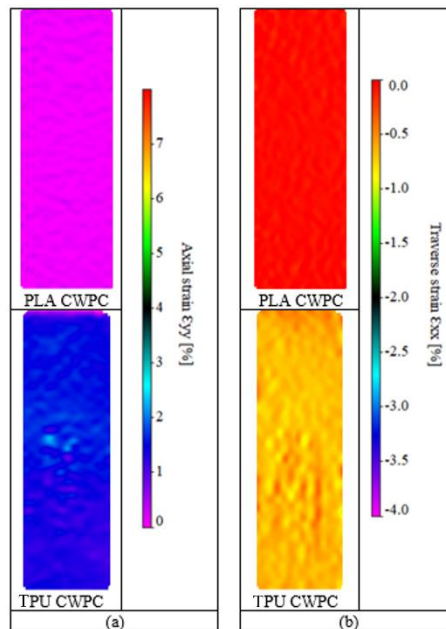


Figure 4-10. Full-field strain distribution at a stress level of 2 MPa for PLA and TPU CWPCs: a) axial strain $\varepsilon_{yy}$, b) transverse strain $\varepsilon_{xx}$.

Figure 4-11 compares the experimentally obtained mechanical properties (ultimate tensile strength, *UTS*, Young's modulus, *E*, and Poisson's ratio, *v*) of PLA, PLA+Cu, TPU, and TPU+Cu. It can be seen that both UTS and Young's modulus of PLA-based materials are larger than those of TPU-based materials. However, Poisson's ratio, v, is larger for TPU-based materials because of the higher flexibility of TPU compared with PLA. Young's modulus was improved by 80.3% and 210.5% for PLA composite and TPU composite, respectively, compared with pure PLA and TPU. The statistical analysis which compared the pure materials with the composite ones shows that UTS was significantly improved only for the case of TPU-based materials (by 31.86%), and this may be attributed to the larger difference in UTS between TPU and Cu compared with PLA-based materials. Young's modulus was significantly improved for both PLA CWPC and TPU CWPC compared with PLA and TPU, respectively. Poisson's ratio was not significantly changed for composite materials compared with pure ones. These statistical results were obtained by applying an independent sample t-test with a confidence level of 95% and are presented in Table 4-4.
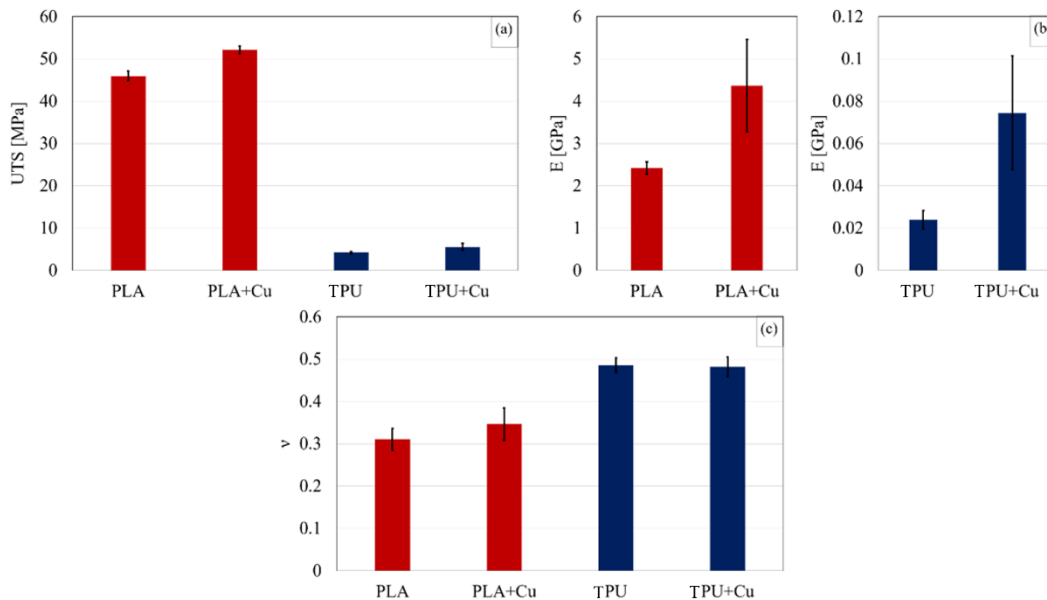


Figure 4-11. PLA, PLa+Cu, TPU, and TPU+Cu mechanical properties: a) ultimate tensile strength, *UTS*, b) Young's modulus, *E*, and c) Poisson's ratio, *v*.

Table 4-4. Independent sample t-test to compare mechanical properties of PLA with PLA+Cu
and TPU with TPU+Cu (S: statistically significant, NS: statistically not significant).

|  |  | P-value | Significance |
|---|---|---|---|
| Ultimate Tensile Strength, *UTS* | PLA & PLA+Cu | 0.889 | NS |
|  | TPU & TPU+Cu | 0.019 | S |
| Young's Modulus, *E* | PLA & PLA+Cu | 0.044 | S |
|  | TPU & TPU+Cu | 0.015 | S |
| Poisson's Ratio, *v* | PLA & PLA+Cu | 0.128 | NS |
|  | TPU & TPU+Cu | 0.775 | NS |

### 4.4.3. Mechanical Model Results

Analytical models for mechanical properties of rigid and hyperelastic materials were applied as
indicated in Sec. 4.3.1 and 4.3.2. Figure 4-12 presents an example of stress–strain curve of the
TPU CWPC sample, comparing the experimental data and the three different applied hyperelastic
analytical models. It can be noted that the Neo-Hookean analytical model has the largest error
(calculated using Equation 4.10) compared with the experimental results, as confirmed by the error
bar chart shown in Figure 4-13. In this figure, both Mooney–Rivlin two parameters model and the
Yeoh analytical model have a small error of $0.066 \pm 0.006$ (6.6% $\pm 0.6\%$) and $0.095 \pm 0.027$ (9.5%
$\pm 2.7\%$), respectively, with respect to the experimental data; because Mooney-Rivlin is easier to
implement than the Yeoh analytical model, it was chosen for further analysis.
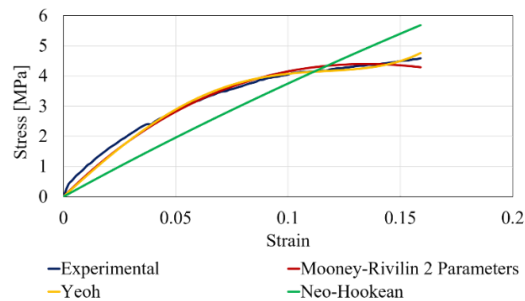


Figure 4-12. Example of experimental and hyperelastic analytical models for TPU CWPC.
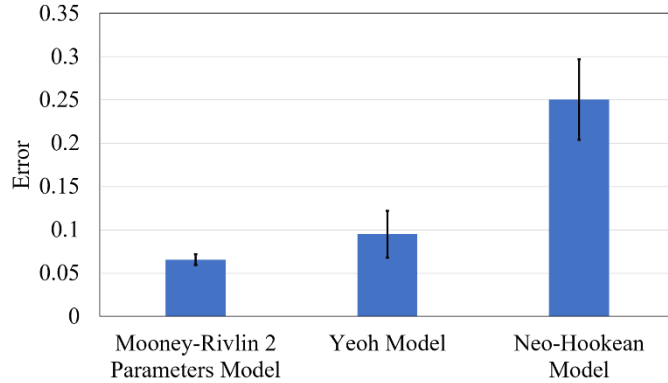
Figure 4-13. Average error between hyperelastic analytical models and experimental data for

TPU CWPCs.

The difference between experimental and theoretical values may be attributed to a lack of consideration of the analytical models of fiber-matrix interaction. For PLA CWPC, ROM was applied, as mentioned in Sec. 4.3.1, using $V_w$ as 1.448% and $V_p$ as 98.552%. Figure 4-14 shows the experimental values of UTS, Young's modulus, and Poisson's ratio versus the analytical model values of the same properties for PLA and TPU CWPCs. There is a slight difference between the experimental and the analytical model data, which may be attributed to the simple assumption of the model which does not take into consideration the complexity of the fabrication process and damage mechanism as reported by [27].

To confirm the credibility of these models, a paired sample t-test with a confidence level of 95% was applied, and the results for both the ROM model and Mooney–Rivlin model versus the experimental data are presented in Table 4-5. The statistical analysis showed a good agreement between the experimental and analytical model data because there was no statistical significance difference between them according to the p-value.
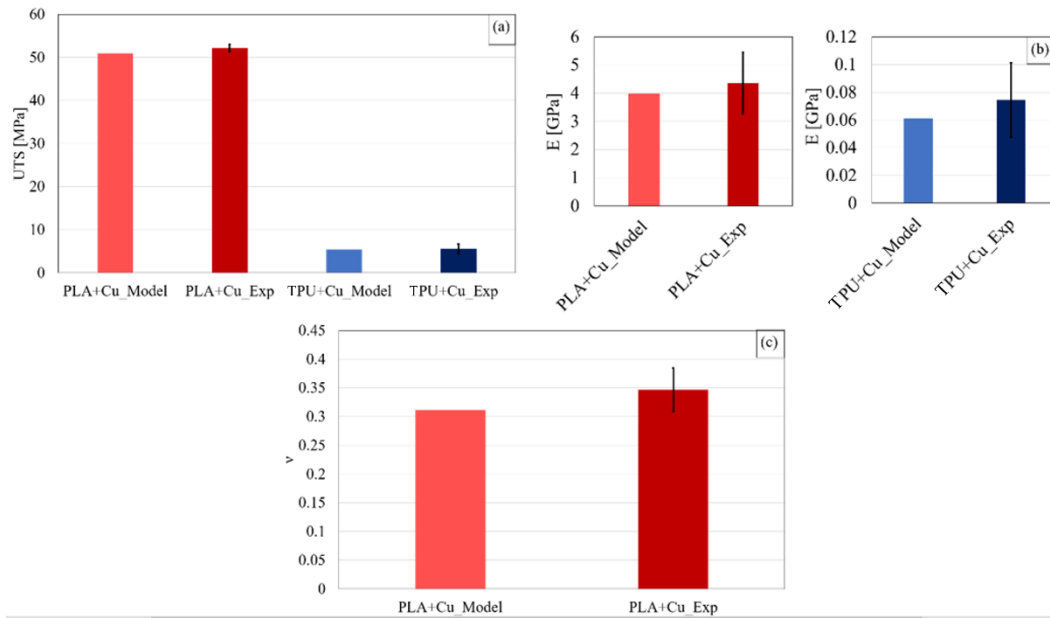
Figure 4-14. Experimental and analytical results of mechanical properties of PLA and TPU CWPCs: a) UTS, b) Young's modulus, and c) Poisson's ratio.

Table 4-5. Paired sample t-test of theoretical and experimental mechanical properties (NS: statistically not significant).

| | | P-value | Significance |
|---|---|---|---|
| Ultimate Tensile Strength, *UTS*, (Model vs. Exp) | PLA+Cu | 0.054 | NS |
| | TPU+Cu | 0.052 | NS |
| Young's Modulus, *E*, (Model vs. Exp) | PLA+Cu | 0.527 | NS |
| | TPU+Cu | 0.09 | NS |
| Poission's Ratio, *v*, (Model vs. Exp) | PLA+Cu | 0.158 | NS |
| | TPU+Cu | N/A | N/A |

### 4.4.4. Electromechanical Properties

Figure 4-15 shows an example of the relative change of electrical resistance under tensile strain for both PLA and TPU CWPCs. The direct linear relationship between the change in resistance and strain proves the suitability of these materials to be used as strain sensors. This agrees with

previously obtained results [15]. The resistance was changed from around 109 Ω in an unloaded

sample to around 112 Ω and 123 Ω just before the cut of the Cu wire for PLA CWPC and TPU

CWPC, respectively. The sudden increase in the value of electrical resistance change indicates a

failure of the wire and loss of conductivity. Therefore, this sensor can be used to predict the

deformation and to indicate the failure mechanism. To obtain the GF, the slope of the first linear

part of the graphs in Figure 4-15 was calculated. The sensitivity of composites using Cu wire in

terms of GF were found to be about 1.36 ±0.14 and 1.29 ±0.07 for PLA and TPU CWPCs,

respectively, as shown in Figure 4-16. An independent sample t-test ($p = 0.05$) was performed to

compare the GF of PLA and TPU CWPC samples, and no statistical was detected (Table 4-6).

This indicates the sensor depends on the wire only, regardless of the matrix used. However, the

TPU CWPCs sustained more strain before breakage of the wire compared with PLA CWPCs, as

depicted by stress–strain curves for PLA+Cu and TPU+Cu samples (Figure 4-9). The higher strain

before the failure of the TPU CWPCs was due to their lower stiffness, as shown in Figure 4-11b.

Therefore, different matrices can be used for different applications, such as rigid sports equipment

and flexible wearable sensors.
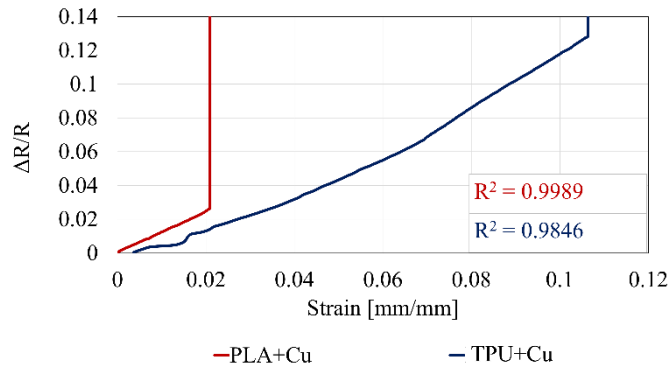


Figure 4-15. Plot of (*ΔR/R-strain*) curve
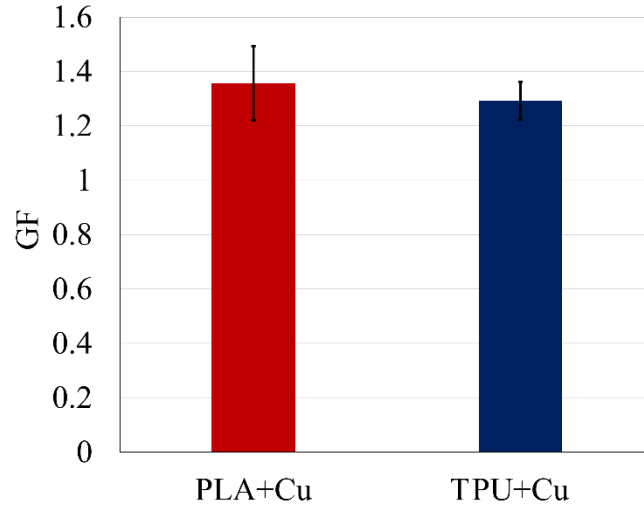
Figure 4-16. GF of PLA and TPU CWPCs.

Table 4-6. Independent sample t-test for GF (NS: statistically not significant).

|  |  | P-value | Significance |
|---|---|---|---|
| GF | PLA+Cu & TPU+Cu | 0.456 | NS |

The sensitivity of both composites was compared with the analytical model, as explained in Sec. 4.3.3 (Figure 4-17). As shown in Figure 4-17, there is a small standard deviation for the theoretical GF bars because the electrical resistance was calculated based on the change of experimental tensile extension, as indicated by Equations 4.3 and 4.11. A paired sample t-test with a confidence level of 95% was applied to statistically analyze the significance between the theoretical and experimental GF of PLA and TPU CWPCs. Table 4-7 supports the use this analytical model to be credibly used to predict the GF because there is no significant difference between the theoretical and experimental data.
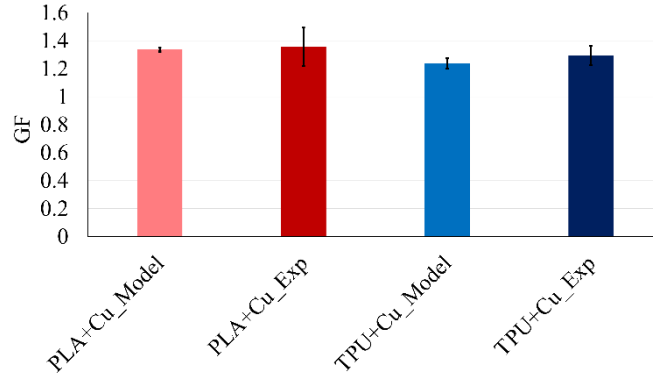
Figure 4-17. Comparison of experimental and analytical models GF for PLA and TPU CWPCs.

Table 4-7. Paired sample t-test of theoretical and experimental GF (NS: statistically not significant).

|  |  | P-value | Significance |
|---|---|---|---|
| GF (Model vs. Exp) | PLA+Cu | 0.772 | NS |
|  | TPU+Cu | 0.342 | NS |

## 4.5. Summary and Conclusions

Two types of polymer matrix composites of rigid and flexible matrices with integrated continuous copper wire were successfully compared in terms of their electromechanical properties for use in structural health monitoring applications. This verifies the capability of 3D printing to fabricate sensors with tunable properties.

A direct relationship between the strain and the change in resistance for PLA and TPU CWPCs indicates the applicability of these 3D-printed structures for use as strain sensors. The electromechanical properties of both composites showed dependency of the strain sensor on the integrated wire, regardless of the type of matrix used because the GFs of 1.36 ±0.14 and 1.29 ±0.07 for both PLA CWPC and TPU CWPC, respectively, are statistically insignificant. Therefore, different matrices can be used to fit different applications, encompassing a wider range of strains.

An analytical model, based on obtaining the GF from the electrical resistance equation, showed agreement with the experimental measured GF for both PLA and TPU CWPCs.

DIC images of both axial and transverse strains showed higher flexibility of TPU CWPC compared with PLA CWPC. The stress–strain curve for both types of composites (PLA and TPU CWPCs) showed higher flexibility of TPU than PLA: the TPU CWPC strain was around six times higher than the PLA CWPC. Ultimate tensile strength, *UTS*, and Young's modulus, *E*, were improved significantly for composite materials compared with pure ones, while Poisson's ratio, *v*, was not significantly changed.

The ROM and Mooney–Rivlin analytical models showed statistical agreement with experimental results for the mechanical properties of PLA and TPU CWPCs, respectively.

Flexible materials showed less void content compared with rigid materials for the 3D-printed samples. Voids were found to be 4.25 ($\pm 0.014$) % for TPU CWPC and 6.3 ($\pm 0.017$) % for PLA CWPC.

## 4.6. References

[1]     C. Tuloup, W. Harizi, Z. Aboura, Y. Meyer, K. Khellil, R. Lachat, On the manufacturing, integration, and wiring techniques of in situ piezoelectric devices for the manufacturing and structural health monitoring of polymer–matrix composites: A literature review, J. Intell. Mater. Syst. Struct. 30 (2019) 2351–2381. https://doi.org/10.1177/1045389X19861782.

[2]     Y. Yang, G. Chiesura, B. Plovie, T. Vervust, G. Luyckx, J. Degrieck, T. Sekitani, J. Vanfleteren, Design and Integration of Flexible Sensor Matrix for in Situ Monitoring of Polymer Composites, ACS Sensors. 3 (2018) 1698–1705.

https://doi.org/10.1021/acssensors.8b00425.

[3]     J.B. Park, T. Okabe, N. Takeda, W.A. Curtin, Electromechanical modeling of unidirectional CFRP composites under tensile loading condition, Compos. - Part A Appl. Sci. Manuf. 33 (2002) 267–275. https://doi.org/10.1016/S1359-835X(01)00097-5.

[4]     R. Balaji, M. Sasikumar, Graphene based strain and damage prediction system for polymer composites, Compos. Part A Appl. Sci. Manuf. 103 (2017) 48–59. https://doi.org/10.1016/j.compositesa.2017.09.006.

[5]     R. Balaji, M. Sasikumar, Development of strain and damage monitoring system for polymer composites with embedded nickel alloys, Meas. J. Int. Meas. Confed. 111 (2017) 307–315. https://doi.org/10.1016/j.measurement.2017.07.036.

[6]     J.S. Sefadi, A.S. Luyt, Morphology and properties of EVA / empty fruit bunch composites, J. Thermoplast. Compos. Mater. 25 (2012), pp.895-914. https://doi.org/10.1177/0892705711421806.

[7]     R.D. Goodridge, M.L. Shofner, R.J.M. Hague, M. Mcclelland, M.R. Schlea, R.B. Johnson, C.J. Tuck, Processing of a Polyamide-12 / carbon nano fi bre composite by laser sintering, Polym. Test. 30 (2011) 94–100. https://doi.org/10.1016/j.polymertesting.2010.10.011.

[8]     N. Kumar, P.K. Jain, P. Tandon, P.M. Pandey, Additive manufacturing of flexible electrically conductive polymer composites via CNC-assisted fused layer modeling process, J. Brazilian Soc. Mech. Sci. Eng. 40 (2018). https://doi.org/10.1007/s40430-018-1116-6.

[9]     M.C. Bertolini, S. Dul, G.M.O. Barra, A. Pegoretti, Poly(vinylidene fluoride)/thermoplastic polyurethane flexible and 3D printable conductive composites, J. Appl. Polym. Sci. (2020)

1–15. https://doi.org/10.1002/app.50305.

[10]   V. Sankar, V. Sankar, A. Nambi, V.N. Bhat, D. Sethy, K. Balasubramaniam, S. Das, M. Guha, R. Sundara, Waterproof Flexible Polymer-Functionalized Graphene-Based Piezoresistive Strain Sensor for Structural Health Monitoring and Wearable Devices, ACS Omega. 5 (2020) 12682–12691. https://doi.org/10.1021/acsomega.9b04205.

[11]   Y. Qureshi, M. Tarfaoui, K.K. Lafdi, K. Lafdi, Development of microscale flexible nylon/Ag strain sensor wire for real-time monitoring and damage detection in composite structures subjected to three-point bend test, Compos. Sci. Technol. 181 (2019) 107693. https://doi.org/10.1016/j.compscitech.2019.107693.

[12]   T. Xiao, C. Qian, R. Yin, K. Wang, Y. Gao, F. Xuan, 3D Printing of Flexible Strain Sensor Array Based on UV-Curable Multiwalled Carbon Nanotube/Elastomer Composite, Adv. Mater. Technol. 6 (2020). https://doi.org/10.1002/admt.202000745.

[13]   R. Herbert, H. Lim, W. Yeo, Printed, Soft, Nanostructured Strain Sensors for Monitoring of Structural Health and Human Physiology, (2020). https://doi.org/10.1021/acsami.0c04857.

[14]   K. Iizuka, A. Todoroki, T. Takahashi, M. Ueda, Reverse piezo-resistivity of 3D printed continuous carbon fiber / PA6 composites in a low stress range, Adv. Compos. Mater. 00 (2020) 1–16. https://doi.org/10.1080/09243046.2020.1848314.

[15]   M.A. Saleh, R. Kempers, G.W. Melenka, 3D printed continuous wire polymer composites strain sensors for structural health monitoring, Smart Mater. Struct. 28 (2019) 105041. https://doi.org/10.1088/1361-665x/aafdef.

[16]  H. Nakamoto, H. Ootaka, M. Tada, I. Hirata, F. Kobayashi, F. Kojima, Stretchable Strain Sensor with Anisotropy and Application for Joint Angle Measurement, IEEE Sens. J. 16 (2016) 3572–3579. https://doi.org/10.1109/JSEN.2016.2535489.

[17]  B.P. Justusson, D.M. Spagnuolo, J.H. Yu, Assessing the Applicability of Digital Image Correlation ( DIC ) Technique in Tensile Testing of Fabric Composites, (2013) 1–24. http://www.dtic.mil/docs/citations/ADA571047%0Apapers3://publication/doi/10.21236/ADA571047.

[18]  B. Pan, K. Qian, H. Xie, A. Asundi, Two-dimensional digital image correlation for in-plane displacement and strain measurement: A review, Meas. Sci. Technol. 20 (2009). https://doi.org/10.1088/0957-0233/20/6/062001.

[19]  R.H. Pritchard, P. Lava, D. Debruyne, E.M. Terentjev, Highlighting the research collaboration between, Soft Matter. 9 (2013).

[20]  Y. Ibrahim, G.W. Melenka, R. Kempers, Fabrication and tensile testing of 3D printed continuous wire polymer composites, Rapid Prototyp. J. 24 (2018) 1131–1141. https://doi.org/10.1108/RPJ-11-2017-0222.

[21]  R. Matsuzaki, M. Ueda, M. Namiki, T.K. Jeong, H. Asahara, K. Horiguchi, T. Nakamura, A. Todoroki, Y. Hirano, Three-dimensional printing of continuous-fiber composites by in-nozzle impregnation, Sci. Rep. 6 (2016) 1–7. https://doi.org/10.1038/srep23058.

[22]  G.W. Melenka, B.K.O. Cheung, J.S. Schofield, M.R. Dawson, J.P. Carey, Evaluation and prediction of the tensile properties of continuous fiber-reinforced 3D printed structures, Compos. Struct. 153 (2016) 866–875. https://doi.org/10.1016/j.compstruct.2016.07.018.

[23] J.F. Rodriguezjames, P.T.E. Renaud, J.F. Rodriguez, J.P. Thomas, J.E. Renaud, Characterization of the mesostructure of fused-deposition acrylonitrile-butadiene-styrene materials. Rapid Prototyp. J. (2000). https://doi.org/10.1108/13552540010337056.

[24] Gilles Marckmann, Erwan Verron, Comparison of Hyperelastic Models for Rubber-Like Materials. Rubber Chemistry and Technology, American Chemical Society, 2006, 79, pp.835-858. 10.5254/1.3547969. hal-01004686v1.

[25] A. Chanda, S. Chatterjee, V. Gupta, Soft composite based hyperelastic model for anisotropic tissue characterization, J. Compos. Mater. 54 (2020) 4525–4534. https://doi.org/10.1177/0021998320935560.

[26] R. W. Ogden, G. Saccomandi, I. Sgura, Fitting hyperelastic models to experimental data, Comput. Mech. J. 34 (2004) 484-502. https://doi.org/10.1007/s00466-004-0593-y

[27] G. Sun, S. Tong, D. Chen, Z. Gong, Q. Li, Mechanical properties of hybrid composites reinforced by carbon and basalt fibers, Int. J. Mech. Sci. 148 (2018) 636–651. https://doi.org/10.1016/j.ijmecsci.2018.08.007.

# Chapter 5      Fatigue Behaviour and Electromechanical Properties of Additively Manufactured Continuous Wire Polymer Composites for Structural Health Monitoring

The fatigue behaviour of continuous wire polymer composite (CWPC) fabricated by fused filament fabrication (FFF) was investigated. Four compositions were examined: polylactic acid (PLA), PLA with copper wire (Cu), thermoplastic polyurethane (TPU), and TPU with Cu wire. Residual properties were measured after different sets of number of cycles ($10^2$, $10^4$, $10^5$). Residual strengths were 89.7% and 70.5% of the ultimate tensile strength of the original material after $10^5$ cycles for PLA CWPC and TPU CWPC, respectively. A one-way analysis of variance (ANOVA) statistical tests showed insignificant changes in the residual strengths of PLA-based materials after an increasing number of cycles and significant changes for the TPU-based materials. CWPC electromechanical properties under fatigue test demonstrated reverse piezoresistance behavior. A strain-controlled fatigue life analytical model was compared to the experimental results showing good agreement. This study demonstrates the applicability of FFF technique to print sensors with continuous integrated wire with tunable properties.

## 5.1. Introduction

Additive manufacturing (AM) has become increasingly popular because it affords new design opportunities not offered by many conventional fabrication approaches. Improvements in this technology and design knowledge have led to the rapid fabrication of high-quality and low-cost parts; therefore, AM is making a growing contribution to research and industry communities. Many polymer materials with varying properties have been introduced based on consumer use and technological requirements [1–4]. For instance, both rigid materials (e.g., acrylonitrile butadiene styrene (ABS) and polylactic acid (PLA)) and flexible materials (e.g., nylon and thermoplastic polyurethane (TPU)) have been used successfully in AM processes [3,5,6]. TPU combines excellent wear resistance and tear resistance with high flexibility and impact strength [7].

Fused filament fabrication (FFF) has become the most popular of the AM processes due to its inexpensive hardware and software; it is considered an open-source technology. FFF can be found in businesses, schools, hospitals, and in a wide range of other applications such as the functional testing of parts and design verification and prototyping [1,8]. The properties of FFF-fabricated parts can differ from those manufactured by other conventional methods such as injection molding, vacuum casting, filament winding, pultrusion, and hand layup [9]. Although for many applications FFF parts have an excellent strength-to-weight ratio, several studies [10–13] have reported that FFF parts are inhomogeneous. Therefore, for the same material, the tensile strength of FFF parts is less than that of parts manufactured by injection molding or other processes [14].

Polymer composites can also be used in FFF [15]. Most composite FFF studies have focused on introducing short fibers to the polymer; for example, Carneiro et al. [16] successfully developed glass fiber–reinforced polypropylene composite with improved mechanical properties, and

Shofner et al. [17] compounded single-wall carbon nanotubes with ABS. These studies showed an improvement in tensile strength. Adding fillers with specific properties can improve the composite material's mechanical, thermal, electrical, optical, and biomedical properties and enhance the FFF part's performance [7]. However, a mix of short fiber with polymer filament can only offer a slight increase in the strength and stiffness of the material [8]. FFF technology can also deposit continuous fiber reinforcement along with the polymer filament during the manufacturing process to expand the mechanical properties of the printed part [8]. Brooks et al. [18] found that adding continuous reinforcement to the polymer during the FFF process dramatically improves the part's mechanical properties, regardless of its build orientation. Melenka et al. [6] found that continuous Kevlar-reinforced nylon composite significantly enhanced mechanical properties over conventional FFF parts, and Ibrahim et al. [19,20] developed continuous wire polymer composite materials fabricated by FFF with improved mechanical [20,21] and thermal [22,23] properties. This composite fabrication approach has since been used to fabricate sensors [24,25].

Recently, the fatigue behaviour of AM polymers has gained more attention due to their increased use in the biomedical, automotive, and aerospace industries. In many applications, parts are subjected to repetitive loading and fatigue damage [1]. The fatigue behaviour of composites is more complex than that of homogeneous materials. For homogeneous materials, a crack is initiated and propagated, leading to a fracture. However, the fatigue behavior of composites depends on the fiber modulus and matrix ductility; therefore, fatigue damage is unpredictable because it may be caused by different damage mechanisms and their interactions [3,26,27]. In composites, a crack may be initiated at multiple sites with nonvisible damage. Then, with the progress of cyclic loading, the crack propagates by crack bridging or by reinforcement and matrix debonding, leading to the final failure of the part [26,27]. Santos et al. and Brandl et al. [28,29] reported that the fatigue

life of an AM part is significantly lower than that of parts processed by other manufacturing methods. The parameters affecting the fatigue life of AM parts include the weak bond between layers because of the layer-by-layer deposition mechanism and the existence of voids [28,29]. For these reasons, the characterization and understanding of the fatigue behaviour of AM polymer composites is crucial for the design of functional and reliable parts.

To avoid the heating of the materials under cyclic loading, it is recommended that the fatigue test be performed at a low frequency [30]. Higher frequency rates can cause an increase in the sample temperature and, therefore, ductility and localized deformation could increase, which may lead to a shorter fatigue life [1]. Vanaei et al. [9] observed an increase in temperature in 3D-printed PLA when conducting a fatigue test at 80 Hz. As reported by several researchers [1,3,30–33], fatigue tests of polymer composites should be conducted at 5 Hz or less to avoid an increase of sample temperature under cyclic loading.

Most polymer composites do not exhibit the same endurance limit as homogeneous materials. Therefore, residual properties such as residual stiffness and strength are used to quantify fatigue damage accumulation within a part. The fatigue life of polymer composites is determined by the number of cycles required to cause a predetermined decrease in a certain property [9,26].

Fatigue tests can be implemented under deformation (strain)-controlled mode or load (stress)-controlled mode. For rubber and polymers, the former is usually applied [34]. The applied local deformation values are not monitored accurately during the fatigue test using conventional direct methods. For example, extensometers and strain gauges could have difficulties such as having a shorter fatigue life than the tested material. For relatively flexible polymers, the extensometer knives could cause local damage, leading to an inaccurate fatigue life of the specimen. Therefore, non-contact deformation measurement is highly recommended to study

107

polymer fatigue behaviour [34]. Accordingly, a digital image correlation (DIC) technique can be used to measure the applied deformation in situ on the structure during cyclic loading [32]. This method can also detect damage evolution by providing strain maps of the part surface during the fatigue test. A change in these strain maps during the test indicates a change of mechanical properties because of the microscopic damage accumulation [32].

In real-life applications, monitoring the mechanical performance of the composite structure is desirable to detect any changes in the service conditions and prevent catastrophic failure. Sensors such as piezoelectric sensors or optical fibers should be placed on specific locations of the part to monitor the composite structure. However, the placement of sensors can have drawbacks, such as limited sensing volume because the sensor only senses its immediate vicinity; it would be impractical to cover the whole structure in this way. Another drawback of adding sensors is their poor durability due to the tendency of sensors to detach from the structure [35]. Self-monitoring capabilities have been introduced (the ability of the structure itself to act as a sensor) to overcome these limitations. Under cyclic fatigue/dynamic load, strain may change reversibly; therefore, dynamic strain monitoring needs a measurand with the ability to change reversibly with reversible strain [35]. The electrical resistance change method is one technique that can be reversibly changed with loading and unloading during a cyclic test. Therefore, it can be used to detect strain in conductive polymer composites without additional sensors [15].

In this study, a strain-controlled fatigue test was conducted to study the fatigue life behaviour of a 3D-printed continuous wire polymer composite (CWPC) of rigid (PLA-based) and flexile (TPU-based) materials. PLA and TPU were selected for this study as they are some of the most common filaments used for the FFF technique representing rigid and flexible based materials, respectively. The damage evolution was investigated by measuring the residual strength of the material after a

specific number of cycles ($10^2$, $10^4$, $10^5$ cycles) under dynamic loading. After each set of cycles, the residual strengths were statistically compared to check the significance of the damage to the part. During the fatigue test, the electromechanical properties of the CWPC were investigated by correlating the change in wire resistance with the strain. The continuous wire integrated in the part had sensing capabilities, but it also enhanced the mechanical properties of the composite. A fatigue test was conducted at a low frequency of 5 Hz to avoid hysteretic self-heating. A strain-life analytical model was applied for comparison with experimental results obtained from the electromechanical test. A 2D DIC technique was used to accurately measure the strain applied on the sample and acquire strain maps for different sets of cycles in order to study the evolution of damage. Strain maps of both rigid and flexible materials were compared. Damage accumulation was investigated for samples subjected to a total of $10^5$ cycles.

The electromechanical properties of CWPC components have been previously investigated under static loading, however, their behaviour under dynamic loading has not been previously explored in the literature. Thus, studying the fatigue behaviour and electromechanical properties of CWPC under cyclic loading are crucial to widening the range of applications of CWPC components for structural health monitoring as strain sensor.

## 5.2.  Experimental Methods

In this section, the characterization of fatigue properties and electromechanical properties of 3D-printed CWPCs under cyclic fatigue load, using the 2D DIC technique to accurately measure the applied strain, is explained. The general experimental setup of this study is represented in Figure 5-1. In this figure, Part (a) represents the electromechanical testing setup under a cyclic fatigue test using a four-probe method to measure the electrical resistance of the Cu wire (detailed explanation

in Sec. 5.2.5). Part (b) shows where the sample is affixed to the mechanical test frame and subjected to cyclic loading (detailed explanation in Sec. 5.2.3). Sample surface images were captured using the 2D DIC system, as shown in Part (c) of Figure 5-1 (detailed explanation in Sec. 5.2.6). Finally, the fatigue testing and electrical resistance readings were synchronized, as shown in Part (d).
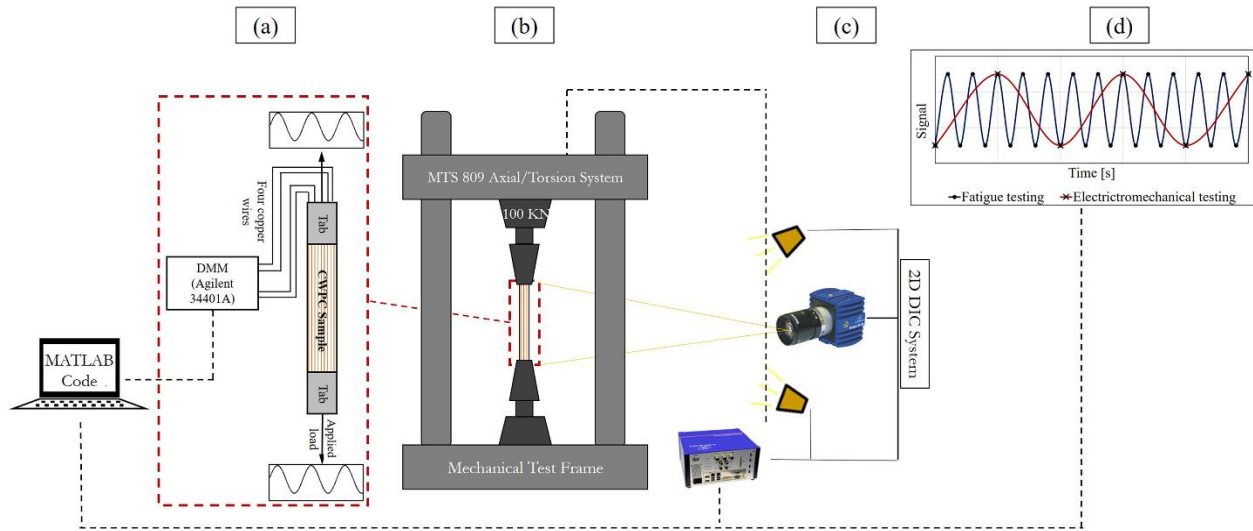


Figure 5-1. Experimental setup of electromechanical fatigue testing: (a) CWPC sample with integrated Cu wire sensor, (b) mechanical test frame for dynamic evaluation of the sensor, (c) 2D DIC system for full-field strain measurement, and (d) synchronization rate.

### 5.2.1. Materials

Flexible TPU filament (1.75 mm Transparent PU, Ninjatek, USA) and rigid PLA filament (1.75 mm Transparent PLA, ColorFabb, The Netherlands) were used for this study. The electrically conductive material integrated into the part was copper wire with a polyimide-coated layer (75 µm Cu wire, Remington Industries, USA).

### 5.2.2. Sample Fabrication

The 3D-printed samples were fabricated according to ASTM D3039-17 and following the same procedures as those used by Saleh et al. [25] with dimensions of $200 \times 25 \times 2$ mm$^3$. Table 5-1 shows the printing parameters of FFF samples. Based on these printing parameters, the absolute resistance value of the embedded Cu wire within the CWPC samples was in average of $107 \pm 3$ Ω. To introduce the embedded Cu wire within the polymer filament, the samples were fabricated using a modified open-source 3D printer (Prusa i3 MK2, Prusa Research, Prague, Czech Republic) and applying a customized G-code generated by a MATLAB script (MATLAB R2019b, Natick, Massachusetts: The MathWorks Inc.). Here, the Cu wire was introduced through a needle inserted into the heat block of the modified 3D printer (according to [19]) to the molten filament where they are co-extruded simultaneously through the nozzle. Figure 5-2 shows a microstructure of a cross-section of the 3D-printed CWPC sample.

Table 5-1. FFF printing parameters of the samples.

|  | PLA, PLA+Cu | TPU, TPU+Cu | Unit |
|---|---|---|---|
| Extruder temperature | 200 | 220 | °C |
| Bed temperature | 50 | 55 | °C |
| Printing speed | 15 | | mm/s |
| Nozzle diameter | 1 | | mm |
| Wire diameter | 0.075 | | mm |
| Raster width | 0.65 | | mm |
| Layer height | 0.5 | | mm |
| Printing angle | 0 | | ° |
| Number of rasters / layers | 38 | | |
| Number of layers | 4 | | |
| Fill density | 100 | | % |
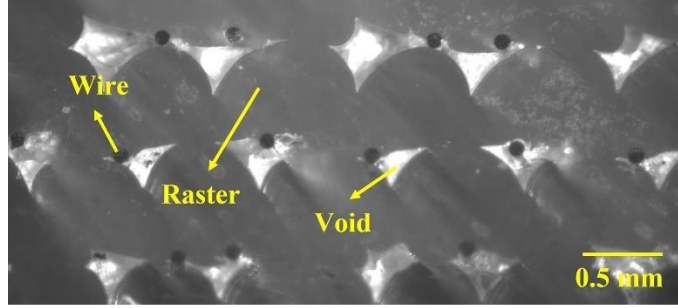
Figure 5-2. Microstructure of a 3D-printed CWPC cross-section.

To theoretically calculate the volume fraction of the Cu wire within the CWPC sample, Equation 5.1 was applied based on the printing parameters and the geometry of the 3D-printed sample. The volume fraction of the Cu wire was found to be 1.34% relative to the total CWPC sample volume.

$$v_w = L_{wire} * A_{wire} = (L_{wire/raster} * no. of\ rasters * no. of\ layers) * (\pi/4)D_{wire}^2 \qquad \text{(5.1-a)}$$

$$v_c = l * w * t \qquad \text{(5.1-b)}$$

$$V_w = \frac{v_w}{v_c} \qquad \text{(5.1-c)}$$

where $v_w$, and $v_c$ are the volume of wire and composite, respectively. $L_{wire}$, $A_{wire}$, and $D_{wire}$ are the length, the cross-section area, and the diameter of the wire, respectively. $L_{wire/raster}$ is the length of the wire in a single raster. $l$, $w$, and $t$ are the total length, width, and thickness of the 3D printed sample, respectively. $V_w$ is the volume fraction of the Cu wire within the CWPC.

In addition, the method used in [25] was followed to prepare samples for electrical resistance measurements. 3D-printed sample with extended Cu wire is represented in Figure 5-3a and b. End tabs of PLA with tapered angle were glued to the ends of the samples to avoid sample slippage from the grips of the test frame during the fatigue test. Figure 5-3c shows a schematic side-view of 3D-printed sample with end tabs and an enlarged schematic cross-section of the sample at A-A. Samples were manufactured in four different configurations: PLA, PLA+Cu, TPU, and TPU+Cu.

Nine samples for each configuration were manufactured, resulting in a total of 36 test samples for fatigue testing.
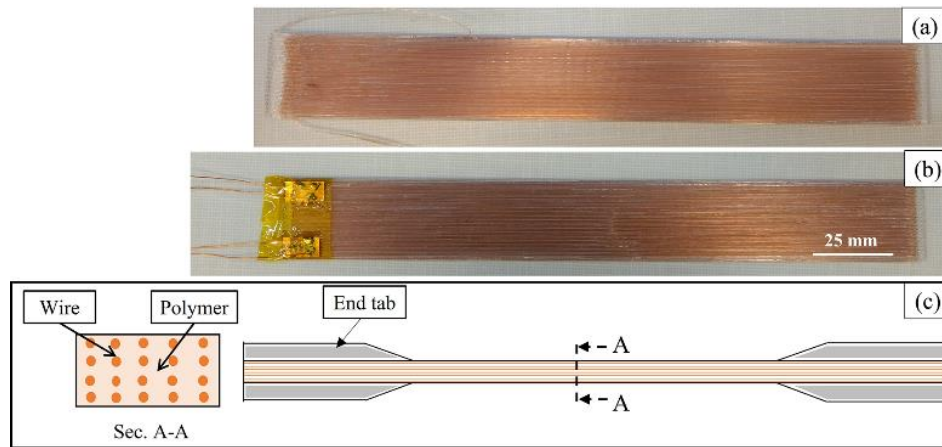


Figure 5-3. a) 3D-printed sample with extended Cu wire; b) sample with four-probe electrical terminal; c) 3D-printed sample with end tabs and enlarged cross-section of the sample at A-A.

### 5.2.3. Fatigue Testing

Polymers and their composites are sensitive to fatigue testing parameters such as applied strain or stress amplitude and mean, the cyclic rate, initial defects, and environmental conditions. Therefore, these parameters should be taken into consideration while designing a fatigue test. Firstly, to define the parameters of the fatigue test, a tensile test is needed to obtain the ultimate tensile strength (UTS) and failure strain of the material. These tensile properties were obtained from a previous study by Saleh et al. [25] on the same materials as shown in Table 5-2. For the strain-controlled fatigue test, 50% of the maximum strain at failure of the material was chosen as the maximum strain to be applied to the specimen. The strain at failure was predetermined as 0.02 mm/mm and 0.11 mm/mm for PLA-based and TPU-based materials, respectively [24,25]. Fatigue tests with sinusoidal waves were conducted using a universal test frame (Series 809 Axial/Torsional Test System, MTS Systems Co., USA) and applying tension–tension cycles with a frequency of 5 Hz.

The test frequency was selected to avoid self-heating, and a strain ratio of $R_s = 0.1$ was selected to avoid sample compression. Therefore, the strain was varied periodically from 0.001 mm/mm to 0.01 mm/mm for PLA based materials and from 0.0055 mm/mm to 0.055 mm/mm for TPU based materials. Because of the time-consuming nature of the fatigue test, only three sets of specific cycles of $10^2$, $10^4$, and $10^5$ were selected. The $10^5$ cycles were selected instead of $10^6$ cycles, as the one run of the test for the $10^6$ cycles would take several days which was not practical. Afterwards, residual tensile strength was measured to quantify the damage accumulation within the material for each condition.

Table 5-2. Tensile properties of PLA-based and TPU-based materials [25].

|  | PLA | PLA+Cu | TPU | TPU+Cu |
|---|---|---|---|---|
| Ultimate Tensile Strength, UTS MPa | 45.952 | 52.2 | 4.234 | 5.583 |
| Maximum strain at failure mm/mm | 0.02 | 0.02 | 0.11 | 0.11 |

### 5.2.4. Tensile Test After Fatigue

Tensile tests were conducted using the same test frame (Series 809 Axial/Torsional Test System, MTS Systems Co., USA) at a 2 mm/min crosshead rate and following the ASTM D3039-17 standard to measure the residual tensile strength after each fatigue test. The obtained stress-strain curves were then used to measure the residual Young's modulus of the sample after each fatigue test. Three samples were tested for each condition, and the average value was calculated.

A one-way analysis of variance (ANOVA) statistical test was performed to characterize significant change in residual stresses after each set of cycles for each condition. A confidence level of 95% was chosen for this test.

### 5.2.5. Electromechanical Test

The electrical resistance of the embedded Cu wire was measured in situ during the fatigue test using a digital multimeter (Agilent 34401A, Agilent Technologies Inc., Colorado, USA). Figure

5-4 shows the CWPC sample with the electrical connections. The electrical resistance was recorded at a rate of 2 Hz using a customized program (MATLAB R2019b, Natick, Massachusetts: The MathWorks Inc.). The electrical resistance recording rate (2 Hz) was synchronized with the fatigue testing rate (5 Hz) and sampling rate (10 Hz), as shown in Figure 5-5, to determine the correlation between the fractal change in electrical resistance (given by Equation 5.2) and the applied strain. For the integrated metal wire in CWPC, the change in electrical resistance under strain is based on the change of the geometry of the wire as explained in Equation 5.3 [24]. This test also indicates wire breakage within the sample when a sudden increase occurs in the electrical resistance reading.

$$Fractional\ change\ of\ electrical\ resistance\ (\Delta R/R) = \frac{R_i - R}{R} \tag{5.2}$$

where $R_i$ is the sample resistance measured during cyclic loading, and $R$ is the sample's initial resistance before loading.

$$R = \rho \frac{L_{wire}}{A_{wire}} \tag{5.3}$$

where $R$ is the sample's initial resistance, $\rho$ is the resistivity of the wire, $L_{wire}$ is the length of the wire, and $A_{wire}$ is the cross-section area of the wire.
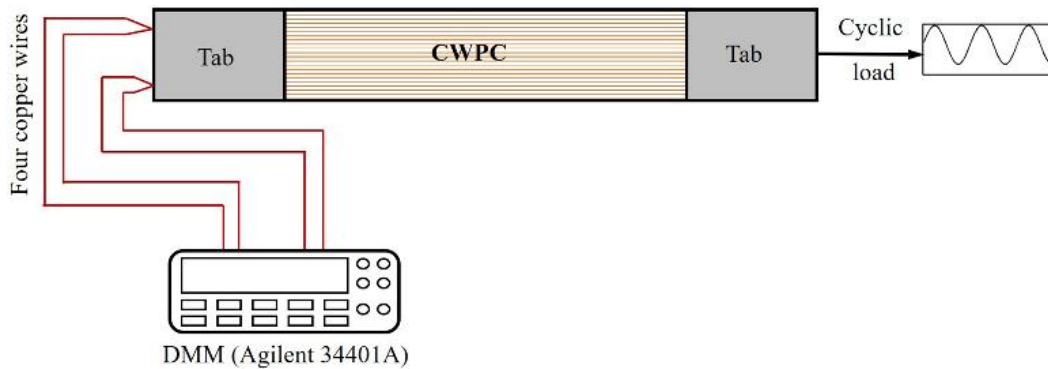


Figure 5-4. Schematic representation of CWPC sample with electrical connections.
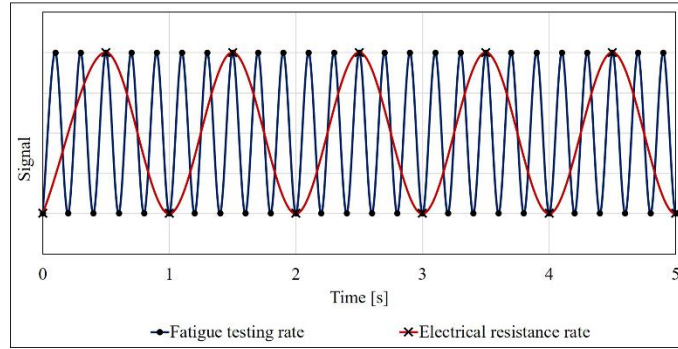
Figure 5-5. Synchronization rate between fatigue testing and electromechanical testing

### 5.2.6.    Digital Image Correlation (DIC)

To accurately obtain strain measurements, the 2D DIC technique was used to obtain a full-field strain map of the sample under the fatigue test. Damage accumulation as the cycles progressed was then investigated. The sample should have significant contrast for image processing and correlation. The samples were first prepared by white speckling (5211 Opaque White, Createx Airbrush Colors, Createx Colors, East Granby, CT, USA) over a black background (2X Ultra Cover, Rust-Oleum Corp, Concord, ON, Canada). Also, the sample was illuminated using two light-emitting diode panels (Neewer 2 Packs LED light, Neewer, Shenzhen, China).

First, a reference image of the unloaded sample was captured before the cyclic test using a 5M Basler camera (acA2440-35um, Basler AG, Ahrensburg, Germany) with a 50 mm focal length lens (KOWA LM50JCM 2/3" 50MM F2.8, RMA Electronics, USA) placed 0.5 m away from the sample. This reference image was then used to compute the full-field strain/strain maps at different fatigue intervals and at maximum and minimum applied strains by correlating the reference image with consecutive images. The strain measurements were conducted using DIC software (DaVis version 10.0.3 StrainMaster, LaVision GmbH, Gottingen, Germany); for correlation, a 60 x 60 pixel subset size with a 20 pixel step size was applied on the surface of the captured images. Average strain within the surface was calculated over a 25 mm x 50 mm field of view (FOV) as

116

presented in Figure 5-6a. Experimental setup showing all components of testing is represented in Figure 5-6b.
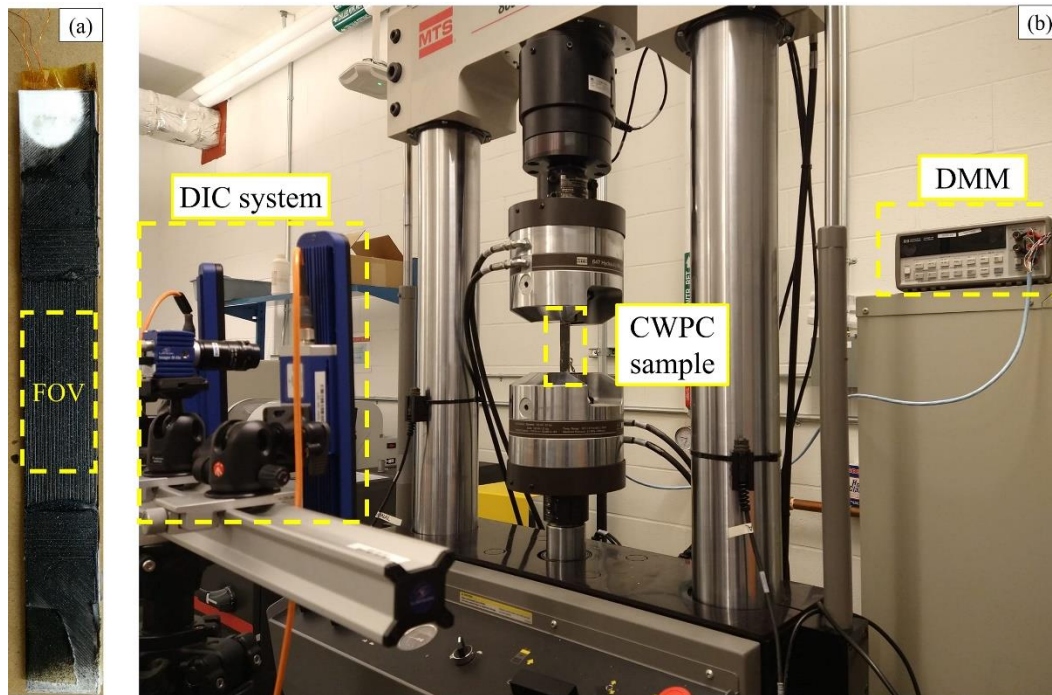


Figure 5-6. a) Painted and speckled sample with the field of view; b) Experimental setup of fatigue and electromechanical testing using DIC technique.

## 5.3. Fatigue Analytical Modelling

An analytical model was applied to predict the fatigue life before failure of the Cu wire within the part under a specific applied strain. The calculated results were then compared with the electromechanical experimental data.

Out of different fatigue life analytical models such as stress-life, strain-life, and linear elastic fracture mechanics models, a strain-life analytical model is applied in this study. For this model, four common approaches were applied: the Coffin–Manson approach (Equation 5.6), the Morrow mean stress equation (Equation 5.7), the modified Morrow approach (Equation 5.8), and the

Walker mean stress equation (Equation 5.9) [36,37] to investigate which agreed most with the experimental data. The equations of all of these approaches include the material's elastic and plastic strain [36,38].

**Coffin–Manson Approach**

From different test sets, elastic and plastic strains are plotted against the fatigue life, $N_f$ on a log-log scale. The elastic strains often give a straight line of shallow slope, while the plastic strains give a straight line of steeper slope. Then, equations are fitted to these lines as shown in Equation 5.4 [36].

$$\varepsilon_{ea} = \frac{\sigma_f'}{E}(2N_f)^b, \qquad \varepsilon_{pa} = \varepsilon_f'(2N_f)^c \qquad (5.4)$$

where $\varepsilon_{ea}$ is the elastic strain, $\varepsilon_{pa}$ is the plastic strain, $E$ is the Young's modulus of the copper, $\sigma_f'$, $\varepsilon_f'$, $c$, and $b$ are strain-life constants, and $N_f$ is the fatigue life. For this study, the strain-life constants for Cu were obtained from [39]. The strain amplitude, $\varepsilon_a$ is a combination of both elastic and plastic strains (Equation 5.5). The form that combines these strains together is called the Coffin-Manson approach as presented in Equation 5.6 [36].

$$\varepsilon_a = \varepsilon_{ea} + \varepsilon_{pa} \qquad (5.5)$$

$$\varepsilon_a = \frac{\sigma_f'}{E}(2N_f)^b + \varepsilon_f'(2N_f)^c \qquad (5.6)$$

This is the simplest method because it assumes fully reversed cycles with $R_s = -1$ and zero mean stress. However, in this study, the mean stress affected the fatigue behaviour of the materials because $R_s = 0.1$. The other three abovementioned approaches consider the effect of mean stress, as described in the following equations.

**Morrow Mean Stress Equation**

In this model (Equation 5.7), the effect of mean stress is considered for both terms of the strain-life equation (elastic strain term and plastic strain term) [36].

$$\varepsilon_a = \frac{\sigma_f'}{E}(1 - \frac{\sigma_m}{\sigma_f'})(2N_f)^b + \varepsilon_f'(1 - \frac{\sigma_m}{\sigma_f'})^{c/b}(2N_f)^c \qquad (5.7)$$

where $\varepsilon_a$ is the strain amplitude, $E$ is the Young's modulus of the copper, $\sigma_f', \varepsilon_f', c$, and $b$ are strain-life constants, $\sigma_m$ is the applied mean stress corresponding to the applied strain, and $N_f$ is the fatigue life.

**Modified Morrow Approach**

Here, the mean stress effect is neglected in the plastic strain term of the equation (Equation 5.8). Hence, the plastic strain is considered to be dominant such that the mean stress is relatively small compared with the plasticity behaviour of the material [36].

$$\varepsilon_a = \frac{\sigma_f'}{E}(1 - \frac{\sigma_m}{\sigma_f'})(2N_f)^b + \varepsilon_f'(2N_f)^c \qquad (5.8)$$

where $\varepsilon_a$ is the strain amplitude, $E$ is the Young's modulus of the copper, $\sigma_f', \varepsilon_f', c$, and $b$ are strain-life constants, $\sigma_m$ is the applied mean stress corresponding to the applied strain, and $N_f$ is the fatigue life.

**Walker Mean Stress Equation**

This model has an additional adjustable fitting parameter ($\gamma$), as shown in Equation 5.9 [36]. More research is needed to validate this parameter, especially for non-ferrous metals such as aluminum and copper. Therefore, in this study, the ($\gamma$) value was extracted from the literature [40].

$$\varepsilon_a = \frac{\sigma_f'}{E}(\frac{1-R}{2})^{(1-\gamma)}(2N_f)^b + \varepsilon_f'(\frac{1-R}{2})^{c(1-\gamma)/b}(2N_f)^c \qquad (5.9)$$

where $\varepsilon_a$ is the strain amplitude, $E$ is the Young's modulus of the copper, $\sigma_f'$, $\varepsilon_f'$, $c$, and $b$ are strain-life constants, $R$ is the stress ratio ($\sigma_{min}/\sigma_{max}$), $N_f$ is the fatigue life, and $\gamma$ is a material constant.

## 5.4.  Results and Discussion

### 5.4.1.  Fatigue Behaviour

The behaviour of the material as cyclic loading progresses is described by the stress-strain loops shown in Figure 5-7. For the strain-controlled fatigue tests, stress relaxation was observed with increasing number of cycles, and it occurred from the beginning of the test. This phenomenon was also observed by Tao et al. [34] for epoxy polymer. As shown in Figure 5-7, the material's elastic modulus decreased as the number of cycles increased, indicating progressive evolution of damage within the part. Senatov et al. [41] state that within one cycle dissipated energy in the part includes heat loss and defect formation. Therefore, the hysteresis loop area indicating the dissipated energy is larger for composite materials (Figure 5-7b and d) than pure materials (Figure 5-7a and c) because the wire within the part increases the probability of defect formation.

Rigotti et al. [7] studied the damage evolution of flexible 3D-printed TPU. They observed damage evolution within the samples by analyzing the absorbed energy behavior within the fatigue cycles. The hysteresis loop area decreased as the number of cycles increased and as the stress–strain loops became more linear and slimmer, indicating damage evolution. Figure 5-7c and d support this observation because a drop of absorbed energy can be seen. Similar observations were also reported by [34,41].
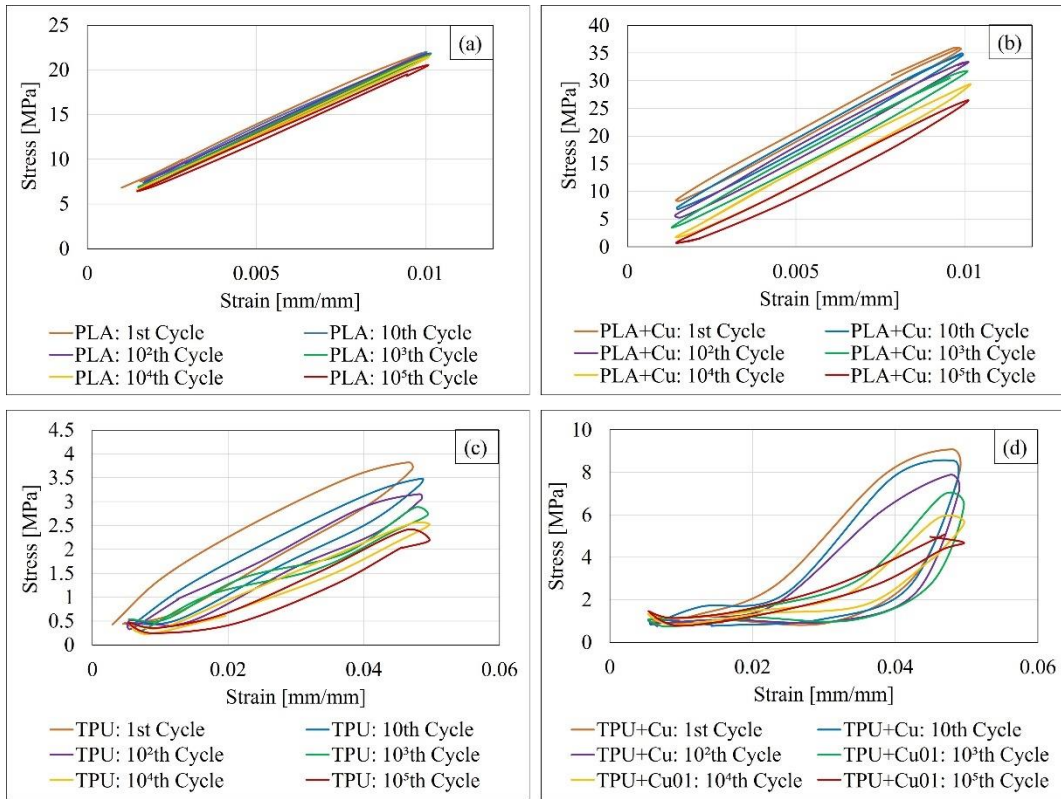
Figure 5-7. Stress–strain loops at an increasing number of cycles under fatigue test; a) PLA, b)

PLA+Cu, c) TPU, d) TPU+Cu.

Figure 5-8 shows an example of stress–strain curves of the four compositions after each fatigue

test. An original plot of the stress-strain curve of the samples obtained from [25] was represented

also in Figure 5-8. This shows that the strength of the material decreases with an increasing number

of cycles. These plots were then used to calculate the residual strengths of each composition after

$10^2$, $10^4$, and $10^5$ cycles, as shown in Figure 5-9. In Figure 5-9, the results are presented as the

average values of the three replicates with error bars representing the standard deviation. The error

between readings may be attributed to the nature of the 3D-printing process for which voids are

commonly exist within the part resulting in inhomogeneous printed sample [6,24,25]. The decrease

in mechanical properties as the number of cycles increased for PLA and its composite is lower

than for TPU and its composite. The UTS of the same four compositions was measured by Saleh

121

et al. [25]. Based on these results, the reduction of the residual strengths was investigated and compared to the UTS after each set of cycles. Table 5-3 shows the ratio of the residual strengths compared to the UTS of each composition. The residual strength is lower for TPU-based materials than for PLA-based materials. This may be attributed to the maximum applied stress on the sample corresponding to 50% of the failure strain. In the case of PLA-based material, the maximum corresponding applied stress was around 47% and 67% of the UTS of PLA and PLA CWPC, respectively. For TPU-based material, the maximum corresponding applied stress was much higher than that of PLA at around 85% and 80% of the UTS of TPU and TPU CWPC, respectively. In another study, Saleh et al. [26] state that composite material is considered to fail when its residual strength is less than 85% of its UTS. Thus, TPU and TPU CWPC failure occurs when these materials are subjected to more than $10^4$ cycles under 50% of their failure strain (Table 5-3). These results were confirmed by applying a statistical one-way ANOVA test to check the significance of strength differences between the UTS and the residual strengths after $10^2$, $10^4$, and $10^5$ cycles for each composition. Table 5-4 shows no significance between the UTS and the residual strength values after $10^2$, $10^4$, and $10^5$ cycles for PLA and PLA CWPC. However, for TPU and TPU CWPC, the residual strength decreased significantly with an increase in the number of cycles. Based on the fatigue behavior of these four compositions, it can be concluded that these FFF CWPC materials with different properties can be successfully designed to be used for different structures subjected to cyclic loading.
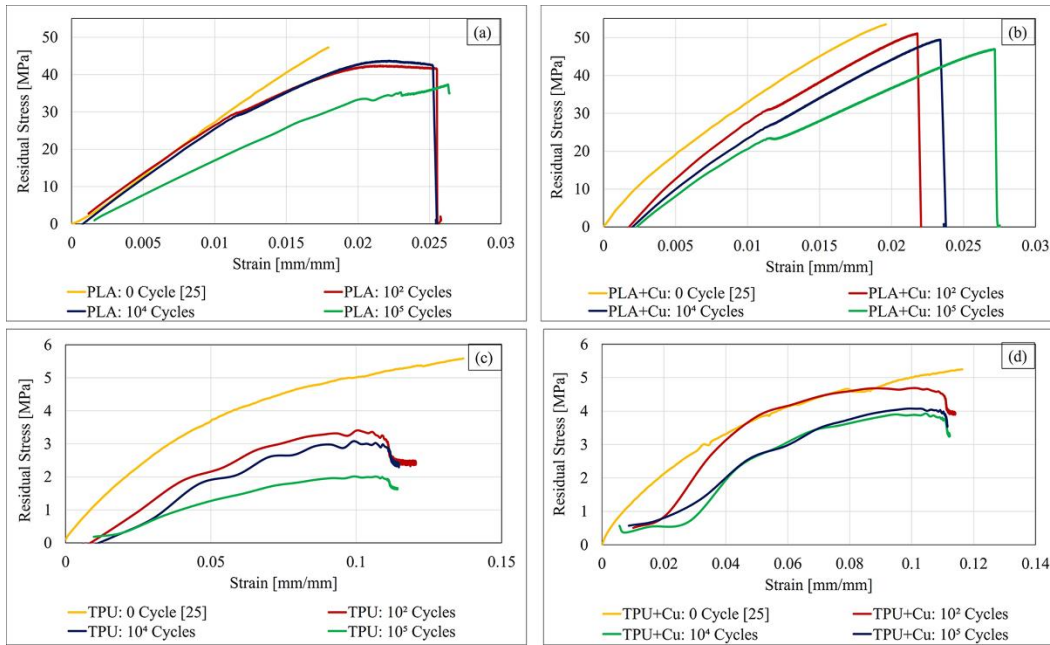
Figure 5-8. Stress–strain curve for increasing number of fatigue cycles for a) PLA, b) PLA+Cu,

c) TPU, d) TPU+Cu.
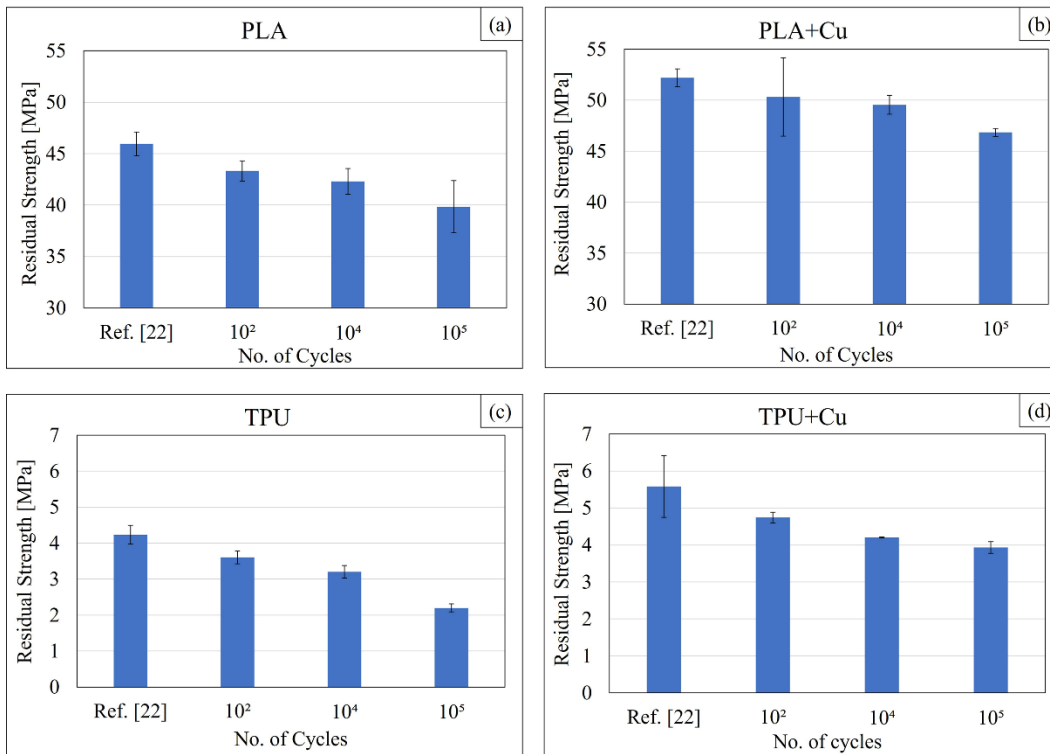


Figure 5-9. Residual strength after different sets of cycles; a) PLA, b) PLA+Cu, c) TPU, d)

TPU+Cu

Table 5-3. The ratio of residual strength compared to the UTS of four compositions with different cycle sets.

| | No. of cycles | PLA | PLA+Cu | TPU | TPU+Cu |
|---|---|---|---|---|---|
| UTS [MPa] [25] | | 45.952 | 52.2 | 4.234 | 5.583 |
| Residual stress/UTS [%] | $10^2$ | 94.3 | 96.4 | 85.1 | 84.9 |
| Residual stress/UTS [%] | $10^4$ | 92 | 94.9 | 75.7 | 75.3 |
| Residual stress/UTS [%] | $10^5$ | 86.7 | 89.7 | 52 | 70.5 |

The slope of the initial linear portion of the curves in Figure 5-8 was used to calculate the residual Young's modulus as shown in Figure 5-10. It can be seen that all four compositions showed a decrease in the Young's modulus with the number of cycles compared to the original Young's modulus of the materials before the fatigue test. This was verified by applying the statistical ANOVA test which showed a statistical significance between the values of Young's modulus with the number of cycles as indicated in Table 5-4. The degradation of materials Young's modulus under fatigue testing may be attributed to the accumulation of matrix microcracks as mentioned by Samareh-Mousavi et al. [42]. In addition, Gong et al. [38] related the reduction of Young's modulus of 3D-printed scaffolds PLA to the cyclic stress-strain softening behaviour of the material under strain-controlled fatigue test.
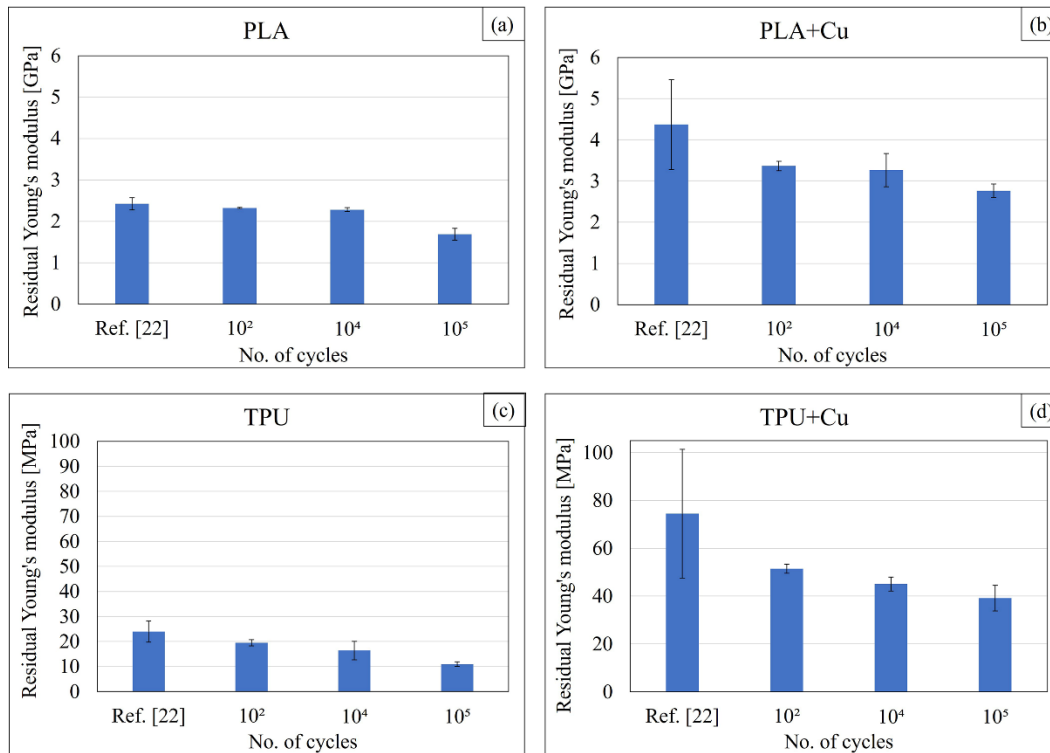
Figure 5-10. Residual Young's modulus after different sets of cycles; a) PLA, b) PLA+Cu, c) TPU, d) TPU+Cu

Table 5-4. One-way ANOVA test to compare tensile strength and Young's modulus before and after the different number of cycles for the four compositions (S: statistically significant, NS: statistically not significant).

| | Tensile strength | | Young's modulus | |
|---|---|---|---|---|
| | P-Value | Statistical significance | P-Value | Statistical significance |
| PLA | 0.0707 | NS | <0.001 | S |
| PLA+Cu | 0.0602 | NS | <0.001 | S |
| TPU | <0.001 | S | <0.001 | S |
| TPU+Cu | <0.001 | S | <0.001 | S |

### 5.4.2. DIC Results

To better understand the behaviour of the material under fatigue test, DIC measurements were performed to capture images of the surface of the sample for different sets of cycles. A fatigue test of $10^5$ cycles was used to study damage accumulation within the sample. The time required to

process digital images is high; therefore, a low rate of 0.06 Hz was applied for the images being processed for the $10^5$ cycles fatigue test. In Figure 5-11c and d, the behaviour of the PLA-based samples under minimum applied strain is represented by images processed at the 2$^{nd}$ (No. 1) and 76500$^{th}$ (No. 3) cycle, for both PLA and PLA CWPC materials. The image processed at the 38500$^{th}$ (No. 2) cycle represents the full-field strain map of the sample under maximum applied strain. To study the damage evolution, images were processed at the 17500$^{th}$ (No. 4), 58000$^{th}$ (No. 5), and 90000$^{th}$ (No. 6) cycle for both PLA (Figure 5-11c) and PLA CWPC (Figure 5-11d). It can be seen that for the PLA and PLA CWPC (Figure 5-11), the full-field strain maps are quite similar for the same strain level (Nos. 4, 5, and 6) regardless of the number of cycles, indicating no significant damage accumulation within the sample. The strain maps at different number of cycles in Figure 5-11c and d shows more deformation in case of PLA (Figure 5-11c) compared to PLA+Cu (Figure 5-11d) for each demonstrated cycle and this may be attributed to the higher strength of PLA+Cu compared to PLA (Table 5-3).

Figure 5-12c and d show the full-field strain map at minimum strain at the 2$^{nd}$ (No. 1) and the 72500$^{th}$ (No. 3) cycle for TPU and TPU CWPC. The processed image at the 35500$^{th}$ (No. 2) cycle represents the strain map at the maximum strain. The damage evolution was studied by processing the images at the 16500$^{th}$ (No. 4), 53500$^{th}$ (No. 5), and 88000$^{th}$ (No. 6) cycle (Figure 5-12). There are some differences in the strain maps (No. 4, 5, and 6) for both TPU (Figure 5-12c) and TPU CWPC (Figure 5-12d); this indicates damage accumulation within the flexible material as the number of cycles increased, which was not the case for PLA-based materials (Figure 5-11). The results shown in Figure 5-11 and Figure 5-12 agree with the statistical results shown in Table 5-4. The strain maps at different number of cycles in Figure 5-12c and d shows more deformation in case of TPU (Figure 5-12c) compared to TPU+Cu (Figure 5-12d) for each demonstrated cycle and

this may be attributed to the higher strength of TPU+Cu compared to TPU (Table 5-3). Generally, it can be obviously seen that the values of axial strain under cyclic loading for TPU-based materials (Figure 5-12) is higher than that of PLA-based materials (Figure 5-11) and this is because the flexible nature of TPU-based materials compared to the PLA-based materials.
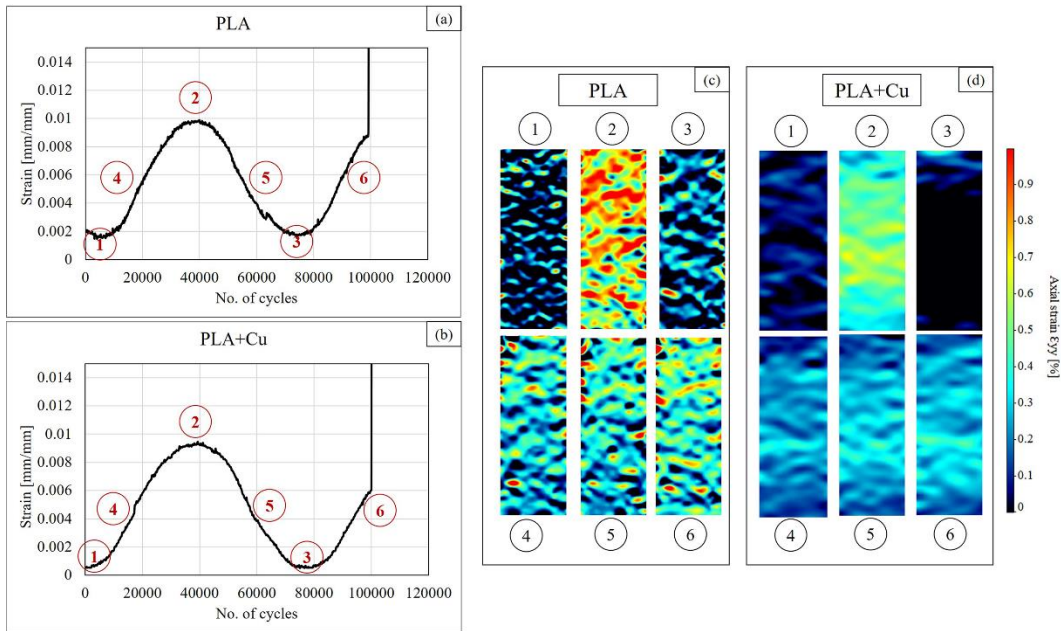


Figure 5-11. Axial strain progression using a 2D DIC system; a) strain progression with increasing number of cycles for PLA, b) strain progression with increasing number of cycles for PLA+Cu, c) strain maps for increasing number of cycles for PLA, d) strain maps for increasing number of cycles for PLA+Cu.
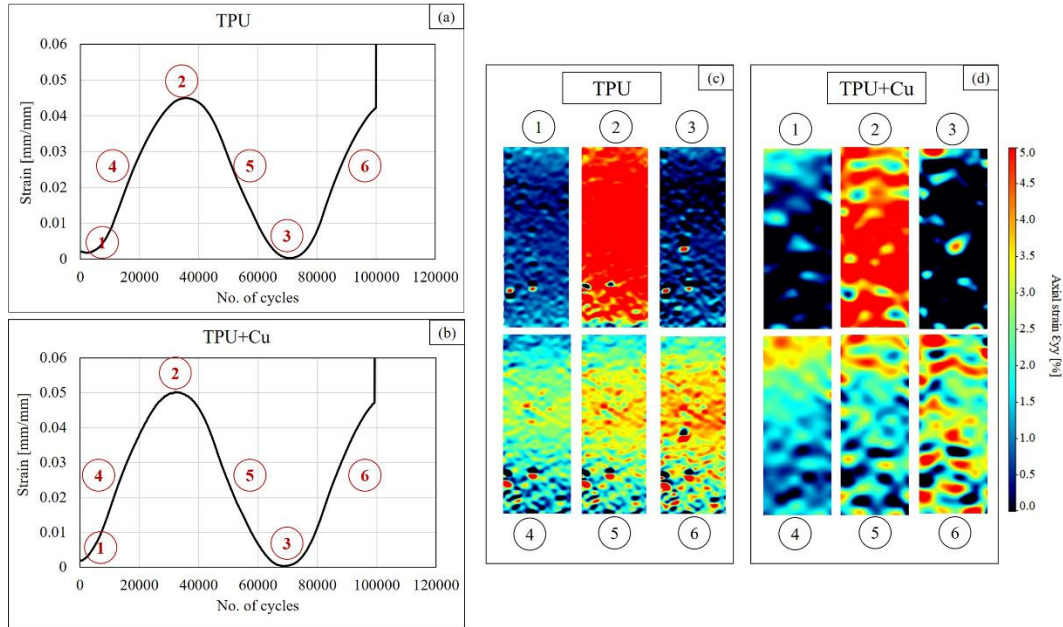
Figure 5-12. Axial strain progression using a 2D DIC system; a) strain progression with increasing number of cycles for TPU, b) strain progression with increasing number of cycles for TPU+Cu, c) strain maps for increasing number of cycles for TPU, d) strain maps for increasing number of cycles for TPU+Cu.

### 5.4.3. Electromechanical Properties

The ability of CWPCs to sense material deformation under cyclic loading is demonstrated in Figure 5-13 which shows the change in fractional electrical resistance of Cu wire with an increasing number of cycles when the CWPCs were subjected to fatigue test. In the case of rigid PLA CWPC, the applied cyclic strain broke the Cu wire at around 30000 cycles. After this, there was an increase in the electrical resistance fractional change before final wire failure at approximately 36000 cycles when the change in electrical resistance suddenly increased. However, for TPU CWPC, the wire sustained approximately 180 cycles before breakage. The longer fatigue life of PLA CWPC compared with TPU CWPC may be attributed to the value of the applied stress for each composite, as mentioned earlier. For PLA CWPC, the stress corresponding to 50% failure

strain is around 67% of the UTS, which is lower than for TPU CWPC with an applied stress of approximately 80% of the UTS. The gradual increase in the fractional change of the electrical resistance before the failure of the wire for TPU CWPC (Figure 5-13b) may be attributed to a permanent deformation/elongation of the Cu wire under applied strain.
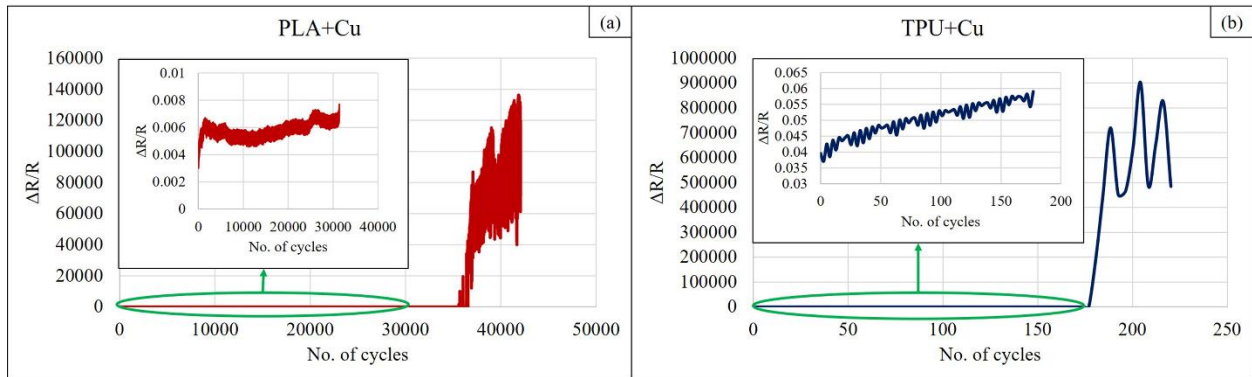


Figure 5-13. Fractional change of electrical resistance with increasing number of cycles for (a) PLA+Cu, (b) TPU+Cu

Figure 5-14 shows the applied strain and fractional change in electrical resistance on the primary and secondary axes, respectively, with the progressive number of cycles for both PLA CWPC (Figure 5-14a and b) and TPU CWPC (Figure 5-14c and d). A small specific range of sets of cycles (20–50 cycles) was selected to demonstrate changes in resistance with changes in applied strain, as shown in Figure 5-14b and d. The electrical resistance changes upon loading and unloading indicate a reverse piezoresistance behavior for both PLA CWPC and TPU CPWC. The results of this test show the applicability of this type of FFF material to be used as a self-sensor for a wide range of structural health monitoring applications, for both rigid and flexible structures.
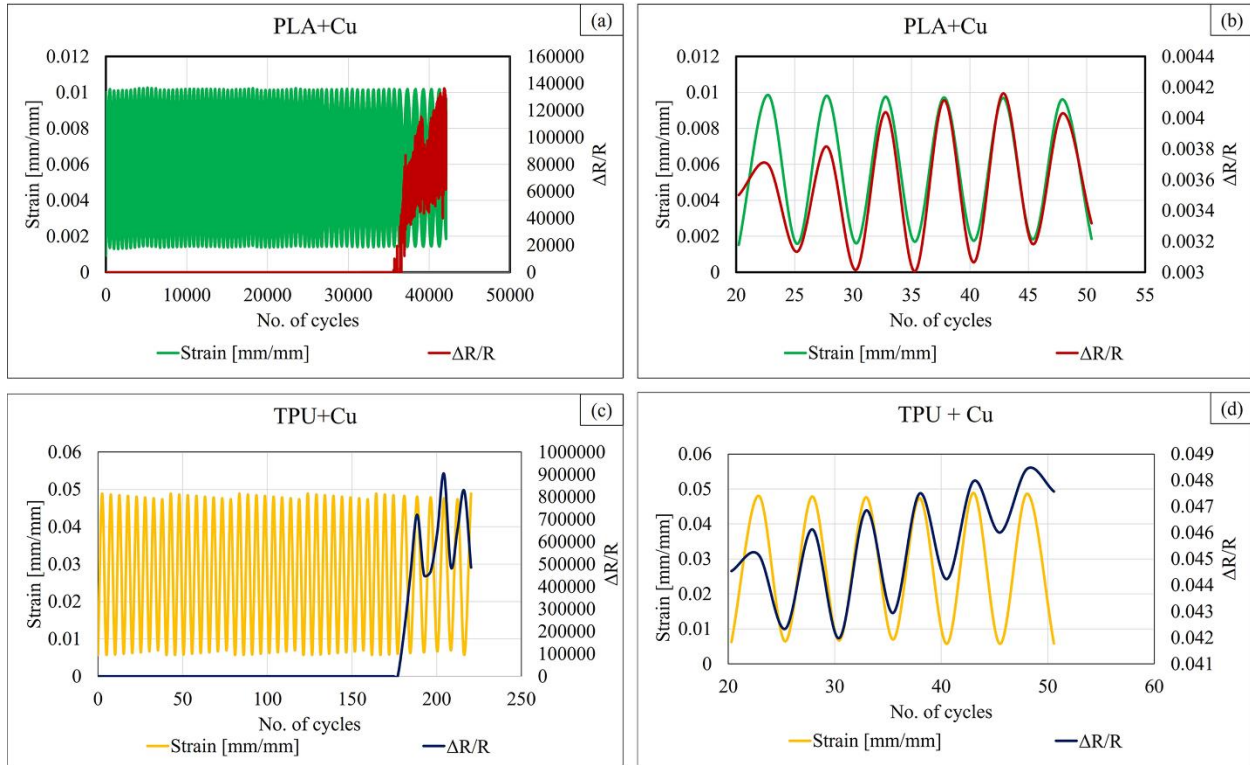
Figure 5-14. Change in electrical resistance and strain for an increasing number of cycles: (a) PLA+Cu, (b) PLA+Cu from 20 to 50 cycles, (c) TPU+Cu, (d) TPU+Cu between 20 and 50 cycles.

### 5.4.4. Strain-Life Analytical Model Results

A strain-life analytical model was implemented using four different approaches, as indicated by Equations 5.6–5.9. The fatigue life of PLA CWPC is represented in Table 5-5 for each approach. It can be noted that the Coffin–Manson approach, Morrow approach, and modified Morrow approach showed agreement of fatigue life when compared with the experimental results ($N_f = 30000$ *cycles*) obtained from the electromechanical test at an applied mean strain of 0.0045 mm/mm. However, for the Walker mean stress equation, the fatigue life was much smaller than that of the experimental data; this may be attributed to error in the assumed value of $\gamma$ and the maximum and minimum applied stresses included in the Walker equation which were calculated

based on the maximum and minimum applied strain on the material. However, in the test, the samples experienced stress relaxation under cyclic loading, which means that the value of the applied stress on the sample during the test was not constant. Thus, the result of the latter approach is not accurate. The fatigue life of TPU CWPC is represented in Table 5-5 for each approach. As mentioned before, there was agreement between the fatigue life obtained from the electromechanical test and the Coffin–Manson approach, Morrow approach, and modified Morrow approach at an applied mean strain of 0.025 mm/mm, though the result of the Walker mean stress equation was not similar to the experimental result. In conclusion, for both types of materials it is recommended to use the modified Morrow approach to predict the fatigue life of CWPC because it considers the effect of mean stress on fatigue life with more accurate results than the Morrow approach and the Walker mean stress equation. This model can predict the failure of a wire/sensor integrated within the part under a strain-controlled fatigue test.

Table 5-5. Strain-life analytical model of PLA and TPU CWPC.

| | | Coffin–Manson Approach | Morrow Approach | Modified Morrow Approach | Walker Mean Stress Equation |
|---|---|---|---|---|---|
| PLA+Cu | $\varepsilon_a$ [mm/mm] | 0.0045 | 0.0045 | 0.0045 | 0.0045 |
| | $N_f$ [Cycles] | 28000 | 27500 | 28000 | 5500 |
| TPU+Cu | $\varepsilon_a$ [mm/mm] | 0.025 | 0.025 | 0.025 | 0.025 |
| | $N_f$ [Cycles] | 150 | 130 | 150 | 60 |

## 5.5. Summary and Conclusions

The fatigue behaviour of 3D-printed continuous wire polymer composites (CWPCs) was characterized for rigid (PLA-based) and flexible (TPU-based) variants. Their electromechanical

properties under fatigue testing were compared for both types and the results demonstrate the applicability of these materials for structural health monitoring applications subjected to dynamic loading.

Changes in residual strengths measured after $10^2$, $10^4$, and $10^5$ cycles were insignificant in the PLA-based materials and significant in the TPU-based materials. This indicates more damage accumulation for TPU-based materials than PLA-based materials.

Digital image correlation (DIC) images presented full-field strain maps of the sample surface for different sets of cycles which provided a deep understanding of the fatigue behaviour of CWPCs under cyclic loading. The strain maps of TPU-based materials showed more damage accumulation as cycles increased than for PLA-based materials.

The electrical resistance changed reversibly upon loading and unloading, indicating reverse piezoresistance behavior of the material for both PLA CWPC and TPU CPWC. The Cu wire for TPU CWPC failed at a lower number of cycles (180 cycles) than PLA CWPC (30000 cycles).

The strain-life analytical model showed agreement between the experimental and model results for fatigue life when the Coffin–Manson approach, Morrow approach, and modified Morrow approach were implemented. Specifically, application of the modified Morrow approach is recommended for wire inserted in CWPC to predict the sensor's failure under a strain-controlled fatigue test. However, the Walker mean stress equation showed a difference between the fatigue life and the experimental data.

In summary, this study proved the applicability of CWPC structures with tunable properties to be used as strain sensors for structural health monitoring applications subjected to dynamic loading. However, further research is still required to fully understand the behavior of CWPC material

under fatigue testing by applying other different testing parameters such as the loading amplitude, loading frequency, and loading ratio. The applied analytical model in this study will allow for manufacturers and designers to predict the fatigue life of CWPC parts.

## 5.6.  References

[1]     Afrose MF, Masood SH, Iovenitti P, Nikzad M, Sbarski I. Effects of part build orientations on fatigue behaviour of FDM-processed PLA material. Prog Addit Manuf 2016;1:21–8.

[2]     Susmel L, Ahmed AA. A material length scale – based methodology to assess static strength of notched additively manufactured polylactide (PLA). Fatigue Fract Eng Mater Struct 2018;41:2071–98.

[3]     Safai L, Cuellar JS, Smit G, Zadpoor AA. A review of the fatigue behavior of 3D printed polymers. Addit Manuf 2019;28:87–97.

[4]     Ahmed AA, Susmel L. Static assessment of plain / notched polylactide (PLA) 3D - printed with different infill levels: Equivalent homogenised material concept and Theory of Critical Distances. Fatigue Fract Eng Mater Struct 2019;42:883–904.

[5]     Giannakis E, Koidis C, Kyratsis P, Tzetzis D. Static and fatigue properties of 3D printed continuous carbon fiber nylon composites. Int. J. Mod. Manuf. Technol 2019;11:69-76.

[6]     Melenka GW, Cheung BKO, Schofield JS, Dawson MR, Carey JP. Evaluation and prediction of the tensile properties of continuous fiber-reinforced 3D printed structures. Compos Struct 2016;153:866–75.

[7]     Rigotti D, Dorigato A, Pegoretti A. Low-cycle fatigue behavior of flexible 3D printed thermoplastic polyurethane blends for thermal energy storage/release applications. J App

Polym Sci. 2021 Jan 15;138(3):49704.

[8]     Molony S, Brooks H, Tyas D. Tensile and fatigue failure of 3D printed parts with continuous fibre reinforcement. Int J Rapid Manuf 2017;6:97–113.

[9]     Vanaei HR, Shirinbayan M, Vanaei S, Fitoussi J, Khelladi S, Tcharkhtchi A. Multi-scale damage analysis and fatigue behavior of PLA manufactured by fused deposition modeling (FDM). Rapid Prototyp J 2021;27:371–8.

[10]    Ziemian C, Sharma M, Ziemi S. Anisotropic Mechanical Properties of ABS Parts Fabricated by Fused Deposition Modelling. Mech Eng 2012;23:159-80.

[11]    Ahn SH, Montero M, Odell D, Roundy S, Wright PK. Anisotropic material properties of fused deposition modeling ABS. Rapid Prototyp J 2002;8:248–57.

[12]    Montero M, Roundy S, Odell D. Material characterization of fused deposition modeling (FDM) ABS by designed experiments. Soc Manuf Eng 2001;10:1–21.

[13]    Hambali RH, Smith P, Rennie AEW. Determination of the effect of part orientation to the strength value on additive manufacturing FDM for end-use parts by physical testing and validation via three-dimensional finite element analysis. Int J Mater Eng Innov 2012;3:269–81.

[14]    Rigon D, Ardengo G, Meneghetti G. Static mechanical properties of virgin and recycled short glass fiber-reinforced polypropylene produced by pellet additive manufacturing. Fatigue Fract Eng Mater Struct 2021;9:2554–69.

[15]    Iizuka K, Todoroki A, Takahashi T, Ueda M. Reverse piezo-resistivity of 3D printed continuous carbon fiber/PA6 composites in a low stress range. Adv Compos Mater

2021;30:380–95.

[16]    Carneiro OS, Silva AF, Gomes R. Fused deposition modeling with polypropylene. Mater. Des. 2015 Oct 15;83:768-76.

[17]    Shofner ML, Lozano K, Rodríguez-Macías FJ, Barrera E V. Nanofiber-reinforced polymers prepared by fused deposition modeling. J Appl Polym Sci 2003;89:3081–90.

[18]    Brooks H, Molony S. Design and evaluation of additively manufactured parts with three dimensional continuous fibre reinforcement. Mater Des 2016;90:276–83.

[19]    Ibrahim Y, Melenka GW, Kempers R. Additive manufacturing of Continuous Wire Polymer Composites. Manuf Lett 2018;16:49–51.

[20]    Ibrahim Y, Melenka GW, Kempers R. Fabrication and tensile testing of 3D printed continuous wire polymer composites. Rapid Prototyp J 2018;24:1131–41.

[21]    Ibrahim Y, Melenka GW, Kempers R. Flexural properties of three-dimensional printed continuous wire polymer composites. Mater Sci Technol 2019;35:1471-82.

[22]    Ibrahim Y, Kempers R. Effective thermal conductivity of 3D - printed continuous wire polymer composites. Prog Addit Manuf 2022.

[23]    Ibrahim Y, Elkholy A, Schofield JS, Melenka GW, Kempers R. Effective thermal conductivity of 3D-printed continuous fiber polymer composites. Adv Manuf Polym Compos Sci 2020;6:17–28.

[24]    Saleh MA, Kempers R, Melenka GW. 3D printed continuous wire polymer composites strain sensors for structural health monitoring. Smart Mater Struct 2019;28:105041.

[25]    Saleh MA, Kempers R, Melenka GW. A comparative study on the electromechanical

properties of 3D-Printed rigid and flexible continuous wire polymer composites for structural health monitoring. Sensors Actuators, A Phys 2021;328:112764.

[26] Saleh MA, Al Haron MH, Saleh AA, Farag M. Fatigue behavior and life prediction of biodegradable composites of starch reinforced with date palm fibers. Int J Fatigue 2017;103:216–22.

[27] Giancane S, Panella FW, Nobile R, Dattoma V. Fatigue damage evolution of fiber reinforced composites with digital image correlation analysis. Procedia Eng 2010;2:1307–15.

[28] Santos E, Abe F, Kitamura Y, Osakada K, Shiomi M. Mechanical properties of pure titanium models processed by selective laser melting. In2002 International Solid Freeform Fabrication Symposium. Austin; 2002: 180–6.

[29] Brandl E, Heckenberger U, Holzinger V, Buchbinder D. Additive manufactured AlSi10Mg samples using Selective Laser Melting (SLM): Microstructure, high cycle fatigue, and fracture behavior. Mater Des 2012;34:159–69.

[30] Qiao P, Yang M. Fatigue life prediction of pultruded E-glass/polyurethane composites. J Compos Mater 2006;40:815–37.

[31] Liber-Kneć A, Kuźniar P, Kuciel S. Accelerated Fatigue Testing of Biodegradable Composites with Flax Fibers. J Polym Environ 2015;23:400–6.

[32] Montesano J, Selezneva M, Levesque M, Fawaz Z. Modeling fatigue damage evolution in polymer matrix composite structures and validation using in-situ digital image correlation. Compos Struct 2015;125:354–61.

[33] Loos MR, Yang J, Feke DL, Manas-Zloczower I, Unal S, Younes U. Enhancement of fatigue life of polyurethane composites containing carbon nanotubes. Compos Part B Eng 2013;44:740–4.

[34] Tao G, Xia Z. A non-contact real-time strain measurement and control system for multiaxial cyclic/fatigue tests of polymer materials by digital image correlation method. Polym Test 2005;24:844–55.

[35] Wang X, Chung DDL. Self-monitoring of fatigue damage and dynamic strain in carbon fiber polymer-matrix composite. Compos Part B Eng 1998;29:63–73.

[36] Shigley JE, Mischke CR, Brown Jr TH. Standard handbook of machine design. 9th ed. New York, USA: McGraw-Hill Education; 2004.

[37] Dowling NE. Mechanical behaviour of materials. 4th ed. UK: Pearson; 2012.

[38] Gong B, Cui S, Zhao Y, Sun Y, Ding Q. Strain-controlled fatigue behaviors of porous PLA-based scaffolds by 3D-printing technology. J Biomater Sci Polym Ed 2017;28:2196–204.

[39] SAE J1099. Technical Report on Low Cycle Fatigue Properties, Ferrous and Non-Ferrous Materials. Surface vehicle information report. USA: SAE International 2002;4970.

[40] Zhu SP, Lei Q, Wang QY. Mean stress and ratcheting corrections in fatigue life prediction of metals. Fatigue Fract Eng Mater Struct 2017;40:1343–54.

[41] Senatov FS, Niaza K V., Stepashkin AA, Kaloshkin SD. Low-cycle fatigue behavior of 3d-printed PLA-based porous scaffolds. Compos Part B Eng 2016;97:193–200.

[42] Samareh-Mousavi SS, Taheri-Behrooz F. A novel creep-fatigue stiffness degradation model for composite materials. Compos Struct 2020;237:111955.

# Chapter 6      Heat Flux Measurement using 3D-Printed Continuous Wire Polymer Composite Sensors

Fused filament fabrication (FFF) 3D printing was used to fabricate continuous wire polymer composite (CWPC) heat flux sensors; the integrated wires acted as resistive sensing elements. Three different compositions were examined: polylactic acid (PLA) with copper wire (Cu), PLA with nickel (Ni) wire, and thermoplastic polyurethane (TPU) with Cu wire. For each composition, samples with different numbers of layers were 3D printed to investigate the effect of sensor thickness on performance. Baseline thermal calibration of the sensors was conducted to verify a linear relation between the change of temperature and the fractional change of the integrated wires' electrical resistance (temperature coefficient of resistances, α). Performance testing of the 3D-printed CWPC as a heat flux sensor showed promising results for all compositions and demonstrated their ability to be used as heat flux sensors for low temperature and low heat flux applications. Measurement errors were less than 17% for PLA+Cu and TPU+Cu, and less than 12% for PLA+Ni. A case study demonstrates the use of a 3D-printed flexible CWPC heat flux sensor to estimate heat loss from an insulated system with good accuracy. This sensor fabrication approach can potentially be employed in a wide range of applications because it allows for custom geometries and can use different types of polymers and sensing elements.

## 6.1. Introduction

Heat flux measurement at surfaces is important for optimizing thermal systems and monitoring the performance of many engineering applications, including industrial process management, building heat transfer, fire test experiments, and biological systems research [1–4]. In these examples, a heat flux sensor is often considered because it is simple, relatively accurate, and quick to respond [3,5]. Heat flux sensors are generally classified based on three operation methods: transient, active heating, and gradient methods [5–7].

In transient methods, the temperature history is measured, and the heat flux is predicted using inverse heat conduction methods. As such, the main challenge of this method relates to the setup and type of analytical model used to obtain heat flux [5,7]. For active heating methods, the input power required to maintain surface temperature is monitored to calculate the heat transfer coefficient or, inversely, a known input power (heat flux) is applied, and the corresponding surface temperature or gradient temperature within a material is measured to calculate the heat transfer coefficient [5,7].

In the gradient method, a temperature difference is measured across an intermediate layer and the heat flux is calculated based on Fourier's law. In this method, the temperature differences, $\Delta T$, are measured as an input to obtain the heat transfer rates [3,4]. The gradient method has some advantages compared with the other methods, such as potentially short response time and in-situ measurement with the least effect on the thermal gradient of the device [7].

Several gradient-based heat flux sensors depend on the deposition of thin resistance layers on both sides of a plastic layer to work as a resistive temperature detector (RTD) [2]. Andretta et al. [8] used resistive elements to produce a heat flux sensor of two copper coils on each surface of a

plexiglass disc in order to study the effect of solar heat on a natural cooling device. Klems and DiBartolomeo [9] fabricated a heat flux sensor consisting of nickel wire placed on a fiberglass substrate and insulated with phenolic resin to investigate building insulation performance by measuring low non-uniform heat fluxes. Hayashi et al. [10] developed a heat flux sensor consisting of two nickel resistors sputtered on both sides of a silicon monoxide substrate. Epstein et al. [11] produced a gradient-type heat flux sensor of nickel resistors deposited on a polyimide substrate. Azerou et al. [12] produced a heat flux sensor of copper resistors deposited on an epoxy plate.

Recently, additive manufacturing (AM) techniques have been leveraged to fabricate polymer composites because they enable the creation of complex, lightweight structures without requiring moulds, and rapid, iterative, and on-demand alteration of prototype dimensions and geometries [13–15]. AM techniques have evolved to produce functional systems with a high level of complexity and low-cost parts [16]. For example, AM techniques have enabled the direct fabrication of electronic devices such as sensors, field-effect transistors, actuators, and organic light-emitting diodes inside a 3D-printed structure [17]. For instance, Lee et al. [18] fabricated a temperature sensor of gated reduced graphene oxide (rGo)/polyurethane composite using a lithographic technique. However, this is a complex process, and the sensor is costly.

Fused filament fabrication (FFF) is one of the most popular AM techniques because it can be operated using low-cost and open-source hardware and software. In the FFF process, extruded feedstock material is deposited layer by layer through a pre-heated nozzle onto the bed of the 3D-printer. This working principle makes it amenable to printing a wide range of materials and to fabricating polymer composites [19]. For example, commercial filaments from different suppliers (e.g., Robo 3D, SainSmart, and Protopasta) have been developed by mixing the reinforcement with polymeric material to produce filament of polymer composites before the FFF process [13,14].

140

Sajid et al. [17] developed a temperature sensor of polylactic acid (PLA) with graphene nanorods using the FFF technique. Wei et al. [20] fabricated a thermally conductive 3D-printed polymer composite by introducing graphene oxide flakes to acrylonitrile butadiene styrene (ABS).

The electrical resistance of conductive polymer composite is governed by the formation of conductive networks within the polymer matrix. However, if this concentration exceeds a specific limit, the mechanical properties may drop abruptly [21–23]. The main challenge to producing conductive polymer composites is the interface between the matrix and the conductive filler, which should be minimized to improve the thermal and electrical properties [14]. Post-processing, such as hot pressing or sintering at elevated temperatures, can be applied to remove the matrix binder and decrease the interfacial thermal resistance. However, the obtained porous structure has poor mechanical properties [24]. In addition, high filler concentration may aggregate and block the printer nozzle [15]. Another drawback of using discontinuous filler is the counterbalance between the electrical response of the filler and the matrix under heating: Some fillers undergo a reduction of their electrical resistance with increasing temperature, while the matrix tends to expand with temperature, resulting in higher electrical resistance. This competing effect may cause a low or non-linear electrical behavior with temperature [25].

To address the shortcomings of 3D-printed conductive discontinuous polymer composites, 3D printing of conductive continuous polymer composites has been investigated to determine mechanical and thermal properties [13,14,16,26,27]. One technique in particular combined FFF with co-extruded metal wires to create continuous wire polymer composites (CWPCs) [28]. These have since been used as a 3D-printed anti- or de-icing panel where the copper wire serves as a heating element [16] and as 3D-printed strain sensors [26,27].

The objective of the present study is to leverage 3D printing to design and quantify the performance of 3D-printed CWPC heat flux sensors which may be used for bespoke thermal applications. To achieve this, different design parameters, such as matrix material, wire material, and sensor thickness, were investigated to evaluate their effect on the performance and accuracy of the sensor. The 3D-printed CWPC heat flux sensor was then employed in an appropriate case study. Application limitations and design improvements are discussed.

## 6.2.    Experimental Methods

### 6.2.1.    Heat Flux Sample Design

3D-printed CWPC heat flux sensor samples were printed (see Figure 6-1) with nominal dimensions of 55 mm length × 40 mm width (sensing area of $40 \times 40$ mm$^2$ as shown in Figure 6-1b). These were fabricated using a modified 3D printer (Prusa i3 MK2, Prusa Research, Prague, Czech Republic) to allow for the simultaneous co-extrusion of continuous wire with the polymer matrix as described previously in [28, 29]. The printed rasters with integrated wire are unidirectional; as such, the continuous wires form a serpentine circuit at each layer. For the top and bottom layers, the serpentine wire was extended from the start and endpoints of the printed layer serving as one resistive sensing element (only the serpentine circuits at the top and bottom layers serve as resistive sensing elements, as shown in Figure 6-1b and c). The wires were soldered to a thin piece of copper tape which served as electrical terminals for electrical resistance measurements of the sensing layers, as shown in Figure 6-1b. The four-wire method was used to measure the electrical resistance to eliminate the lead wires' resistance by soldering two external copper wires to each electrical terminal.
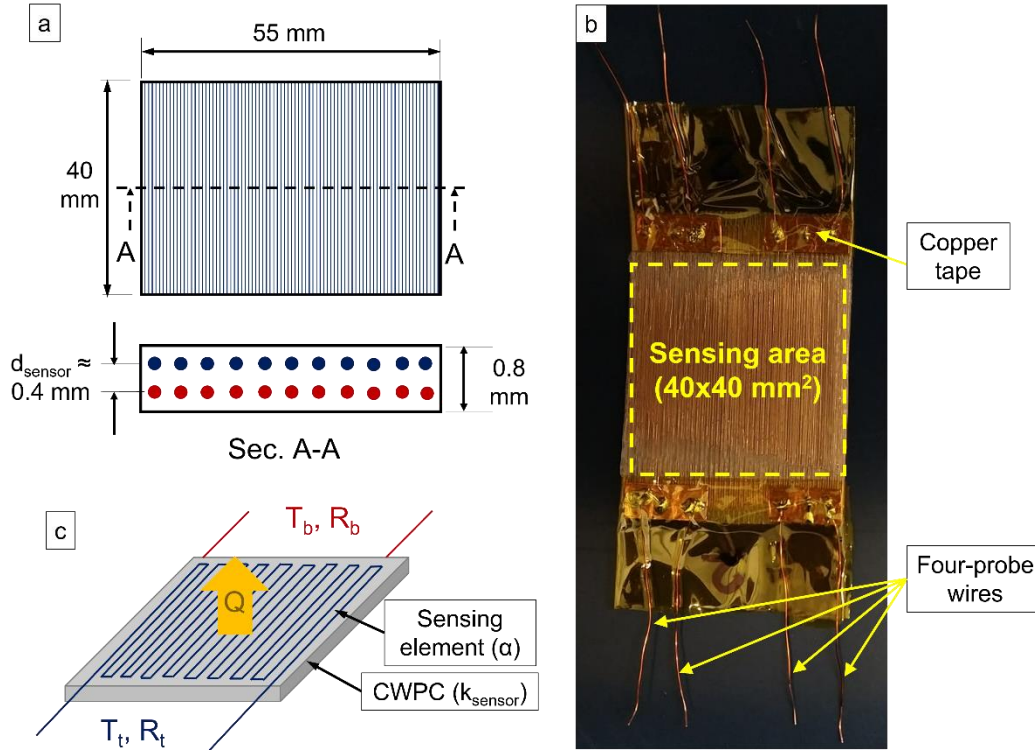
Figure 6-1. Two-layer CWPC heat flux sensor sample, a) schematic of 3D-printed sample with enlarged cross-sectional area (Sec. A-A); b) photograph of 3D-printed sample with electrical connection; c) 3D schematic of CWPC sensor.

The 3D-printed CWPC sensor measures the heat transfer rate through the sensor, $Q_{meas}$, using Fourier's law,

$$Q_{meas} = \frac{k_{sensor} A_{sensor} \Delta T}{d_{sensor}} \tag{6.1}$$

where $k_{sensor}$ is the thermal conductivity of the CWPC sensor, $A_{sesnor}$ is the sensing area of the CWPC (as shown in Figure 6-1b), $d_{sensor}$ is the distance between sensing elements (which varied by the number of printed layers (two-, three-, and four-layers)). $\Delta T$ is the temperature difference between the top layer, $T_t$, and the bottom layer, $T_b$, of sensing elements of the CWPC sensor given by

$$\Delta T = T_t - T_b \tag{6.2-a}$$

$$T_t = \Delta T_t + T_{amb} \tag{6.2-b}$$

$$T_b = \Delta T_b + T_{amb} \tag{6.2-c}$$

where $\Delta T_t$ and $\Delta T_b$ are the change in temperature in both top and bottom layer of the CWPC sensor, respectively. This temperature difference depends on the electrical resistance of the sensing elements in the top layer, $R_t$, and bottom layer, $R_b$, and the temperature coefficient of resistance, $\alpha$, according to

$$\Delta T_t = \frac{(R_t - R)/R}{\alpha} \tag{6.3-a}$$

$$\Delta T_b = \frac{(R_b - R)/R}{\alpha} \tag{6.3-b}$$

where $R$ is the sensing element's electrical resistance at ambient temperature, $T_{amb}$.

Therefore, to obtain a reasonably accurate $Q_{meas}$, accurate knowledge of $k_{sensor}$, $d_{sensor}$, and $\alpha$ are required. With knowledge of these values, $Q_{meas}$ can be obtained as per Equation (6.1) and compared with a known heat flux to evaluate the accuracy of the sensor. The following sections address how each of these parameters were understood and quantified.

### 6.2.2. Sensor Materials

For the polymer matrix, transparent polylactic acid (PLA) (ColorFabb, The Netherlands) and transparent thermoplastic polyurethane (TPU) (Ninjatek, USA) were used. Two types of wires were used as sensing elements of the heat flux sensor: enamelled copper wire (75 µm, Remington Industries, USA) and enamelled nickel wire (75 µm, Magnet Wire and Precision Wire Solutions, USA). Three different material configurations were 3D printed: PLA+Cu, PLA+Ni, TPU+Cu. The Cu and Ni wires were selected because they have a good linear relationship between electrical

resistance and temperature, and they are less costly than platinum wires which are often used as RTDs in heat flux sensors [25]. Rigid PLA and flexible TPU were selected to explore the effect of sensor rigidity and to potentially widen the range of applications for the CWPC heat flux sensor.

Since the wire integrated within the CWPC is not aligned in the direction of heat transfer, it has limited effect on the thermal conductivity of the CWPC in the sensing direction and the $k_{sensor}$ can be assumed to be equal to the thermal conductivity of the base polymer [14]. The values of the thermal conductivity of PLA and TPU were obtained from the literature as 0.13 W/mK [30] and 0.24 W/mK [31], respectively..

### 6.2.3. Microscopic Imaging

To accurately measure the distance between the layers, especially the distance between the wires in each layer where the electrical resistance was measured, $d_{sensor}$, the samples were cross-sectioned and examined using an optical stereomicroscope (LEICA MZ10 F, LEICA, Germany). Firstly, the surface of the sample cross-section was prepared using a grinding and polishing machine (StarGrind™ 200-2V, Microstar 2000, Canada) at 300 rpm rotational speed. The surface was ground using silicon carbide papers of 180, 280, 400, and 600 grit. Then, it was polished using a 1 μm alumina particle suspension. Lastly, the captured images were analyzed using image processing open-source software (ImageJ, National Institutes of Health, Bethesda, Maryland, USA) to measure the value of the $d_{sensor}$ used in Equation (6.1.

### 6.2.4. Temperature Coefficient of Resistance Characterization

The temperature coefficient of resistance, $\alpha$, for these sensors depends on the integrated wire material and was measured for each wire type. Although $\alpha$ is well known for elemental Cu and Ni, it was measured independently for the CWPC sensing elements here because its value may vary slightly depending on the metal alloy used for the wires and the manufacturing or heat treatment

process (e.g., annealing). $\alpha$ was measured by placing the CWPC sensors in a temperature-controlled isothermal chamber. The temperature of the CWPCs was varied from 18°C to 42°C in steps of 4 K and the corresponding electrical resistance of the wires was measured using a digital multimeter (DMM; Agilent 34401A). A Fluke RTD probe (Model 5606) was used to measure the reference temperature. The relation between the fractional change of electrical resistance and the temperature change was plotted for each layer/sensing element. For both Cu and Ni wires, this relation was linear over the temperature range, and the slope of this curve yields the temperature coefficient of the wires, $\alpha$, as

$$\alpha = \frac{(R_i - R)/R}{T_i - T} \tag{6.4}$$

where $R_i$ is the electrical resistance measured at each temperature, $T_i$, and $R$ is the reference electrical resistance at the initial baseline temperature, $T$ (=18°C) [5]. The samples used for this measurement had four layers which contained four separate sensing elements each; these were used to obtain an average value of $\alpha$ and an associated uncertainty.

### 6.2.5.   Heat Flux Characterization

Having established $A_{sensor}$, $k_{sensor}$, $d_{sensor}$, and $\alpha$, electrical resistance measurements can be used to directly quantify heat transfer rate through the CWPC sensor, $Q_{meas}$, using Equation (6.1. the efficacy of the 3D-printed CWPC heat flux sensors was characterized by applying a well-known heat transfer rate, $Q_{applied}$, to the sample using the steady-state guarded heat flux apparatus developed by Elkholy et al. [32] (shown in Figure 6-2).
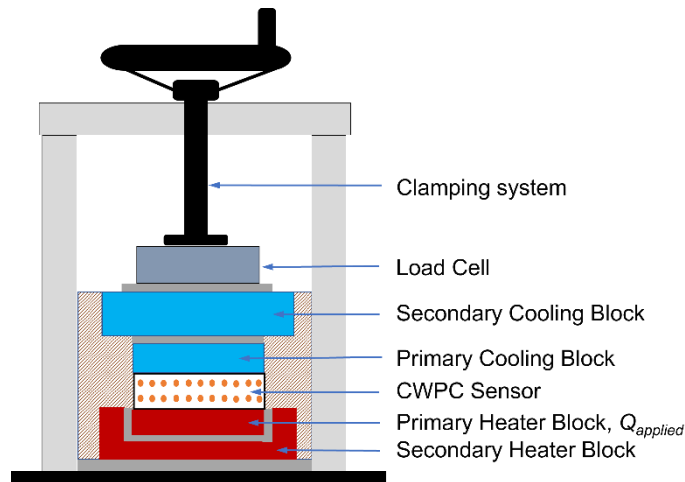
Figure 6-2. Heat flux characterization device.

The CWPC heat flux sensor was sandwiched between the primary heating and cooling blocks. A known electrical power was applied to the primary heater block, $Q_{applied}$, and the cooling blocks were held at a fixed temperature using a recirculating chiller. The temperature of the secondary heater block (guard heater) was controlled such that it was identical to the primary heater block temperature to ensure that all $Q_{applied}$ to the primary heater block flowed through the sample under test. Additional details regarding the design, construction, and uncertainty analysis of this apparatus are described in [32].

Once steady state was achieved, the electrical resistance of the top and bottom elements of the CWPC sensor ($R_t$ and $R_b$, respectively) was measured using the DMM. The electrical resistances of each layer were then used to calculate the corresponding sensing element temperatures, $T_t$ and $T_b$, using the previously measured $\alpha$ and Equations (6.2 and (6.3).

The heat transfer rate through the CWPC sensor, $Q_{meas}$, can then be quantified using Equation (6.1 and compared with $Q_{applied}$ to quantify the accuracy of the CWPC heat flux sensor. The error was calculated as

147

$$\% \ Error = \frac{Q_{meas} - Q_{applied}}{Q_{applied}} * 100 \qquad\qquad (6.5)$$

## 6.3. Results and Discussion

### 6.3.1. Microscopic Imaging

Microstructure images were used to measure the distance between the sensing elements, $d_{sensor}$, for each of the 3D-printed CWPC sensor samples. The distance was calculated based on the relative spacing of the wires within the layers, as seen in Figure 6-3. Approximately 88 measurements across the whole width of the sample were obtained and averaged to obtain $d_{sensor}$. The uncertainty was estimated as two standard deviations. Table 6-1 summarizes $d_{sensor}$ values for the CWPC samples. For all CWPC compositions, the relative positional uncertainty of $d_{sensor}$ decreased with sample thickness; however, thicker sensors have higher thermal resistance, and therefore these influenced the heat transfer rate of the system to a greater degree.
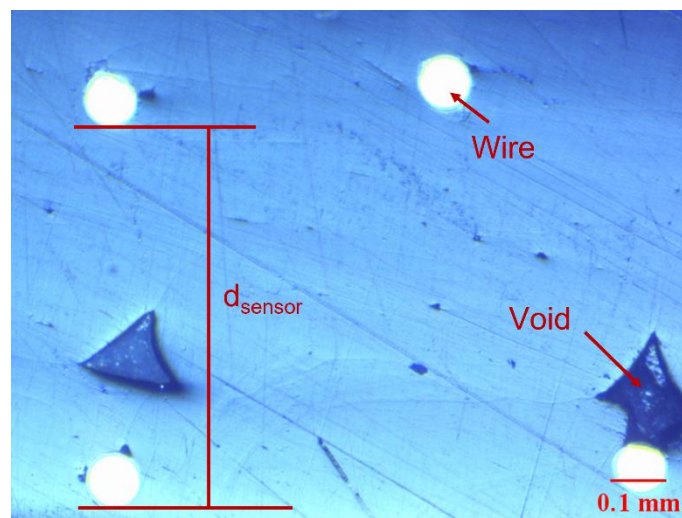


Figure 6-3. Example of cross-section microscopy of 3D-printed CWPC.

Table 6-1. Average distance between sensing elements for two-, three-, and four-layers samples of PLA+Cu, PLA+Ni, and TPU+Cu.

| | Average distance between sensing elements, $d_{sensor}$ (mm) | | |
|---|---|---|---|
| Samples | PLA+Cu | PLA+Ni | TPU+Cu |
| Two layers | $0.394 \pm 0.045$ ($\pm 11.29\%$) | $0.398 \pm 0.042$ ($\pm 10.43\%$) | $0.33 \pm 0.044$ ($\pm 12.58\%$) |
| Three layers | $0.665 \pm 0.045$ ($\pm 6.73\%$) | $0.804 \pm 0.04$ ($\pm 4.94\%$) | $0.79 \pm 0.039$ ($\pm 5.03\%$) |
| Four layers | $0.993 \pm 0.037$ ($\pm 3.74\%$) | $1.128 \pm 0.037$ ($\pm 3.3\%$) | $1.068 \pm 0.036$ ($\pm 3.48\%$) |

## 6.3.2. Temperature Coefficient of Resistance Characterization

The type of wire integrated within the 3D-printed CWPC sensor dictates the electrical response under different temperatures according to its temperature coefficient of resistance, α. Figure 6-4 shows the corresponding fractional change of electrical resistance of the wire integrated into the CWPCs as a function of the change of temperature applied. In this temperature range, the relationship is very linear for both the 3D-printed PLA+Cu sample and the PLA+Ni sample. The temperature coefficient of resistance, $α$, comes from the slope of these curves as determined from Equation (6.4). $α$ was evaluated as $0.4072 \times 10^{-2}$ K$^{-1}$ for PLA+Cu and $0.5269 \times 10^{-2}$ K$^{-1}$ for PLA+Ni. The PLA+Ni sample has a higher $α$ compared with the PLA+Cu sample because Ni has higher $α$ than Cu. Overall, the $α$ values are consistent Cu and Ni wire properties found in other studies [33,34].

To estimate its uncertainty, $α$ was measured for every layer in the four-layer samples for both PLA+Cu and PLA+Ni CWPC sensors, as summarized Table 6-2. The values were relatively consistent, and two standard deviations were used as an estimate of uncertainty.
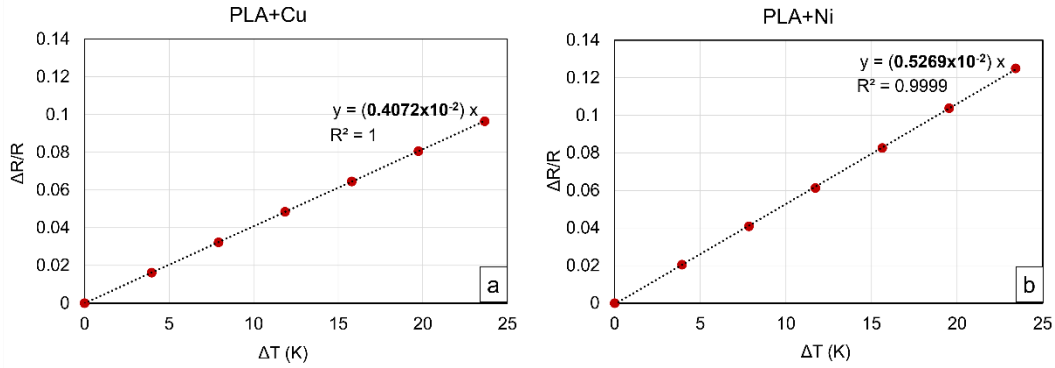
Figure 6-4. Example showing relation between the change of temperature for the wire electrical resistance of a) PLA+Cu; b) PLA+Ni.

Table 6-2. The temperature coefficient of resistance for each layer of 3D-printed CWPC.

|  | $\alpha$ for PLA+Cu ($K^{-1}$) | $\alpha$ for PLA+Ni ($K^{-1}$) |
|---|---|---|
| 1st layer | $0.4080 \times 10^{-2}$ | $0.5263 \times 10^{-2}$ |
| 2nd layer | $0.4072 \times 10^{-2}$ | $0.5256 \times 10^{-2}$ |
| 3rd layer | $0.4061 \times 10^{-2}$ | $0.5287 \times 10^{-2}$ |
| 4th layer | $0.4075 \times 10^{-2}$ | $0.5269 \times 10^{-2}$ |
| Average ± uncertainty (± %) | $0.4072 \times 10^{-2} \pm 0.8164 \times 10^{-5}$ (±0.20%) | $0.5269 \times 10^{-2} \pm 1.328 \times 10^{-5}$ (±0.25%) |

### 6.3.3. Uncertainty Analysis and Heat Flux Characterization

The uncertainty of the measured parameters of the CWPC heat flux sensor ($k_{sensor}$, $A_{sensor}$, $d_{sensor}$, $\alpha$, $R$) are summarized in Table 6-3. The uncertainty of $k_{sensor}$ was estimated as ±4% based on the variations of the values of thermal conductivities of 3D-printed material reported in different studies [14,32]. The uncertainty of the change in the temperature, $\Delta T$, within each layer was determined based on the uncertainties of the electrical resistance and $\alpha$ readings (Equation 5). The uncertainty of the electrical resistance measurements was the main contributor to the uncertainty of $\Delta T$ due to the low value of the uncertainty of $\alpha$, as shown in Table 6-3.

Table 6-3. Summary of uncertainties of measured parameters.

| Parameter | Uncertainty | | |
|---|---|---|---|
| $k_{sensor}$ (W/mK) | PLA+Cu | | $\pm$ 0.0052 |
| | PLA+Ni | | $\pm$ 0.0052 |
| | TPU+Cu | | $\pm$ 0.0096 |
| $A_{sensor}$ (mm$^2$) | $\pm$ 0.1063 | | |
| $R$ ($\Omega$) | $\pm$ (0.01% of reading + 0.004) | | |
| $\alpha$ (K$^{-1}$) | PLA+Cu | | $\pm$ 0.8164x10$^{-5}$ |
| | PLA+Ni | | $\pm$ 1.328x10$^{-5}$ |
| | TPU+Cu | | $\pm$ 0.8164x10$^{-5}$ |
| $d_{sensor}$ (mm) | PLA+Cu | 2 layers | $\pm$ 0.045 |
| | | 3 layers | $\pm$ 0.045 |
| | | 4 layers | $\pm$ 0.037 |
| | PLA+Ni | 2 layers | $\pm$ 0.042 |
| | | 3 layers | $\pm$ 0.04 |
| | | 4 layers | $\pm$ 0.037 |
| | TPU+Cu | 2 layers | $\pm$ 0.044 |
| | | 3 layers | $\pm$ 0.039 |
| | | 4 layers | $\pm$ 0.036 |

Having established the uncertainty of each design parameter associated with the CWPC heat flux sensor, the overall uncertainty in $Q_{meas}$ can be estimated using the error propagation method developed by Kline and McClintock [35] according to

$$\frac{\omega_Z}{Z} = \left[\sum_{i=1}^{n} \left(\frac{\omega_{x_i}}{x_i}\right)^2\right]^{1/2} \tag{6.6}$$

where Z is the resulting quantity, $\omega_Z$ is its uncertainty, $n$ is the number of independent variables, $x_i$ are the independent variables, and $\omega_{x_i}$ are their uncertainties.

The power applied, $Q_{applied}$, to the 3D-printed CWPCs and the calculated $Q_{meas}$ based on electrical resistance readings of the CWPCs were compared and plotted for each configuration of 3D-printed CWPC sensor (Figure 6-5). The value of the error between $Q_{applied}$ and $Q_{meas}$ was calculated as per Equation (6.5 for all configurations to estimate the error lines (plotted in Figure 6-5).

The error ranged from 9.27% to 16.92%, from 2.17% to 11.41%, and from 4.44% to 14.96% for PLA+Cu, PLA+Ni, and TPU+Cu, respectively. Generally, measurement errors were less than 17% for PLA+Cu and TPU+Cu, and less than 12% for PLA+Ni and these results were comparable to the results reported in previous studies, where the error between the theoretical and experimental data was found to be 24% in the study conducted by Jasperson et al. [5] and 11.5% in the study conducted by Gifford et al. [36]. The error in the case of PLA+Ni for all numbers of layers (Figure 6-5b) is smaller than that of PLA+Cu and TPU+Cu (Figure 6-5a and c). This can be attributed to the higher $\alpha$ of the Ni wire compared with Cu wire as presented in Section 6.3.2. Overall $Q_{meas}$ agrees with $Q_{applied}$ within experimental uncertainty and the discrepancies in $Q_{meas}$ are attributed to the uncertainties in the sensor's governing parameters ($k_{sensor}$, $A_{sensor}$, $d_{sensor}$, $\Delta T$).
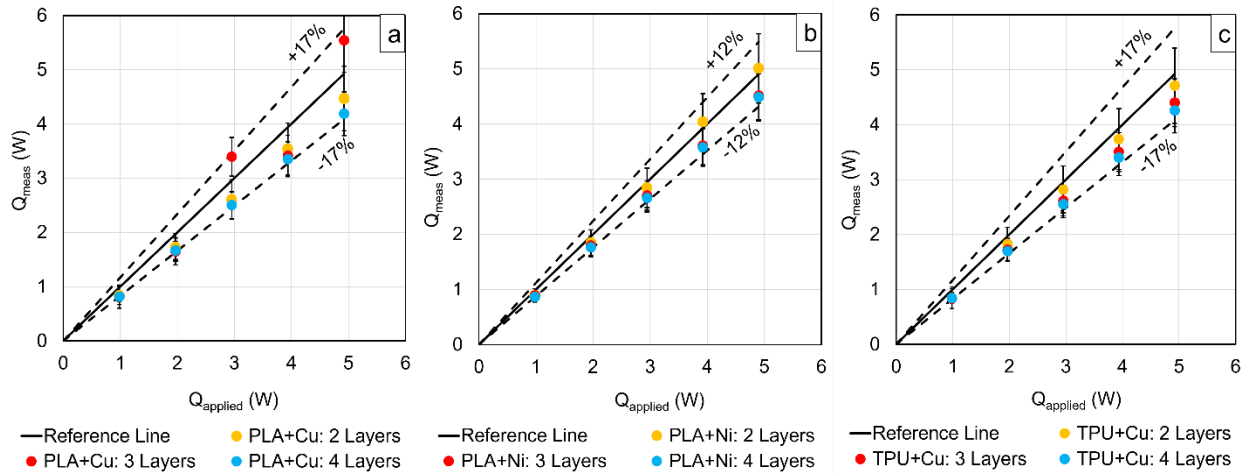


Figure 6-5. Error between $Q_{applied}$ and $Q_{meas}$ for different number of layers of a) PLA+Cu; b) PLA+Ni; c) TPU+Cu.

To understand how the individual parameter uncertainties contribute to the uncertainty of $Q_{meas}$, their percentages were compared (Figure 6-6) with heat transfer rate for the different 3D-printed CWPC sensor compositions. Here, $A_{sensor}$, $d_{sensor}$, and $k_{sensor}$ do not vary with heat flux and depend

strictly on sensor design and materials. The thicker sensors have lower uncertainty but have higher thermal resistance. This is partly due to less relative uncertainty in $d_{sensor}$ and partly the larger $\Delta T$ between the sensing circuits (and lower relative uncertainty) for a given heat flux. Finally, Figure 6-6 illustrates that the uncertainties of $\Delta T$ for the PLA+Ni sensors are lower than those of the PLA+Cu and TPU+Cu sensors due the higher $\alpha$ (or temperature sensitivity) of the nickel wire compared with copper, as discussed previously.



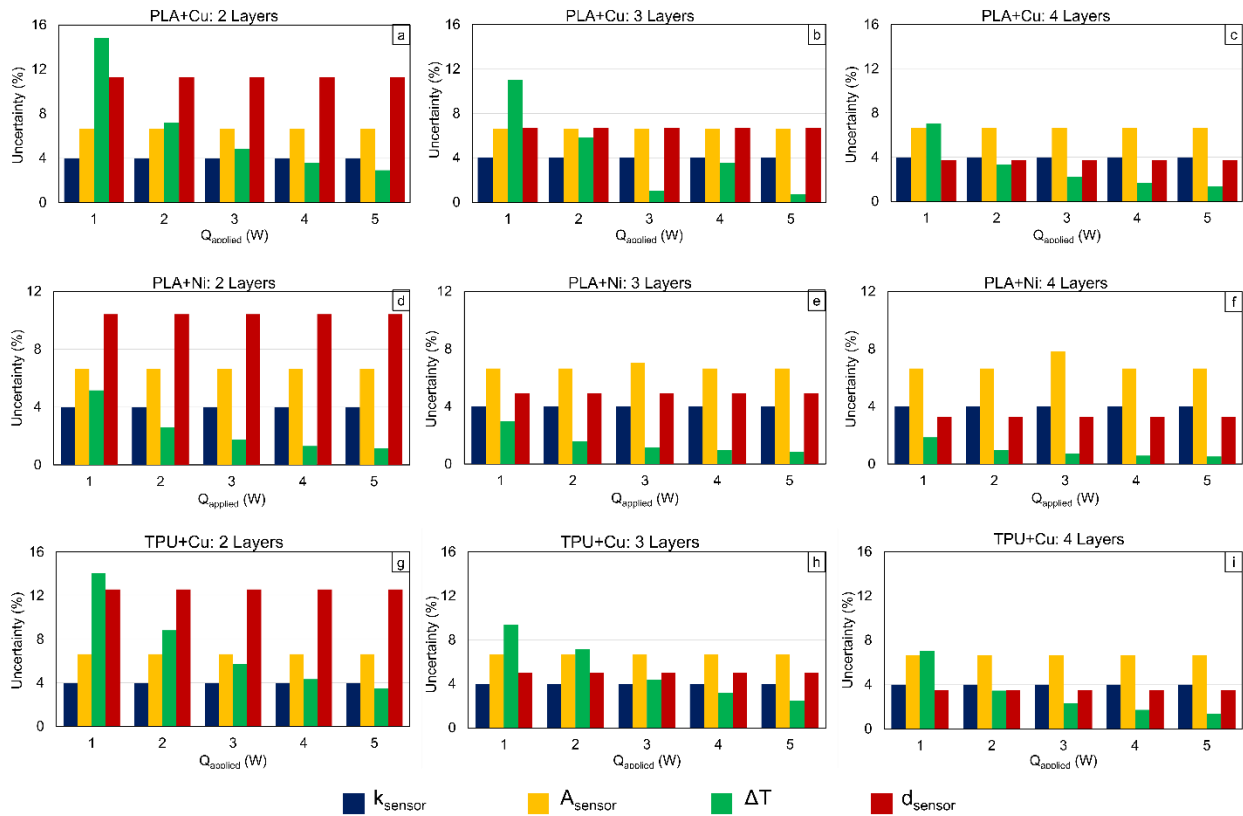Figure 6-6. Uncertainty percentage of Fourier's law parameters for different number of layers at different Qapplied for a) PLA+Cu: 2 layers; b) PLA+Cu: 3 layers; c) PLA+Cu: 4 layers; d) PLA+Ni: 2 layers; e) PLA+Ni: 3 layers; f) PLA+Ni: 4 layers; g) TPU+Cu: 2 layers; h) TPU+Cu: 3 layers; c) TPU+Cu: 4 layers.

It is important to recognize that the fabrication method and materials used for these 3D-printed CWPC heat flux sensors result in inherent limitations such as a relatively high thermal resistance (owing to thickness and polymer conductivity) and relatively low temperature limits. However, the design flexibility can make these sensors suitable for a variety of low-temperature and low-heat flux applications such as biomedical, building, and lab-scale applications. Moreover, the manufacturing technique allows for the fabrication of both rigid and flexible sensors. This flexibility (both in terms of material and design) are illustrated in the following section in the context of a case study. Moreover, this FFF CWPC heat flux sensor can not only be used to measure heat flux through a specific area like most of the commercial and studied heat flux sensors [2,8–12], but it can also be used to obtain the heat flux characterization of the whole structure by 3D printing of a functional part. Thermal sensors account for 70–80% of the global sensor market [37] and FFF of functional CWPC sensors can further contribute to this growth.

## 6.4. Application Case Study

### 6.4.1. Alternative CWPC Heat Flux Sensor Configurations

The planar 3D-printed CWPC configuration demonstrated in the previous sections can be extended to 3D print more complex 3D structures which can simultaneously serve as functional components (e.g., enclosures) and as heat flux sensors for low-temperature and low-heat flux applications. Different shapes with different sizes were 3D printed, as shown in Figure 6-7. For example, a cylindrical shape (Figure 6-7a) may be applied to the outer surface of an insulated piping system to estimate energy losses. CWPC heat flux sensors can also be printed as rectangular enclosures such as those with a square cross-section as shown in Figure 6-7b. In laboratory heat transfer experiments, it is often necessary to fabricate bespoke and complex-shaped insulative enclosures to mitigate heat loss from insulated components such as heaters (e.g., at the evaporator section of

154

thermosyphons [38,39], heated test sections [40,41], or in heat flux meter bar applications [42]). The 3D-printed CWPC heat flux sensor demonstrated here could be leveraged and incorporated into these enclosures to simultaneously insulate and estimate heat loss in these applications.
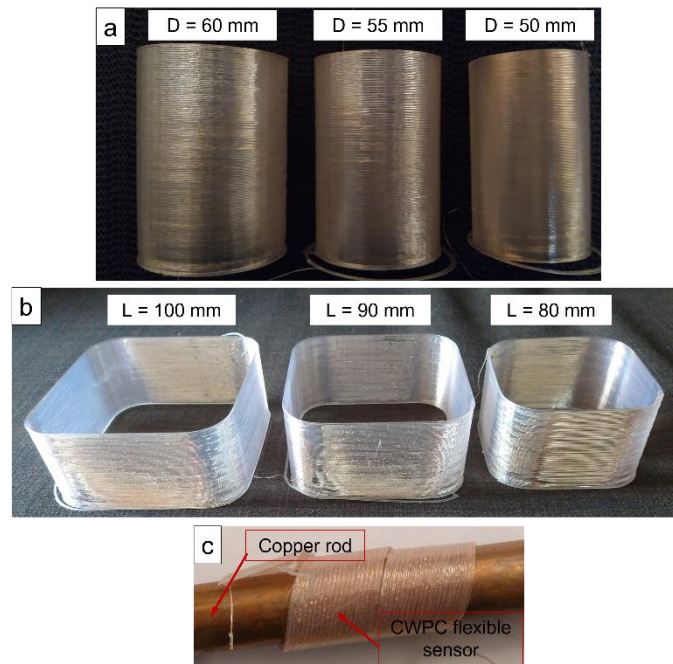


Figure 6-7. Different 3D-printed functional structures for heat flux sensor, a) hollow cylinders; b) square cross-section container; c) flexible strip.

Alternatively, this FFF CWPC fabrication approach can also be used to 3D-print flexible heat flux sensors which can be designed fit a wide range of applications. For example, a two-layer flexible strip of TPU+Cu (characterized in a planar configuration in Figure 6-5c above) was unidirectionally 3D printed at $0°$ and wrapped around a cylinder, as shown in Figure 6-7c. Compared with commercial heat flux sensors, these structures have the advantage of being custom designed, sized, and 3D-printed to suit a given application.

### 6.4.2.    Flexible CWPC Heat Flux Sensor Case Study

To demonstrate the functionality of the flexible heat flux sensor, an experimental setup was designed and constructed to imitate usage in a heat-loss estimation scenario (e.g., on the external surface of an insulated process pipe containing a hot fluid). The flexible TPU+Cu CWPC heat flux sensor designed for this case study is shown in Figure 6-8. Here, the 3D-printed sensor consisted of two layers with integrated unidirectional wire, such that at each layer the continuous wires formed a serpentine circuit that worked as a sensing element. For each layer, the serpentine wire was extended from the start and endpoints of the printed layer acting as one resistive sensing element. The sensor was prepared for the electrical connection measurements as described in Section 6.2.1.
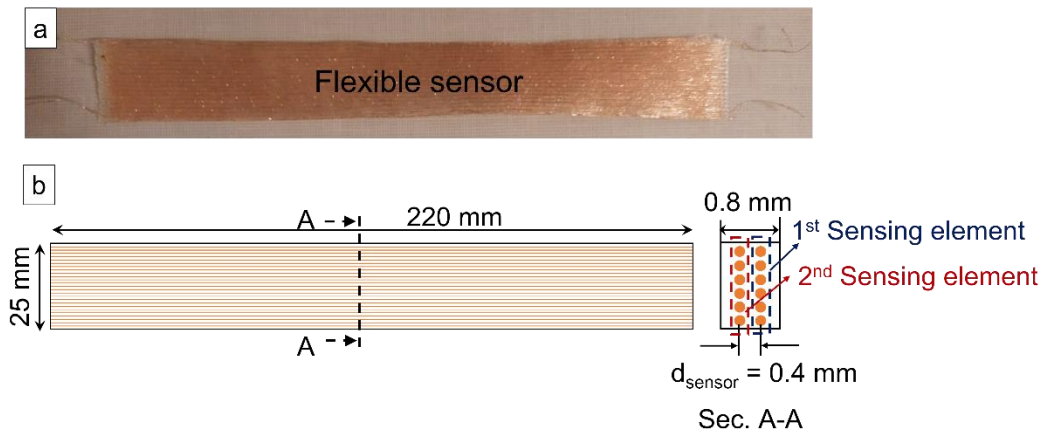


Figure 6-8. TPU+Cu CWPC flexible sensor, a) photo of the sensor; b) enlarged schematic of the sensor with dimensions and cross-section.

A schematic of the experimental setup for this case study is shown in Figure 6-9. A heated aluminum rod 25.4 mm (1 inch) in diameter, $D_{rod}$, and 101.6 mm (4 inches) long, $L_{rod}$, simulates a section of a hot pipe in a larger piping system. The rod was heated with a 4.76 mm diameter x 101.6 mm long (0.1875 x 4 inch) cartridge heater (McMaster-Carr, USA) inserted in a hole at the

rod center. Power was supplied and measured using a DC power supply (Aim-TTi, CPX400DP). The heated rod was instrumented with a 1.5 mm T-type thermocouple to a depth of 15 mm to record the rod temperature, $T_{rod}$. The ambient air temperature, $T_{amb}$, was measured with another 1.5 mm T-type thermocouple.

The aluminum rod was insulated using 1.15 mm of ceramic fiber (McMaster-Carr) which has a thermal conductivity, $k_{ins}$, of 0.05 W/mK to minimize circumferential heat loss, as would be the case in a real piping system. The outer surface area of the insulation was 8841 mm$^2$. The ends of the aluminum rod were insulated using a much thicker (10 mm) and more effective aerogel blanket (Aspen Aerogel Spaceloft) with thermal conductivity of 0.014 W/mK. This ensures that the electric input power dissipated circumferentially as much as possible. The CWPC sensor was installed and wrapped around the insulated rod, as shown in Figure 6-10, covering approximately 63% of the exposed area.
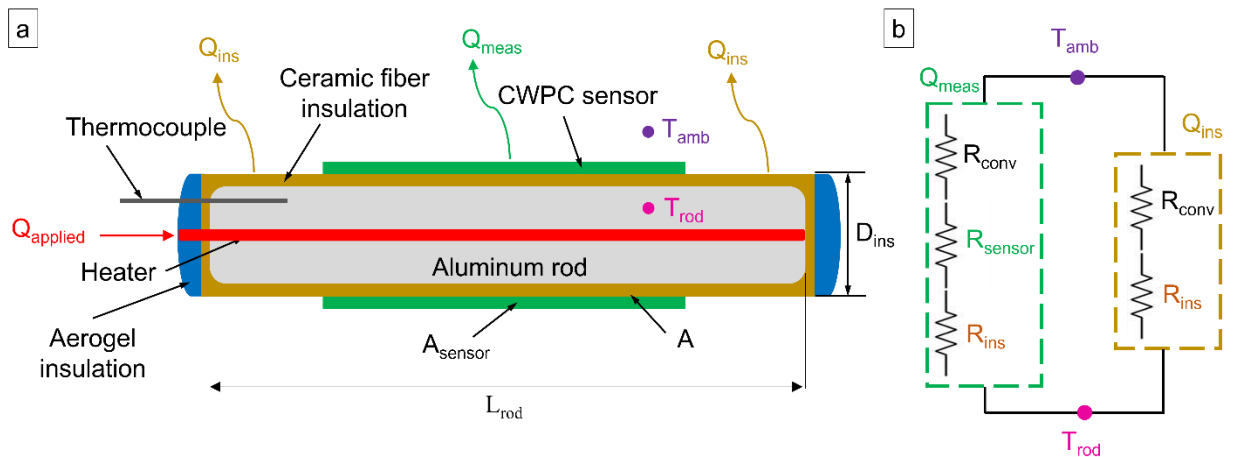


Figure 6-9. a) Cross-section schematic of the flexible CWPC sensor applied to a cylindrical thermal system (e.g., heat loss from a piping system), b) Corresponding thermal resistance network.

157
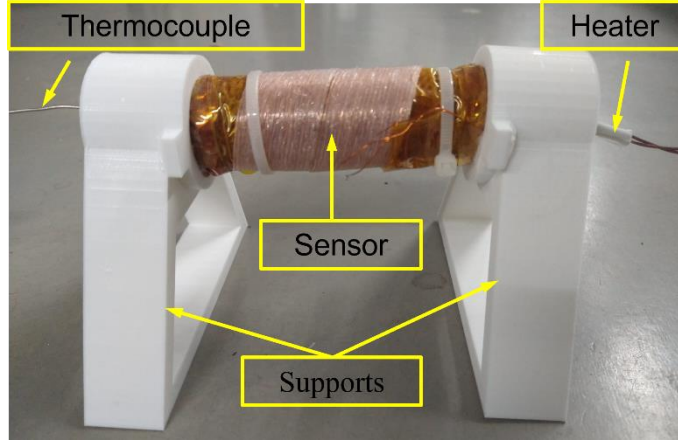
Figure 6-10. Experimental setup of radial CWPC sensor.

In this example, the thickness of the CWPC sensor is very small compared with the diameter of the aluminum rod, $D_{rod}$; therefore, the functionality of the system can be validated using the planar formulation for the heat flux calculations as described in Section 6.2.1.

To ensure that the CWPC sensor does not overly influence the heat flow of the thermal system (i.e., the heat flux through the sensor is approximately the same as the heat flux through the portion of the insulation not covered by the sensor) the thermal resistance of the sensor was estimated and compared to the estimated thermal resistance of the whole system. The specific thermal resistance of each component of the system was calculated as

$$R_{sensor}A_{sensor} = \frac{t_{sensor}}{k_{sensor}}$$

(6.7-a)

$$R_{ins}A_{sensor} = \frac{t_{ins}}{k_{ins}}$$

(6.8-b)

$$R_{conv}A_{sensor} = \frac{1}{h}$$

(6.9-c)

where $t_{sensor}$ is the thickness of the 3D-printed CWPC flexible sensor, $t_{ins}$ is the thickness of the insulation material, and $h$ is the convective heat transfer coefficient which was assumed to be 10 W/m$^2$K for this case study [43].

Figure 6-11 summarizes the estimated values of thermal resistance for each component in the system and shows that the sensor represents a very small thermal resistance compared with the total system resistance (3.7% of the total RA). This validates the assumption of uniform heat flux for this application.



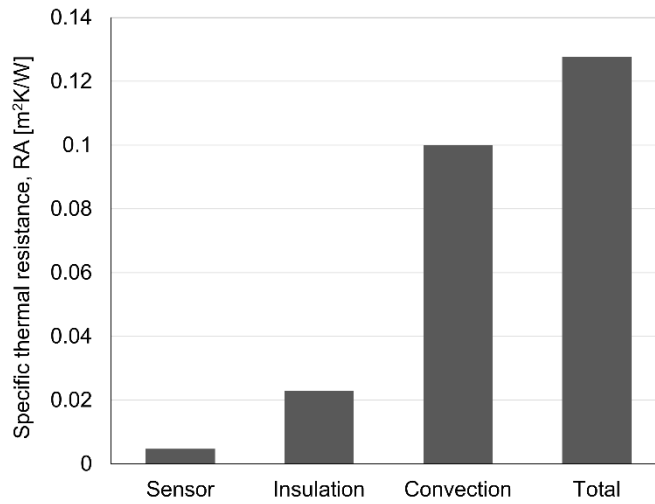Figure 6-11. Thermal resistance of each component of the prototype system.

To validate the functionality of the flexible 3D-printed CWPC heat flux sensor for this type of application, the heat flux measured by the sensor was compared to the theoretical heat flux being dissipated by the system. The heat flux measured by the sensor, $q_{meas}$, is given by

$$q_{meas} = \frac{Q_{meas}}{A_{sensor}} \tag{6.8-a}$$

where $Q_{meas}$ is the heat transfer rate through the sensor measured from Equation (6.1 as described in Section 6.2.1, $A_{sensor}$ is the surface area of the 3D-printed CWPC sensor (220 mm x 25 mm). This was compared to the theoretical heat flux, $q_{applied}$, given by

$$q_{applied} = \frac{Q_{applied}}{A} \qquad \text{(6.8-b)}$$

where $Q_{applied}$ is the electrical power to the heater and $A$ is the outer surface area of the insulation given by

$$A = \pi D_{ins} L_{rod} \qquad \text{(6.9)}$$

where $D_{ins}$ and $L_{rod}$ are defined in Figure 6-9.

The heat flux measured by the CWPC sensor, and the theoretical applied heat flux are shown in Figure 6-12. Generally, agreement between $q_{applied}$ and $q_{meas}$ is reasonably good and within the measurement uncertainty of the sensor. The agreement improves and the relative uncertainty of $q_{meas}$ decreases at higher heat fluxes due to the larger temperature difference within the sensor, as discussed previously.
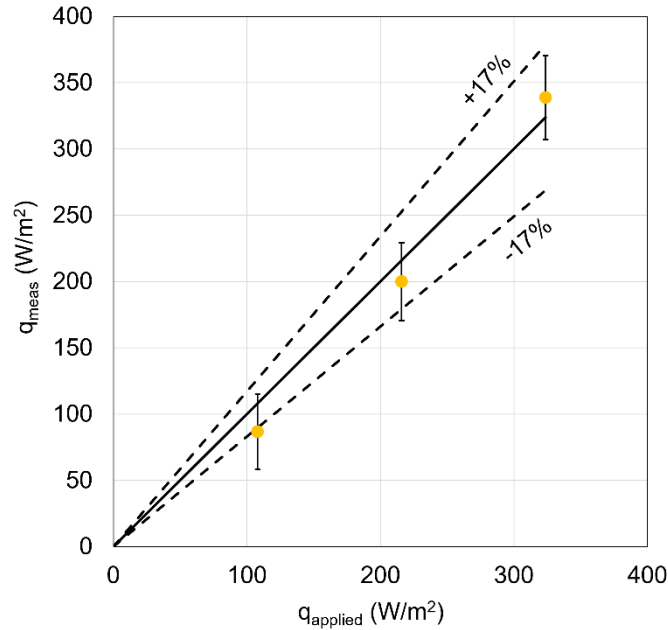
Figure 6-12. Error between $q_{applied}$ and $q_r$ for two layers TPU+Cu flexible strip.

Again, the main disadvantage of these 3D-printed CWPC heat flux sensors is their relatively high thermal resistance due to their low thermal conductivity and relative thickness. As such, their use is limited to scenarios where one wishes to minimize heat transfer but still quantify it (such as this heat-loss estimation case study). Moreover, in many instances the sensor may not fully encompass the area of interest; rather, the sensor is only applied to a portion of the area of interest (as is the case in the present case study). Therefore, the thermal resistance of the sensor itself must be relatively small compared with the thermal resistance of the rest of the system.

## 6.5. Summary and Conclusions

3D-printed continuous wire polymer composites were used to fabricate gradient-type heat flux sensors whose integrated wires served as resistive temperature detectors. Combinations of PLA+Cu, PLA+Ni, and TPU+Cu were fabricated in two-, three-, and four-layer configurations.

Important design parameters which govern the performance and accuracy of the heat flux measurement were quantified. The sensors were verified by imposing a known heat flux and comparing it to the measured heat flux. Overall agreement was good: the measured heat flux agreed within experimental uncertainty. Measurement errors were less than 17% for PLA+Cu and TPU+Cu, and less than 12% for PLA+Ni.

An uncertainty analysis showed that increased sensor thickness lowered the uncertainty of the measured heat flux, but at the expense of having a more resistive sensor. The sensor using the Ni wire showed better sensitivity owing to the higher α of this wire. Overall, the sensors showed reasonable performance for low-temperature, low-heat flux applications and are mainly advantageous because they can be customized to suit a given geometrical application.

A case study was conducted in which a flexible TPU+Cu sensor was fabricated and wrapped around an insulated heated rod to simulate the measurement of heat loss from an insulated pipe. This study predicted the theoretical heat loss with good agreement.

## 6.6. References

[1]    I. Mohammed, A.R.A. Talib, M.T.H. Sultan, S. Saadon, Temperature and heat flux measurement techniques for aeroengine fire test: A review, IOP Conf. Ser. Mater. Sci. Eng. 152 (2016). https://doi.org/10.1088/1757-899X/152/1/012036.

[2]    J. Ewing, A. Gifford, D. Hubble, P. Vlachos, A. Wicks, T. Diller, A direct-measurement thin-film heat flux sensor array, Meas. Sci. Technol. 21 (2010). https://doi.org/10.1088/0957-0233/21/10/105201.

[3]    A. Zribi, M. Barthès, S. Bégot, F. Lanzetta, J.Y. Rauch, V. Moutarlier, Design, fabrication and characterization of thin film resistances for heat flux sensing application, Sensors

Actuators, A Phys. 245 (2016) 26–39. https://doi.org/10.1016/j.sna.2016.04.040.

[4]     A. Jadhav, R. Peetala, V. Kulkarni, Multi-walled carbon nano-tubes for performance enhancement of thin film heat flux sensors, Heat Mass Transf. Und Stoffuebertragung. 56 (2020) 1537–1549. https://doi.org/10.1007/s00231-019-02765-0.

[5]     B.A. Jasperson, J. Schmale, W. Qu, F.E. Pfefferkorn, K.T. Turner, Thin film heat flux sensors fabricated on copper substrates for thermal measurements in microfluidic environments, J. Micromechanics Microengineering. 24 (2014). https://doi.org/10.1088/0960-1317/24/12/125018.

[6]     N.R. Nagaiah, J.S. Kapat, L. An, L. Chow, Novel polymer derived ceramic-high temperature heat flux sensor for gas turbine environment, J. Phys. Conf. Ser. 34 (2006) 458–463. https://doi.org/10.1088/1742-6596/34/1/075.

[7]     B.A. Jasperson, F.E. Pfefferkorn, W. Qu, K.T. Turner, A Thin-Film Heat Flux Sensor Fabricated on Copper for Heat Transfer Measurements in Parallel Channel Heat Sinks, (2010) 437–444.

[8]     A. Andretta, B. Bartoli, B. Coluzzi, V. Cuomo, S. De Stefano, Simple heat flux meter, Rev. Sci. Instrum. 233 (1998) 10–12. https://doi.org/10.1063/1.1136578.

[9]     J. H. Klems, D. DiBartolomeo, Large-area, high-sensitivity heat-flow sensor, Rev. Sci. Instrum. 1609 (2019) 1–5. https://doi.org/10.1063/1.1136847.

[10]    M. Hayashi, S. Aso, A. Tan, Fluctuation of Heat Transfer in Shock Wave/Turbulent Boundary-Layer Interaction, AIAA Journal 27 (1989) 399–404. https://doi.org/10.2514/3.10126.

[11]  A. H. Epstein, G. R. Guenette, High-frequency response heat-flux gauge, Rev. Sci. Instrum. 57 (1986) 639–649. https://doi.org/10.1063/1.1138882.

[12]  O. Access, Thin film heat flux sensors for accurate transient and unidirectional heat transfer analysis, J. Phys. Conf. Ser. 395 (2012) 012084. https://doi.org/10.1088/1742-6596/395/1/012084.

[13]  Y. Ibrahim, A. Elkholy, J.S. Schofield, G.W. Melenka, R. Kempers, Effective thermal conductivity of 3D-printed continuous fiber polymer composites, Adv. Manuf. Polym. Compos. Sci. 6 (2020) 17–28. https://doi.org/10.1080/20550340.2019.1710023.

[14]  Y. Ibrahim, R. Kempers, Effective thermal conductivity of 3D-printed continuous wire polymer composites, Prog. Addit. Manuf. V (2022). https://doi.org/10.1007/s40964-021-00256-5.

[15]  U. Kalsoom, A. Peristyy, P.N. Nesterenko, B. Paull, A 3D printable diamond polymer composite: A novel material for fabrication of low cost thermally conducting devices, RSC Adv. 6 (2016) 38140–38147. https://doi.org/10.1039/c6ra05261d.

[16]  Y. Ibrahim, R. Kempers, A. Amirfazli, Cold Regions Science and Technology 3D printed electro-thermal anti- or de-icing system for composite panels, Cold Reg. Sci. Technol. 166 (2019) 102844. https://doi.org/10.1016/j.coldregions.2019.102844.

[17]  M. Sajid, J.Z. Gul, S.W. Kim, H.B. Kim, K.H. Na, K.H. Choi, Development of 3D-printed embedded temperature sensor for both terrestrial and aquatic environmental monitoring robots, 3D Print. Addit. Manuf. 5 (2018) 160–169. https://doi.org/10.1089/3dp.2017.0092.

[18]  H. Lee, T. K. Choi, Y. B. Lee, H. R. Cho, R. Ghaffari, L. Wang, H. J. Choi, T. D. Chung, N. Lu, T. Hyeon, S. H. Choi, D. Kim, A graphene-based electrochemical device with

thermoresponsive microneedles for diabetes monitoring and therapy, Nat. Nanotechnol 11 (2016) 566–572. https://doi.org/10.1038/nnano.2016.38.

[19]     M. Nikzad, S.H. Masood, I. Sbarski, Thermo-mechanical properties of a highly filled polymeric composites for Fused Deposition Modeling, Mater. Des. 32 (2011) 3448–3456. https://doi.org/10.1016/j.matdes.2011.01.056.

[20]     X. Wei, D. Li, W. Jiang, Z. Gu, X. Wang, Z. Zhang, 3D Printable Graphene Composite, Nat. Publ. Gr. (2015) 1–7. https://doi.org/10.1038/srep11181.

[21]     J. Chen, Y. Zhu, Z. Guo, A.G. Nasibulin, Recent progress on thermo-electrical properties of conductive polymer composites and their application in temperature sensors, Eng. Sci. 12 (2020) 13–22. https://doi.org/10.30919/es8d1129.

[22]     J. Chen, Y. Zhu, J. Huang, J. Zhang, D. Pan, J. Zhou, J.E. Ryu, A. Umar, Z. Guo, Advances in Responsively Conductive Polymer Composites and Sensing Applications, Polym. Rev. 61 (2021) 157–193. https://doi.org/10.1080/15583724.2020.1734818.

[23]     S.H. Masood, W.Q. Song, Development of new metal/polymer materials for rapid tooling using Fused deposition modelling, Mater. Des. (2004). https://doi.org/10.1016/j.matdes.2004.02.009.

[24]     N.D. Ebrahimi, Y.S. Ju, Thermal conductivity of sintered copper samples prepared using 3D printing-compatible polymer composite filaments, 24 (2018) 479–485. https://doi.org/10.1016/j.addma.2018.10.025.

[25]     L. Dan, A.L. Elias, Flexible and stretchable temperature sensors fabricated using solution-processable conductive polymer composites, Adv. Healthc. Mater. 9 (2020) 2000380. https://doi.org/10.1002/adhm.202000380.

[26]   M.A. Saleh, R. Kempers, G.W. Melenka, A comparative study on the electromechanical properties of 3D-Printed rigid and flexible continuous wire polymer composites for structural health monitoring, Sensors Actuators, A Phys. 328 (2021) 112764. https://doi.org/10.1016/j.sna.2021.112764.

[27]   M.A. Saleh, R. Kempers, G.W. Melenka, 3D printed continuous wire polymer composites strain sensors for structural health monitoring, Smart Mater. Struct. 28 (2019) 105041. https://doi.org/10.1088/1361-665x/aafdef.

[28]   Y. Ibrahim, G.W. Melenka, R. Kempers, Fabrication and tensile testing of 3D printed continuous wire polymer composites, Rapid Prototyp. J. 24 (2018) 1131–1141. https://doi.org/10.1108/RPJ-11-2017-0222.

[29]   M.A. Saleh, R. Kempers, G.W. Melenka, Fatigue behavior and electromechanical properties of additively manufactured continuous wire polymer composites for structural health monitoring, FFEMS (2022) 2630–2645. https://doi.org/10.1111/ffe.13778.

[30]   O. Zmeskal, L. Marackova, T. Lapcikova, P. Mencik, and R. Prikryl, Thermal properties of samples prepared from polylactic acid by 3D printing, AIP Conf. Proc. 2305 (2020) 020022. https://doi.org/10.1063/5.0033857.

[31]   J. Liu, W. Li, Y. Guo, H. Zhang, Z. Zhang, Improved thermal conductivity of thermoplastic polyurethane via aligned boron nitride platelets assisted by 3D printing, Compos. Part A. 120 (2019) 140–146. https://doi.org/10.1016/j.compositesa.2019.02.026.

[32]   A. Elkholy, R. Kempers, An accurate steady-state approach for characterizing the thermal conductivity of Additively manufactured polymer composites, Case Stud. Therm. Eng. 31 (2022). https://doi.org/10.1016/j.csite.2022.101829.

[33]   B. Sun, P. Wang, B. Ma, J. Deng, J. Luo, Effects of annealing on the temperature coefficient of resistance of nickel film deposited on polyimide substrate, 160 (2019) 18–24. https://doi.org/10.1016/j.vacuum.2018.11.016.

[34]   B. C. Johnson, Electrical resistivity of copper and nickel thin-film interconnections, J. Appl. Phys. 3018 (2017) 1–8. https://doi.org/10.1063/1.345424.

[35]   J.P. Holman, Experimental Methods for Engineers, 8th ed., McGraw Hill (2012).

[36]   A.R. Gifford, D.O. Hubble, C.A. Pullins, T.E. Diller, S.T. Huxtable, Durable Heat Flux Sensor for Extreme Temperature and Heat Flux Environments, 24 (2010). https://doi.org/10.2514/1.42298.

[37]   B.F. Monea, E.I. Ionete, S.I. Spiridon, D. Ion-Ebrasu, E. Petre, Carbon nanotubes and carbon nanotube structures used for temperature measurement, Sensors (Switzerland). 19 (2019). https://doi.org/10.3390/s19112464.

[38]   A. Elkholy, R. Kempers, Experimental investigation of geyser boiling in a small diameter two-phase loop thermosyphon, Exp. Therm. Fluid Sci. 118 (2020) 110170. https://doi.org/10.1016/j.expthermflusci.2020.110170.

[39]   A. Elkholy, C. Unlusoy, R. Kempers, Thermal performance of a two-phase loop thermosyphon with an additively manufactured evaporator, Appl. Therm. Eng. 202 (2022) 117692. https://doi.org/10.1016/j.applthermaleng.2021.117692.

[40]   D. Jafari, W.W. Wits, B.J. Geurts, Phase change heat transfer characteristics of an additively manufactured wick for heat pipe applications, Appl. Therm. Eng. 168 (2020) 114890. https://doi.org/10.1016/j.applthermaleng.2019.114890.

[41] A.J. Robinson, J. Colenbrander, T. Deaville, J. Durfee, R. Kempers, A wicked heat pipe fabricated using metal additive manufacturing, Int. J. Thermofluids. 12 (2021) 100117. https://doi.org/10.1016/j.ijft.2021.100117.

[42] R. Kempers, A. Robinson, Heated Meter Bar Techniques: What You Should Know and Why, Art Meas. Therm. Sci. (2021) 313–335.

[43] T.L. Bergman, A.S. Lavine, F.P. Incropera, D.P. DeWitt, Fundamentals of heat and mass transfer, 7th ed., John Wiley and sons (2011).

# Chapter 7    Conclusions and Future Work

## 7.1. Summary and Conclusions

In Chapter 3, the electromechanical characterization of the Cu CWPC and NiCr CWPC showed a direct linear relationship between the applied mechanical strain and the fractional change of the electrical resistance of the integrated metal, which approved the applicability of CWPCs to be used as strain sensor. The sensitivity of these sensors was calculated in terms of gauge factor and found to be 1.17±0.06 and 1.13±0.07 for Cu and NiCr CWPCs, respectively. The analytical model used to theoretically calculate the gauge factor based on the resistivity and the geometry of material showed a good agreement with experimental results. This indicates the ability to predict the value of the gauge factor for such CWPC materials using the proposed analytical model. The mechanical properties of CWPC materials were characterized for both Cu CWPC and NiCr CWPC. The NiCr CWPC showed better UTS and Young's modulus compared to Cu CWPC due to the higher mechanical properties of NiCr wire compared to Cu wire. However, the used NiCr in this study was uncoated which caused some difficulties in the electrical resistance measurements due to the short circuit's occurrence between the wires and the metallic frame of the testing machine. Therefore, it is recommended to use a coated wire to develop the 3D-printed CWPC sensor.

In Chapter 4, the electromechanical properties of the CWPC using two different matrices were characterized. Rigid CWPC (PLA+Cu) and flexible CWPC (TPU+Cu) were selected to expand the application of CWPC as strain sensors to be used for either rigid applications such as sporting equipment or flexible application such as wearable sensor. The gauge factor of both composites was obtained from the slope of the direct linear relationship between the applied mechanical strain and the fractional change of the electrical resistance. The statistical analysis showed insignificant difference between the gauge factor values of PLA+Cu CWPC and TPU+Cu CWPC, indicating

the dependency of the gauge factor on the wire used regardless of the type of matrix. In this study, 2D DIC system was used to accurately measure the mechanical strain of both rigid and flexible material. The mechanical testing characterization of PLA+Cu and TPU+Cu showed a significant improvement in the Young's modulus when compared to pure polymer of PLA and TPU, respectively.

In Chapter 5, the reliability and reversibility of the CWPC as strain sensor was investigated. Firstly, the fatigue behaviour of both 3D-printed PLA and TPU based materials was characterized by measuring the residual strength of the CWPC samples after different number of cycles ($10^2$, $10^4$, $10^5$) using strain-controlled fatigue test (minimum and maximum applied strain of 5% and 50% of the sample's failure strain, respectively). The reduction of the residual strengths in case of PLA based materials was lower than that of TPU based materials because of the higher applied stress values with respect to UTS of the materials in case of TPU based materials compared to PLA based materials. The TPU based materials is considered to fail after $10^4$ cycles as the residual strength was less than 85% of their UTS when subjected to cyclic loading. The results showed the insignificance difference between the residual strength and the UTS of PLA based samples, while the TPU+Cu material showed a significant difference between the residual strength and UTS. For the Young's modulus, both materials showed a significance difference between the residual Young's modulus and the Young's modulus of the material. The DIC results approved the more damage accumulation with the number of cycles in case of TPU based materials compared to PLA based materials. The electromechanical characterization results under cyclic loading showed a reversable change of the electrical resistance with the applied strain, indicating the reverse piezoresistive behaviour of the 3D-printed CWPC and its applicability to be used as strain sensor under dynamic loading. The electromechanical test showed the failure of PLA+Cu at 30,000 cycles

and 180 cycles for TPU+Cu when the Cu wire was broken. The strain-life analytical model showed agreement with the experimental data.

In Chapter 6, the thermal sensing capability of the 3D-printed CWPC was characterized when using different wire materials of Cu and Ni with rigid and flexible materials of PLA and TPU, respectively. The temperature coefficient of resistance characterization showed a linear relationship between the change of applied temperature and the fractional change of the electrical resistance of the wire for all 3D-printed CWPC samples. The temperature coefficients of resistance values were calculated and found to be 0.0041 and 0.0053 1/K for PLA+Cu and PLA+Ni, respectively. The heat flux characterization of the samples was conducted by applying a predetermined power on the sample and compare it to the corresponding measured heat flux power by the 3D-printed CWPC sensor. The results showed an acceptable error between the applied power and the measured heat flux. A prototype of a real-life application of thermal piping system was designed using a flexible TPU+Cu and the results validated the 3D-printed CWPC to be used as a heat flux sensor for different geometries.

Generally, the proposed study developed a low-cost smart material of AM CWPCs that can be used as strain and heat flux sensors with improved mechanical properties. Although the accuracy of the proposed sensors in terms of gauge factor for strain sensors and thermal resistance for the heat flux sensors is not high when compared to the commercial sensors, the cost of the CWPC sensors is much less when compared to a commercial strain gauges and heat flux sensors. For instance, the cost of Cu CWPCs is approximately less than a dollar, while the costs of commercial strain gauges and heat flux sensors are few dollars. Self sensing using AM CWPCs material will provide enormous contribution towards the promising market of 3D printing by using low cost and open-source 3D printers. This fabrication approach can provide design flexibility to produce a

171

functionalized polymer composite structure with in-situ sensing capabilities. The different matrices used with different mechanical properties widen the range of applications of CWPCs sensors by 3D-print functionalized structure with tunable properties. Promising results in terms of gauge factor and temperature coefficient of resistance were achieved for CWPCs sensors for either strain or thermal sensing applications.

## 7.2. Recommendations and Future Work

Future studies should be conducted to fulfil the research gap in the current study. The following points describe the different areas that should be covered to fully characterize the developed 3D-printed CWPC and to improve the fabrication process:

- To enhance the performance of the FFF process in terms of introducing the wire simultaneously with the polymer filament, different designs for the modified part of the 3D-printer's head should be taken into consideration to provide more flexibility in designing the sensing element within the 3D-printed sample.

- The process of introducing the wire into the printer head should be automated with a cutting mechanism to leverage the potential of FFF technique for industrial applications.

- To fully understand the behaviour of the CWPC under mechanical loading, the interfacial interaction between the wire and matrix should be investigated by conducting a pull-out test. To minimize any debonding that may occur between the wire and the matrix, a pre-treatment step for the wire may be needed for better bonding with the polymer. This would help in minimizing the source of error when correlating the electrical resistance of the integrated wire to the strain of the composite structure (the electromechanical characterization of the CWPC sensor).

- Characterize the strain sensing capability of the 3D-printed CWPC sample with different wire orientations is crucial. The change in wire orientation can be used for joint angle measurements (goniometer) such as human wrist which is important for some sporting purposes. Sensors with different orientations can measure the angle of the wrist movement due to the stretching or contraction that occurs during movement.

- Another parameter to optimize the performance of CWPCs strain sensor is the volume fraction of the wire relative to the total volume of the structure which can be controlled by varying wire diameters to study its effect on mechanical behaviour and sensing capability of CWPCs.

- In terms of dynamic loading, different fatigue testing parameters such as the loading amplitude, loading frequency, and loading ratio should be examined to optimize the performance of the 3D-printed CWPC under cyclic loading. However, the applied testing frequency is small (5 Hz), it is crucial to investigate the temperature increase under cyclic loading, especially in case of TPU-based materials.

- Explore and design different real-life applications of the functionalized CWPC sensors. These applications may include soft actuators and wearable sensors by using the flexible CWPC material. Bioinspired structures can be also investigated.

- For the heat flux characterization test, a thermal camera can be used during the test to measure the change of temperature across the 3D-printed samples to have a better understanding about the source of error in the heat flux measurements and to quantify any heat loss during the test.

- Further characterization of the heat flux sensor in terms of response time (how quickly the sensor responds to the change of temperature) should be investigated. The response time is a vital parameter for different thermal applications, as some of them may require fast response time, while others may need consistency in the response time rather than a quick response time.